THESIS

# DIFFERENTIAL SPUTTERING YIELDS OF REFRACTORY METALS BY ION BOMBARDMENT AT NORMAL AND OBLIQUE INCIDENCES

Submitted by

Kirk A. Zoerb

Department of Mechanical Engineering

In partial fulfillment of the requirements

For the Degree of Master of Science

Colorado State University

Fort Collins, Colorado

Fall 2007

COLORADO STATE UNIVERSITY

October 30, 2007

WE HEREBY RECOMMEND THAT THE THESIS PREPARED UNDER OUR SUPERVISION BY KIRK A. ZOERB ENTITLED "DIFFERENTIAL SPUTTERING YIELDS OF REFRACTORY METALS BY ION BOMBARDMENT AT NORMAL AND OBLIQUE INCIDENCES" BE ACCEPTED AS FULFILLING IN PART REQUIREMENTS FOR THE DEGREE OF MASTER OF SCIENCE.

Committee on Graduate Work

**Committee Member:**

**Committee Member:** **Raymond S. Robinson**

**Committee Member:** **Azer P. Yalin**

**Advisor:** **John D. Williams**

**Department Head:** **Allan T. Kirkpatrick**

ABSTRACT OF THESIS

DIFFERENTIAL SPUTTERING YIELDS OF REFRACTORY METALS BY ION BOMBARDMENT AT NORMAL AND OBLIQUE INCIDENCES

Currently, the problems of sputter erosion and spacecraft contamination due to deposition of sputtered material are generally handled by numerical computer codes. These codes rely on sputtering data as "inputs" which are needed to compute the magnitude and trajectory of the sputtered particles. The basic sputtering data available for these codes tend to be incomplete. Often only total sputter yields, with units of sputtered atoms per ion, have been measured. The total sputter yields characterize the total amount of material sputtered, but without directional trajectory information of the sputtered particles. Thus, without such directional information, computer codes make assumptions on the angular sputtering profile, which are often not in agreement with the actual profiles. The angular description of the sputtering is treated by differential sputter yields ($y(\alpha)$), with units of sputtered atoms per ion per steradian, which quantifies sputtering as a function of angular direction ($\alpha$ is the polar angle relative to the surface normal).

Differential sputter yields are reported for Molybdenum, Tantalum, and Tungsten after exposure to Xenon, Krypton, and Argon ion bombardment at multiple angles of incidence (0 - 60°) and ion energies (150 - 1500 eV). Differential yields were measured by sweeping a Quartz Crystal Microbalance in a semi-circular arc over a target in the plane defined by the target normal and ion beam axis. Differential yields were integrated to obtain total sputter yields. The dependence of total yield on angle of incidence was also investigated. The total yields were found to be largest for angles of incidence between 45° and 60°. The effects of the bombarding ion energy and the ion mass-to-target atom mass ratio on the differential yield distributions are discussed. In addition, measurements of differential sputter yields as a function of both polar and azimuthal angles are presented.

Kirk Andrew Zoerb
Mechanical Engineering Department
Colorado State University
Fort Collins, Colorado 80523
Fall 2007

# ACKNOWLEDGEMENTS & DEDICATION

The completion of this thesis was the direct result of assistance provided to the author by many people. Firstly, I'd like to thank Dr. John Williams for advising me on this thesis, the lab experiments, and life in general and also for giving me the opportunity to run amok at the CSU Ion Stand. I'd also like to thank Dr. Paul Wilbur for giving me the initial push into graduate school, and for being such an inspiring professor. Thank you, also, to Dr. Azer Yalin and Dr. Steve Robinson for agreeing to be on my thesis committee. Thank you, Azer, for the guidance you provided in the experiments, research, and writing during my time at CSU.

I'd like to thank my wife, Catherine, for giving constant inspiration and (sometimes dogged) support during my time in graduate school. Thanks are owed to my parents, Ron and Linda, for nurturing and encouraging my love of science and for their support in general.

I'd also like to thank Russ Martin, Vijay Surla, Casey and Cody Farnell, Rafael Martinez, and Daisy Williams for keeping me laughing at the lab, and to Mark Buttweiler and Dustin Warner for their assistance with the lab equipment. I'd like to thank Jonathon Wolf and Rosa Muñoz for performing many of the QCM measurements. The funding provided by the Jet Propulsion Laboratory and the Air Force Research Labs, Edwards Air Force Base is also greatly appreciated.

Lastly, I'd like to dedicate this thesis to my father, Ronald L. Zoerb: 1949-2003. "Wish you were here."

-Kirk Zoerb, August 2007.

CONTENTS:

Chapter 1 Introduction........................................1

1.1 Overview of Thesis........................................1

1.2 Introduction to Electric Propulsion........................................1

1.2.1 Electric Propulsion........................................2

1.2.1.1 Electron Bombardment Thruster........................................3

1.2.1.2 Hall Effect Thruster........................................5

1.2.2 Importance of Electric Propulsion........................................7

1.2.3 Brief History of Electric Propulsion........................................10

1.3 Introduction to Sputtering........................................13

1.3.1 Brief History of Sputtering........................................13

1.3.2 Sputtering in Electric Propulsion Systems........................................16

1.3.2.1 Accelerator and Screen Grid Sputtering Considerations........................................16

1.3.2.2 Hollow Cathode Sputtering Consideration........................................19

1.4 Summary........................................19

Chapter 2 Sputtering and Sputtering Models........................................20

2.1 Sputtering Process........................................20

2.2 Sputtering Models........................................24

2.2.1 Sigmund Total Yield Formula........................................26

2.2.2 Yamamura & Tawara Semi-Empirical Total Yield Formula........................................27

2.2.3 Oblique Ion Incident Total Yield Models........................................29

2.2.4 Differential Sputter Yields and Models........................................31

2.3 Summary........................................34

Chapter 3 Methods for Measuring Sputter Yields........................................35

3.1 Total Sputtering Yields........................................35

3.1.1 Weight Loss........................................35

3.1.2 Depth Profiling ........................................ 36

3.1.3 Gas Phase Spectroscopy ........................................ 40

3.1.4 Accumulation ........................................ 43

3.2 Quartz Crystal Microbalance ........................................ 43

3.3 Differential Sputtering Yields ........................................ 47

3.4 Summary ........................................ 50

Chapter 4 Experimental Set-up and Measurements ........................................ 51

4.1 Vacuum Chamber ........................................ 51

4.2 Ion Source and Target ........................................ 52

4.3 Quartz Crystal Microbalance Sensor ........................................ 56

4.4 Measurement Procedure ........................................ 57

4.5 Data Acquisition and Analysis ........................................ 59

4.6 Infinitesimal Beam Spot Assumption Analysis ........................................ 61

4.7 Azimuthal Measurement Description ........................................ 65

4.8 Summary ........................................ 67

Chapter 5 Results & Discussion ........................................ 68

5.1 Normal Incidence ........................................ 68

5.2 Non-normal Incidence ........................................ 71

5.3 Azimuthal Measurements ........................................ 79

5.4 Summary ........................................ 83

Chapter 6 Conclusion and Suggestions for Future Work ........................................ 84

Bibliography ........................................ 86

Appendix A: Table of Polynomial Curve Fit Coefficients to Experimental Data ........................................ 91

Appendix B: Table of Modified Zhang Fit Parameters to Experimental Data ........................................ 97

Appendix C: Table of Data Collected in Azimuthal Experiments ........................................ 100

# Chapter 1 Introduction

## 1.1 *Overview of Thesis*

The pages in this document will provide a discussion on sputtering experiments performed using a Quartz Crystal Microbalance to obtain differential sputtering yields. Xenon, Argon, and Krypton ions were used to bombard targets of Molybdenum, Tungsten, and Tantalum at energies of 500, 750, 1000 and 1500 eV at 0, 15, 30, 45, and 60° angles of incidence. Chapter 1 provides a brief introduction to the idea of electric propulsion and sputtering. The theory of sputtering and some numerical models of sputtering will be discussed in Chapter 2. Various methods of measuring sputter yields are presented in Chapter 3. Chapter 4 will focus on the experimental set-up and methods used in this thesis investigation. Chapter 5 will present the results and discuss the experiments performed. Chapter 6 will discuss conclusions and future work. Appendices of figures and tables summarizing the experiments performed are provided (Appendices A, B, and C).

## 1.2 *Introduction to Electric Propulsion*

This section provides a basic description of the idea of electric propulsion (EP). The main sub-categories of EP thrusters are discussed, with more detailed explanations given to specific types of EP thrusters that are affected by sputtering. The importance and limitations of electric propulsion will be discussed via a comparison to the conventional chemical thruster. A brief history of electric propulsion is also given.

### 1.2.1 Electric Propulsion

Electric propulsion devices use electric power to accelerate a propellant, thereby producing a thrust. Major components of the EP system on a spacecraft include electricity generation/storage, a propellant storage and feed system, electrical power processing/conditioning equipment, and the actual thrusting device. There are three main sub-categories of EP devices[1]: electrothermal, electrostatic, and electromagnetic. Electrothermal EP devices use electrical power to heat a propellant and use nozzles to accelerate the propellant to produce thrust (e.g. resistojets and arcjets; Figure 1.1). Electrostatic EP devices use electrical power to accelerate charged particles through an applied electric field (e.g. electron bombardment, contact ion, and emission/colloid type thrusters; Figure 1.2). Electromagnetic EP devices apply an electric field in a plasma and use a magnetic field to generate a force (the $j \times B_{mag}$ force) on the plasma, accelerating it away from the device (e.g. Hall effect, magnetoplasmadynamic, and pulsed-plasma type thrusters; Figure 1.3). It is noted that Hall effect thrusters can also be categorized as electrostatic-based devices. Sputtering effects are most important in electrostatic and electromagnetic types of devices.

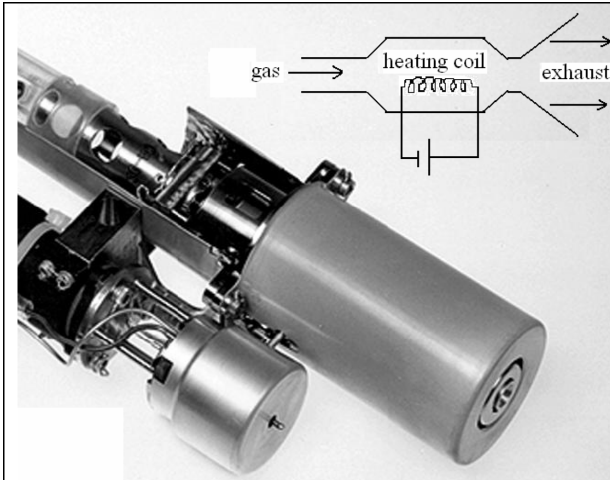


**Figure 1.1: Resistojet type electrothermal thruster[1]**

**Figure 1.2: Electron Bombardment type electrostatic thruster[1]**

**Figure 1.3: Hall Effect type electromagnetic thruster [Busek, BHT-1500, www.busek.com]**

#### 1.2.1.1 Electron Bombardment Thruster

The current preferred type of electrostatic thruster is the electron bombardment type, also referred to as a Kaufman thruster (Figure 1.4). This type of thruster was used in NASA's Deep Space 1 technology demonstration mission and on JAXA's Hayabusa mission to land a craft on the surface of the asteroid Itokawa and return a sample. It will be used in NASA's DAWN mission to rendezvous with asteroids Vesta and Ceres. These thrusters are also used on numerous satellites in Earth's orbit[2]. In this type of thruster, a plasma (at potential $V_{anode}$) is created in a discharge chamber by bombarding a neutral propellant gas (usually Xe) with energetic electrons. The energetic electrons can be supplied with a hollow cathode at

potential $V_{cathode}$. JAXA used microwave radiation to excite the electrons and create a discharge plasma in the Hayabusa thrusters. As the electrons flow from the hollow cathode to the anode held at potential $V_{anode}$ (on the order of 30Vabove $V_{cathode}$), they have collisions with neutral Xe atoms. Some of these collisions result in removing an electron from the Xe atom creating a $Xe^{+}$ ion. This plasma is magnetically confined to a cup-like shape inside the discharge chamber (defined by the "B-field" lines in Figure 1.4) with the open end of the "cup" adjacent to the ion optics (grid set) assembly.

The ion optics system usually consists of 2-3 grids that have differing voltages applied to them in order to extract and focus the propulsive ion beam. The grid directly adjacent to the discharge plasma is referred to as the screen grid and is kept at a high positive potential, $V_s$ (usually equal to $V_{cathode}$). This voltage roughly determines the energy that each ion will have at the end of the acceleration process. The grid directly downstream of the screen grid is the accelerator grid and is kept at a negative potential, $V_a$, in order to accelerate the ions out of the discharge chamber. The accelerator grid's negative bias also keeps electrons produced by the neutralizer cathode from entering the discharge chamber (or in other words, the negative bias on the accelerator grid prevents electron backstreaming). Downstream of the accelerator grid may be other grids (typically referred to as decelerator grids) that help in focusing the beam and are typically held at potentials between $V_a$ (negative) and 0V. To maintain the spacecraft's electrical neutrality and to keep beam divergence to a minimum, a second hollow cathode emits a current of electrons into the beam through a plasma bridge that forms between this cathode and the beam plasma. The number of electrons emitted is equal to the number of ions in the beam, thus current neutralizing the spacecraft.

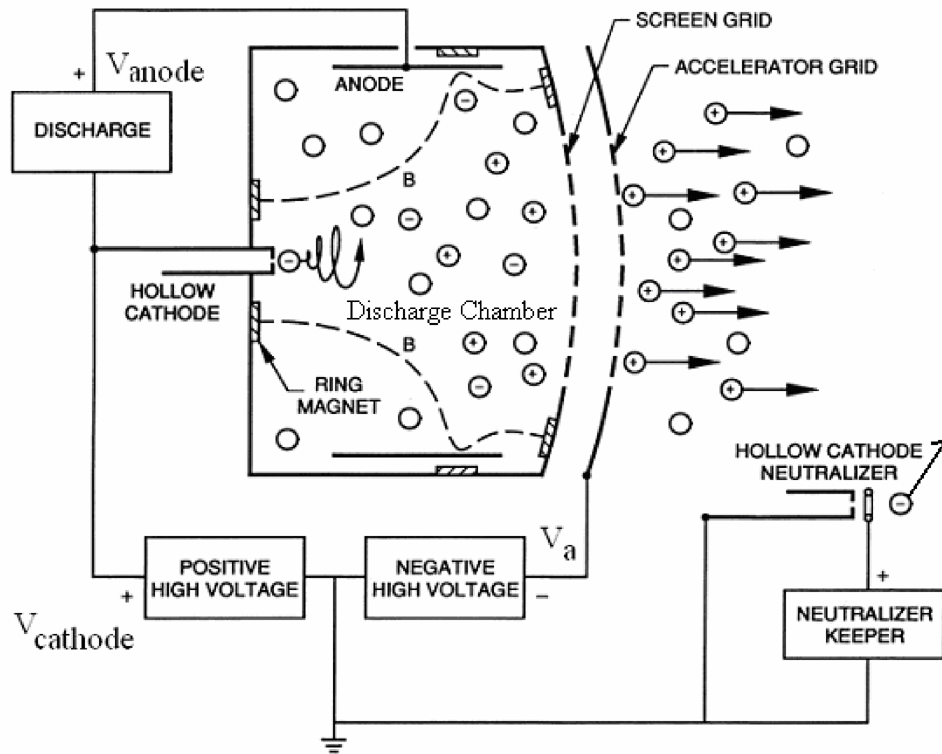


**Figure 1.4: Electron bombardment type (Kaufman type) thruster[1].**

#### 1.2.1.2 Hall Effect Thruster

The currently most preferred type of electromagnetic thruster is the Hall effect thruster (Figure 1.5). This type of thruster was used on ESA's highly successful SMART-1 mission and is used on at least 10 active Earth orbiting satellites[2]. A typical Hall effect thruster consists of an inner annular magnetic coil and an outer annular magnetic coil that creates a radial magnetic field (B-field). The region spanning the two magnetic coils is the discharge channel, with one end closed and the other end open. The discharge channel walls are usually made from Boron Nitride, an insulating material, in order to electrically isolate the discharge channel. Like the electron bombardment type thruster, electrons are created in a hollow cathode device that (unlike the electron bombardment type thruster) is located outside and downstream of the discharge chamber. Electrons created here are pulled toward the anode (held at potential $V_{anode}$, ~300V) located at the closed end of the discharge chamber.

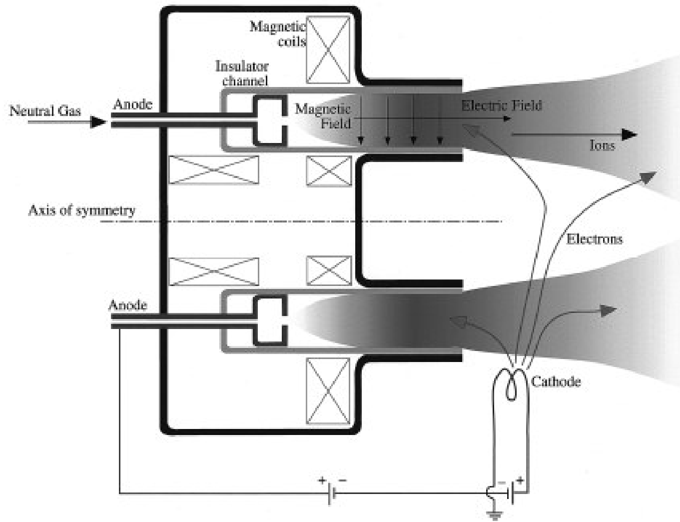


**Figure 1.5: Hall effect type thruster[1].**

As the moving electron (with velocity *v*, charge *q*) enters the magnetic field (*B*) created by the magnetic coils, the electron experiences a Lorentz force, *F*:

$$\vec{F} = q\left(\vec{E} + \vec{v} \times \vec{B}\right) \tag{1.1}$$

This force acts in a circumferential (azimuthal) direction, because the electric field between the cathode and the anode has an axial direction and the magnetic field is in a radial direction (the Lorentz force acts perpendicularly to these fields) as shown in Figure 1.6. The electron is then "trapped" circling (the so called Hall current) the inner magnetic coil region for a majority of its lifetime, thus creating an area of high electron density called the virtual cathode region (the potential here is approximately that of the hollow cathode). Eventually, the circling electron will leave the influence of the magnetic field and finally make its way to the anode as it has collisions with walls, neutrals, ions, and other electrons.

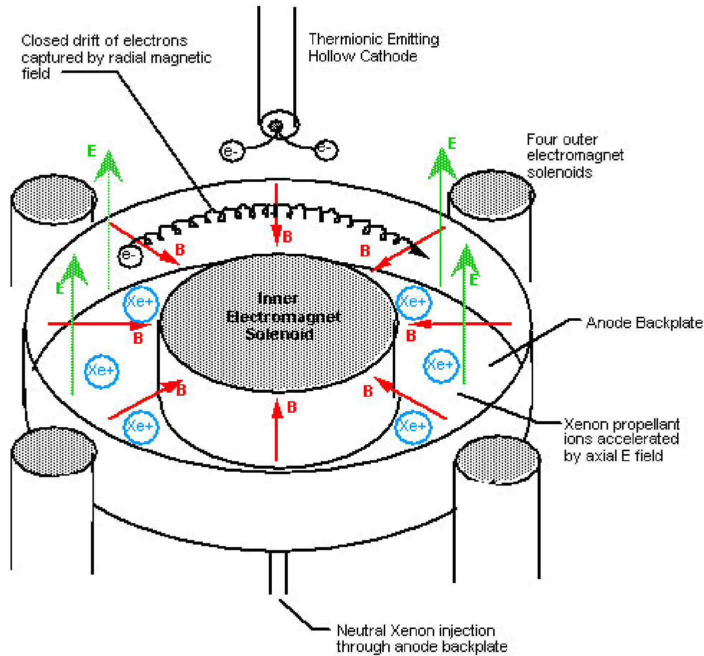


**Figure 1.6: Electron path in Hall effect thruster[6].**

To create a plasma, a neutral gas (typically Xe) is flowed into the discharge chamber through the anode. As the neutral atoms diffuse through the discharge chamber, collisions with electrons create $Xe^+$ ions. Once the ion is created, it is accelerated axially toward the virtual cathode region of circling electrons. Due to the ion's much larger mass than the electron, the Lorentz force impaired upon it in the magnetic field will not greatly affect the ion's azimuthal motion (as in the case of the electron) and will leave the thruster with an energy on the order of 150 to 300 eV, thus providing the desired thrust. The hollow cathode will now also provide an electron to neutralize the space charge created by the expelled ion.

## 1.2.2 Importance of Electric Propulsion

With NASA, ESA, JAXA, and commercial space industry partners considering ambitious space missions, it is important to ensure that the technologies used on the spacecraft will provide the best match to the mission and its goals. Many factors contribute to the quality of a mission including cost and mission time. One of the largest costs in a mission is the act of freeing the payload from Earth's gravitational well. With costs of approximately $22,000 per kilogram to insert a craft into geostationary orbit and

approximately $10,000 per kilogram for low earth orbit (LEO)[3], it is important to minimize the launch weight of the spacecraft to keep mission costs low.

The basic governing equation in space propulsion is one that is fittingly known as "the rocket equation":

$$\frac{m_o}{m_1} = \exp\left[\frac{v_1 - v_0}{v_{ex}}\right] = \exp\left[\frac{\Delta v}{v_{ex}}\right] \qquad \textbf{(1.2)}$$

where $m_0/m_1$ is the initial mass to final mass ratio, $v_0$ is the initial velocity of a craft, $v_1$ is the final velocity of a craft, and where $v_{ex}$ is the exhaust velocity of the propellant. The rocket equation quantifies the mass of propellant (i.e., $m_1$-$m_0$) that must be expelled through a propulsive device to get a certain change in characteristic velocity or "delta v" (written as $\Delta v$), one of the most important variables in any space mission or maneuver.

Another important concept in space propulsion is the specific impulse, $I_{sp}$, which is the measure of the amount of impulse (change in momentum) per unit of expelled propellant mass and is defined as:

$$I_{sp} = \frac{v_{ex}}{g} = \frac{T}{\dot{m}g} \qquad \textbf{(1.3)}$$

where g is acceleration due to gravity, $T$ is thrust, and $\dot{m}$ is mass flow rate; giving $I_{sp}$ units of time (seconds in SI). Specific impulse is important because it determines the amount of fuel that must be processed to change a spacecraft's velocity by a given amount, i.e. a measure of the propellant efficiency. If the rocket equation is written in terms of $I_{sp}$ the following equation is obtained:

$$\frac{m_o}{m_1} = \exp\left[\frac{\Delta v}{I_{sp} g}\right] \qquad \textbf{(1.4)}$$

It can be seen from equation (1.4) that it is desirable to have a high specific impulse in order to keep the initial spacecraft mass and the propellant mass low.

In a typical chemical rocket thruster, all of the energy used to accelerate the spacecraft is stored in the chemical bonds present in the on-board propellant (oxidizer and fuel). The best chemical rockets can provide an exhaust velocity of less than 5,000 m/s (yielding a specific impulse <~ 500 s) and is limited by

the energy released in the available chemical reactions and by the nozzle's ability to convert that energy into thrust. Electrothermal EP devices use electrical power to heat a propellant and use nozzles to accelerate the fluid to produce thrust, similar to the chemical rocket, thus giving the electrothermal device similar $I_{sp}$ limitations to that of a chemical thruster.

Due to the electrostatic and electromagnetic devices' ability to impart energy to propellant ions through electrical means, they can produce the desired high exhaust velocities and, thus, can give the devices a high $I_{sp}$ (>1500 s). Unlike chemical propulsion, these EP devices do not need to transport all the energy (stored in the chemical bonds in chemical propulsion) used to accelerate the craft. Instead, solar panels can be used to convert energy from the sun to the requisite electrical power. If solar power is not adequate, the electric power can be supplied by an on-board energy system (such as a fission reactor), and while the craft is again carrying all of the energy used to accelerate the craft, it can have lower mass than if it were storing the energy in chemical bonds.

**Table 1: Specific Impulses of Thrusters[4]**

| Thruster Type | Typical $I_{sp}$, (s) |
|---|---|
| Chemical rocket | 500 |
| Electrothermal (arcjet, resistojet) | 500 |
| Electromagnetic (Hall, MPD) | 1600 |
| Electrostatic (electron bombardment) | 3000 |

Although the specific impulses are high, the total thrust from EP devices are low (typically in the $10^{-3}$ Newton range) due limitations of the power generation/distribution. This limitation can be seen by considering the definition of thrust ($T$) and power ($P$) while neglecting efficiency losses:

$$T = \frac{dm}{dt} v_{ex} \tag{1.5}$$

$$P = \frac{1}{2}\frac{dm}{dt} {v_{ex}}^2 \tag{1.6}$$

Combining terms reveals that:

$$T = \frac{2P}{v_{ex}} = \frac{2P}{I_{sp} g} \tag{1.7}$$

hence, the higher the $I_{sp}$, the lower the thrust for a given power level. Therefore, these devices are only useful in an environment where drag forces are less than the mN thrust level (i.e., in space). To get the EP device into the low-drag space environment, launches using traditional chemical rockets are still needed. Once in the space environment, the low thrust feature can have advantages. For example, using a low thrust EP device on a satellite provides more precise control of the satellite's position (station-keeping) than with a conventional hypergolic-fuel based thruster, allowing more satellites to occupy an orbital slot.

To illustrate the effect that specific impulse can have on a mission, consider a spacecraft in LEO that will deliver a scientific payload to Mars. A typical characteristic $\Delta v$ from LEO to a Mars orbit is approximately 6000 m/s. If a chemical rocket ($I_{sp}$= 500 s) were used to accomplish the mission, only 30% of the initial mass of the craft in LEO could be delivered to Mars, the rest being expelled as propellant. If an electron bombardment type EP thruster were used ($I_{sp}$= 3000 s), 80% of the initial mass of the craft in LEO could be delivered to Mars. (Note that it is assumed that the EP power system will be useful at the destination). Using EP, then, allows a greater payload to be delivered or an equal payload with drastically less mass to launch from Earth and thus reducing the cost of a mission.

However, EP will have a great advantage over conventional chemical propulsion only in certain missions. In order for an EP device to be a better match to a mission than traditional chemical propulsion, the mission must either be one that has a great travel distance and delta v associated with it, or one of low delta v in which transit time is not of great concern (due to the low but continuous thrust of the EP device). Even in missions where the application of EP will have an advantage over chemical thrusters, EP thrusters are not always selected due to their greater complexity and the relative inexperience of using EP systems in spaceflight. Another concern is that the EP system must run continuously and reliably for months to years on end where in chemical propulsion a thruster burn time would only be required to last minutes.

### 1.2.3 Brief History of Electric Propulsion

Choueiri[5] divided a US-centric history of electric propulsion into five eras spanning one century (the author has combined Choueiri's last two eras into one):

1. Era of Visionaries: 1906-1945

2. Era of Pioneers: 1946-1956
3. Era of Diversification and Development: 1957-1979
4. Era of Acceptance and Application: 1980- Present (2007)

The beginning of the history of EP has been widely credited to Robert Goddard when, in 1906, he wrote several entries in his notebook, starting with: "At enormous potentials can electrons be liberated at the speed of light…"[5]. Goddard had several EP related entries in his notebooks from 1906-1912, in which he recognizes the advantages of using ions instead of electrons and also recognizes the need to neutralize the accelerated particles so that a craft will remain electrically neutral. Goddard filed patents in 1913 and 1917 related to ionizing gas and electrostatically accelerating ions.

In 1911, Konstantin Tsiolkovsky (who also developed the rocket equation) published the following statement: "It is possible that in time we may use electricity to produce a large velocity for the particles ejected from a rocket device"[5]. This was the first statement explicitly mentioning the use of electricity to provide a thrust for a rocket device. Both Goddard and Tsiolkovsky were inspired to think of electrically propelled rockets by recent "cathode ray" experiments by J. J. Thompson. While both men were among the first to conceptualize EP, they were also the first to feel that chemical rockets deserved higher research priority.

In 1929, Hermann Oberth published a chapter entitled "The Electric Spaceship" in his book *Ways to Spaceflight* that dealt with spacecraft power and various EP ideas. Because Oberth's book was widely read by space enthusiasts, the idea of EP began to permeate science fiction literature and the minds of space-faring dreamers. Unfortunately, the idea was slow to take hold in scientific and engineering minds. The next mention of EP in scientific literature did not occur again until 1945.

The Era of Pioneers is marked by a few scientists who investigated EP largely on their own. Of most note in this period was Ernst Stuhlinger who, in 1947, was encouraged by Werhner Von Braun to look into Oberth's ideas on EP. In 1954, Stuhlinger published and presented "Possibilities of Electrical Space Ship Propulsion" at the *5$^{th}$ International Astronautical Congress*. This paper was the first to include detailed design considerations of an EP system. Stuhlinger published two other design focused papers in 1955 and 1956. During the same period (in 1949), L.R. Shepherd and A.V. Cleaver published a paper that

outlined some EP concepts and concluded that, while EP was an interesting concept, it was impractical due to the system's large power requirements. In 1952, however, Lyman Spitzer published a similar paper to Shepard and Cleaver's and, instead, came to the conclusion that EP was feasible.

The Era of Diversification and Development is characterized by teams of scientists and engineers working together to work out the design and manufacture of physical EP devices. In 1957, the Air Force issued the first research grants into EP[6]. Soon, major aerospace corporations (Lockheed, General Electric, Hughes, Thiokol, and Aerojet) had EP research divisions. The newly formed NASA had several centers that worked on EP (Jet Propulsion Laboratory, Marshall Space Flight Center, and the Lewis Research Center). Work was also accomplished at numerous academic institutions during this time. In 1964, the Solar Electric Rocket Test I (SERT I) was launched on a ballistic rocket and demonstrated that EP devices would work in space. In 1970, NASA launched the SERT II mission that demonstrated the long term usage of an EP device in space. Tests on the SERT II spacecraft were done as late as 1991 (though the last thruster start was in 1981).

The Era of Acceptance and Application is marked by commercial companies and NASA working toward the use of EP in non-experimental missions and satellites, due to the successes demonstrated by the SERT missions. In the early 1990's, Lockheed Martin used an electrothermal EP thruster for station-keeping on a satellite. In 1997 Hughes Space and Communications Company launched a satellite with its XIPS (Xenon Ion Propulsion System) thruster, the first electrostatic EP thruster used for the station-keeping of a commercial satellite (there are about 25 in operation today[2]).

An important EP milestone for NASA came during 1998 and 1999 when it successfully used the NSTAR (NASA Solar Electric Propulsion Technology Application Readiness) electrostatic thruster to complete a mission to rendezvous with asteroid Braille and comet Borrelly. In 2003-2004, ESA successfully used a Hall effect thruster to place the SMART-1 probe in orbit around the Moon. In an even more daring mission, JAXA successfully used an electrostatic EP thruster on the Hayabusa mission to rendezvous with asteroid Itokawa in late 2005, where the craft landed on the asteroid's surface to collect and return a sample; however, it's not yet clear if the sample collection operation was successful.

The ambitious NASA project Prometheus was to make extensive use of EP to explore the solar system, but in 2004-2005 most of the budgets had been cut to accommodate the NASA back-to-the-moon-and-onto-Mars strategy, which does not have EP as a central technology. Also cut in early 2006 was the EP-equipped, nearly ready-to-launch DAWN mission to asteroids Ceres and Vesta. However, after an international uproar of complaints from scientists, NASA re-instated the mission and it was launched in September 2007 to start a 2,500 day mission.

## 1.3 Introduction to Sputtering

### 1.3.1 Brief History of Sputtering

Sputtering is defined as the removal of near surface atoms by energetic particle bombardment. The term 'sputtering' was possibly derived from J. J. Thompson's use of the word 'spluttering' to describe the wear of a cathode in a vacuum tube. The first actual uses of the term 'sputtering' did not occur until the early 1920's when I. Langmuir and K.H. Kingdon of General Electric Research Labs used the term in their publications[7].

The first person to formerly study sputtering was W.R. Grove (the inventor of the fuel cell) whose work, "On the Electro-Chemical Polarity in Gases" published in 1852 described the use of a wire as a sputtering source material to be deposited onto the surface (Figure 1.7) of a highly polished silver plate[8]. In 1858, A.W. Wright published a paper[9] on the use of an "electrical deposition apparatus" that he used to create mirrors; a process that put him at odds with Thomas Edison when Edison filed a patent (1884) for a similar arc deposition device[7]. In 1902, Edison also received a patent for a sputter deposition process that put a layer of gold on his wax phonograph cylinders[10].

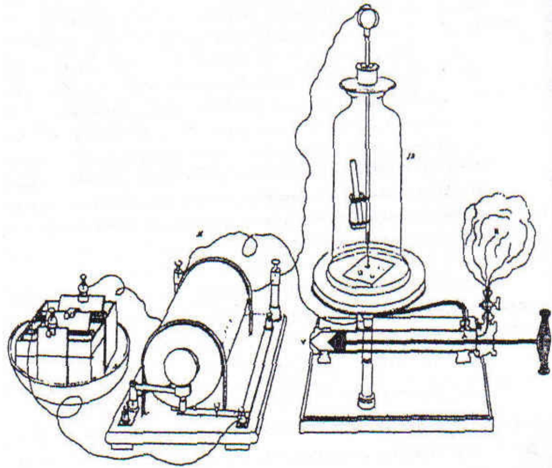

**Figure 1.7: Diagram of First Sputtering Device used by Grove in 1852[8]**

Most early sputtering experiments were performed with gas glow discharges and were typically performed at pressures of approximately 1 Torr (1 mm of Hg). In 1909, Stark worked on a momentum theory of sputtering, which was later (1935) cast aside in favor of a now defunct thermal evaporative process theory[11,12]. The most extensive early sputter measurements were made in the 1920's and 1930's by Guentherschulze[13]. In the 1920's Kingdon and Langmuir worked on sputtering theory, who (like Stark) proposed a momentum transfer theory of sputtering[14]. In 1926, A. von Hipple proposed a thermal evaporative sputter theory[14], where it was thought that when a high energy ion interacted with the target, a localized area of extremely high temperature would result in the vaporization of the target material (creating the source of sputtered particles).

The thermal process theory posited that there would be no preferred sputter direction (i.e. it would have a cosine distribution), while the momentum theory predicted that such a preference would exist[14]. Seeliger and Sommermeyer performed the first sputter experiment (1935) designed to obtain angularly resolved sputtering measurements to test which of the two theories were correct[14]. The results indicated that the distribution was cosine-like with no preferred direction, thus giving the evaporative theory a preferred status. In 1956, Gottfried Wehner conducted sputtering experiments on single crystal targets and observed the coating patterns produced by the sputtered particles[15]. His results clearly indicated that there were preferred sputtering directions (Figure 1.8), thus bringing the momentum theory back as the preferred theory.

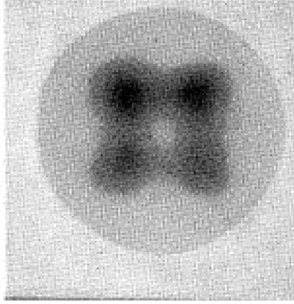

**Figure 1.8: Coating pattern produced in Wehner's single crystal sputter experiment[15].** *This case is for 100 eV* $Hg^+$ *on a Ag plate. Several preferred sputter directions are clearly seen.*

In the 1950's and 1960's, Wehner conducted extensive sputtering experiments and contributed much to the momentum transfer theory. In the late 1960's, Thompson, Lindhard, and Sigmund separately refined the momentum transfer theories further. Variants of Sigmund's model presented in the book chapter "Theory of Sputtering I"[12] are considered the standard sputtering model that is accepted to this today. In the 1980's and 1990's, Yamamura, Matsunami, Eckstein, and Bodhansky worked on formulating extensive empirical formulae (based on theoretical considerations) for use in any ion/target combination. Also of note, many Monte Carlo computer simulations have been produced in the past 40 years to emulate the sputtering process, most notably SRIM/TRIM, first developed in the early 1980's by Ziegler and Biersack.

Currently, sputtering processes are involved in many important fields including manufacturing, high energy physics, and space science/applications. A major application is that of the creation of surface property changing, thin-film coatings where sputtered particles are used to coat other materials. Thin-film coatings are used heavily in the semi-conductor, optical glass, architectural glass, and tooling (drill/mill bit) industries. Many consumer products today are coated with sputtered atoms (e.g. decorative jewelry coatings, eyewear lenses). Sputtering is also used to clean and modify micro-surfaces, hence being an important process in the fabrication of MEMS and NEMS devices. In microscopy/spectroscopy applications, a specimen's surface can be sputtered and the resulting sputtered particles masses can be identified (Secondary Ion Mass Spectroscopy, SIMS). In fusion research, the walls of reactors are constantly sputtered by very high energy neutral atoms and neutrons. High energy solar particle-induced

sputtering has also been identified as an important process on astronomical bodies that lack significant atmospheres (e.g. the moon)[16,17]. The focus of this thesis will be sputtering in electric propulsion systems.

## 1.3.2 Sputtering in Electric Propulsion Systems

Sputter erosion of surfaces is of great importance for EP thrusters and spacecraft employing such thrusters. Sputtering has been identified as a major concern in 44% (8/18) of the possible failure modes of an electrostatic thruster[18], and is also a major process that leads to failure of the insulating Boron Nitride wall material in the main discharge channel of the Hall effect thruster. Additionally, deposition of sputtered products onto other spacecraft surfaces can result in modification of surface material properties, or contamination of non-EP devices on a spacecraft.

Sputtering can affect the performance of an ion engine in different ways and can be put into two general groups: 1) modes attributed to ion impingement sputter erosion and 2) modes attributed to the re-deposition of the sputtered materials. The first group can cause failures of structural components of the thruster and can also change the geometry of the grids such that the paths that electrons and ions travel will be sufficiently disrupted (from the intentions of the designer) to cause decreases in performance. The second group can cause the build-up of films on surfaces around the sputtering source, which may eventually flake off. These flakes can cause electrical shorts or disrupt the electrostatic potentials that the charged particles follow causing decreases in performance. A thin film being deposited onto a functional surface on a spacecraft can also lead to decreases in spacecraft performance (e.g., a coating on a solar panel decreases available power, a coating on a camera lens blurs images, etc.). Sputtering affects three major components of an electrostatic EP device: the accelerator and screen grids, and the hollow cathodes.

### 1.3.2.1 Accelerator and Screen Grid Sputtering Considerations

Ion impingement sputter erosion of the accelerator grid is the major sputtering related concern in electrostatic EP devices. One process of minor concern is that of *direct* ion impingement[19], which is caused when an improperly focused ion beamlet (with energies of approximately $V_s$+$V_a$) is incidence upon the upstream and barrel surfaces of the accelerator grid. Usually these improperly focused beamlets are

sufficiently avoided with properly designed ion optics geometry and electrical operating parameters. A more unavoidable process in the sputtering of the accelerator grid is that of charge exchange. Charge exchange involves two particles: a fast moving charged ion and a slow moving (at thermal velocity) neutral atom. There is a certain statistical probability (the charge exchange cross section) that when these two particles come close enough together, the slow neutral atom will give up an electron (now an ion) to fill the fast moving ion's outer electron shell (now a fast moving neutral atom). The result of such an interaction is a fast moving neutral atom and a slow moving ion. This creates two problems 1) the slow moving ion may be in a region where its energy is insufficient to escape a negatively biased surface (i.e. the accelerator grid) and 2) the fast moving neutral can no longer be controlled by the established electric fields.

The charge exchange process is important in the gap between the screen and accelerator grids and in the regions immediately downstream of the accelerator grids. More than 90% of the charge exchange interactions occur downstream of the accelerator grid[20]. In this region, the fast moving neutral is not a concern as it will continue on its path away from the thruster. The slow moving ion, however, can now be attracted to the accelerator grid and strike it on the downstream face with an energy equal to the potential it falls through (as high as $|V_a|$), causing sputtering damage. Accumulated sputtering damage results in the formation of "pit and groove" features (Figure 1.9, Figure 1.10) in two grid systems. Over time, the pits can erode through the grid entirely, making it prone to structural failure. The few charge exchange interactions that occur in the grid gap create slow moving ions that can strike the barrel region of the accelerator grid holes, thus enlarging their diameter. This enlargement will reduce the accelerator grids' ability to repel back-streaming electrons present in the beam plasma located just downstream of the accelerator grid. The fast moving neutral created in the gap region may also cause sputter damage to the upstream and barrel surfaces of the accelerator grid depending on the trajectory it follows after the charge exchange interaction.

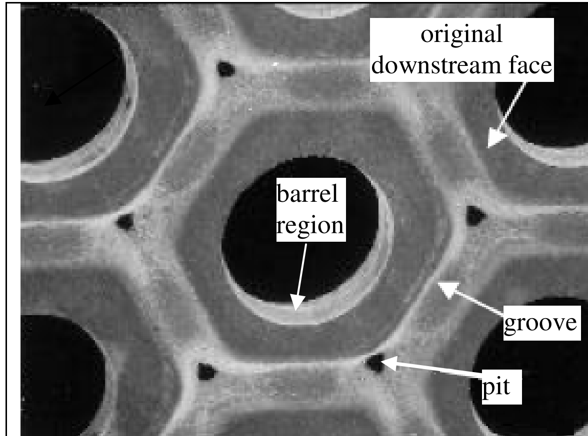


**Figure 1.9: Downstream view of an eroded accelerator grid**[18]

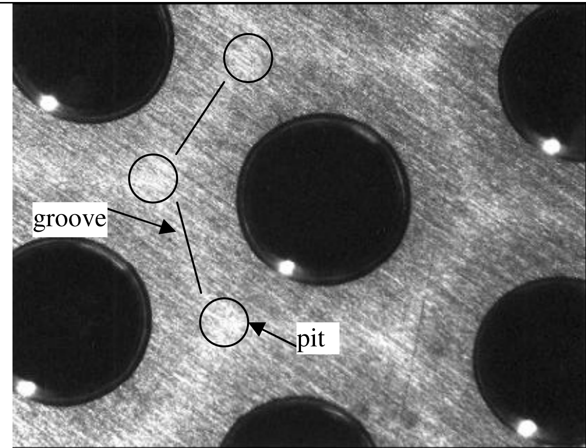


**Figure 1.10: Downstream view of an accel grid beginning to show signs of pit and groove wear**[20]

Sputter erosion of the screen grid is caused by ions in the discharge plasma impinging upon the screen grid's upstream face. The discharge plasma is at a potential $V_{anode}$ (typically 20–30 V) above that of the screen grid. Hence, singly charged ions in the discharge plasma will collide with energies of about 25 eV, which will produce a very small amount of sputtered atoms (if any at all). However, the multiply charged ions that exist in the discharge plasma will impinge with twice as much energy (~ 50 eV) if doubly-charged or three times as much energy (~75 eV) if triply-charged and produce significantly more sputtered atoms than the singly charged ions. While these relatively low energies won't produce a considerable amount of sputtered particles with each impingement, the situation of the screen grid being directly exposed to the discharge plasma for the lifetime of the thruster causes some design concern of erosion.

The sputtered material from the accelerator grid will coat components (where the upstream screen grid face is one surface of most concern) of an ion thruster in the vicinity of the sputtering source. Over time, this material will build up into thin-films that can crack and flake off. These flakes will sometimes become positioned between the two electrode grids, thus causing an electrical short. These shorts are typically "cleared" by applying a pulse of electrical current between the grids so that electric arcing/joule heating occurs in the area of the flakes. These effects usually release enough energy to dislodge the flake or vaporize it, thus clearing the short. If the short cannot be cleared, the power supplies cannot maintain

the grid voltages and thruster failure occurs. These flakes can also become caught in the screen grid, disrupting the carefully designed potential field between the ion optic grids, thus causing an improperly focused beamlet. This can cause direct high energy ion impingement of accelerator grid.

#### 1.3.2.2 Hollow Cathode Sputtering Consideration

The discharge hollow cathode is exposed to the same discharge plasma that the screen grid is and is susceptible to the same sputtering damage, however, the plasma density is much higher near the cathode which causes higher ion flux and higher sputter rates. It is thought by some that most of the erosion noted on the hollow cathode keeper plate (e.g., see Figure 1.11) is due to sputtering by multiply charged ions in the discharge plasma. The hollow cathodes in an ion thruster remain operational as the keeper is eroded away, but may become more prone to failure and off-design operation as the keeper plates erode away, e.g., eventually leading to an inability to start the hollow cathode or operate it in a safe spot mode. As in the case of the grids, the build-up of sputtered films on the surfaces of the hollow cathodes can lead to electrical shorts and render the cathode inoperable if the shorts can not be cleared/vaporized by keeper power supplies.

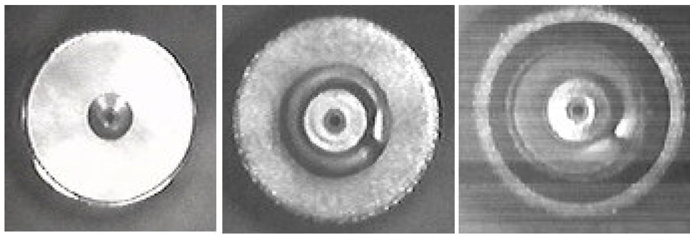

**Figure 1.11: Erosion of cathode keeper plate[21].** *0 hours (left), 11700 hours (middle), 25500 hours (right).*

## 1.4 Summary

Electric propulsion, through its high specific impulse, allows the delivery of greater payload masses to a destination than chemical propulsion. Due to its low thrust nature, an EP device must be able to function for years on end. Major lifetime limiters of an EP device involve low energy (<1000 eV) sputtering processes. It is therefore important to accurately quantify the sputtering processes.

# Chapter 2 Sputtering and Sputtering Models

This chapter will investigate the basic processes and interactions of sputtering, and some numerical/empirical models that help describe the process. Collision cascades are discussed as well as basic factors that change the sputtering yield. The concepts of nuclear and electronic stopping powers and cross sections will be introduced. Descriptions of Sigmund's sputtering model and several variants, including Yamamura's semi-empirical model, will be presented. Differential sputter yields will be discussed. Models presented will analyze total yields at normal incidence, total yields at oblique incidences, and differential yields at both normal and oblique incidences.

## 2.1 Sputtering Process

A typical sputtering event begins when an energetic particle strikes a target surface atom. This particle is often called the incident, primary, or projectile particle. The energetic incident particle loses energy to the target via two mechanisms: elastic nuclear collisions (kinetic energy conserved, atom-on-atom "billiard" ball collisions) and inelastic electronic loses (electronic excitation, ionization, electron-electron collisions). The atoms that collide directly with the incident particle are called primary recoils (or primary knock-on atoms, PKAs). These primary recoil atoms in turn are generally dislodged from their lattice sites (overcoming the lattice displacement energy, $U_d$) and have collisions with yet other target atoms (secondary recoil atoms or 2$^{nd}$ generation recoil atoms), which will collide with yet other target atoms (3$^{rd}$ generation recoil atoms) in a process called a collision cascade. The collision cascade will continue in this way (4$^{th}$, 5$^{th}$,…,n$^{th}$ generation recoil atoms) until all displaced atoms' energies fall below

the level where they can dislodge other bulk atoms (i.e. $U_{atom} < U_d \sim 10$ eV). The whole process is usually over in picoseconds.

A target atom becomes sputtered when it is displaced near the target surface and has a trajectory away from the surface and has sufficient kinetic energy so that it no longer interacts with other target surface atoms (overcoming the surface binding energy, $U_b$), thus escaping and becoming a gas phase sputtered atom. This collision cascade/sputter process is illustrated in Figure 2.1 (shown are three sputtered particles). Sputtering is typically quantified by the *total* sputter yield ($Y$), and is defined as the statistical mean number of sputtered particles per incident particle (units: atoms/incident particle), hence the sputter yield as illustrated in Figure 2.1 is $Y = 3$ atoms/incident particle. The sputter yield is a statistical measure in that an individual incident particle may create more or less sputtered atoms than the value $Y$, but a large group of $N$ incident particles will sputter $Y*N$ atoms. Sputtering can be induced by ions, neutral atoms, neutrons, electrons, molecules, or energetic photons. This document will focus on sputtering by noble gas ions (not chemically reactive) on single component targets (i.e., targets comprised of one element).

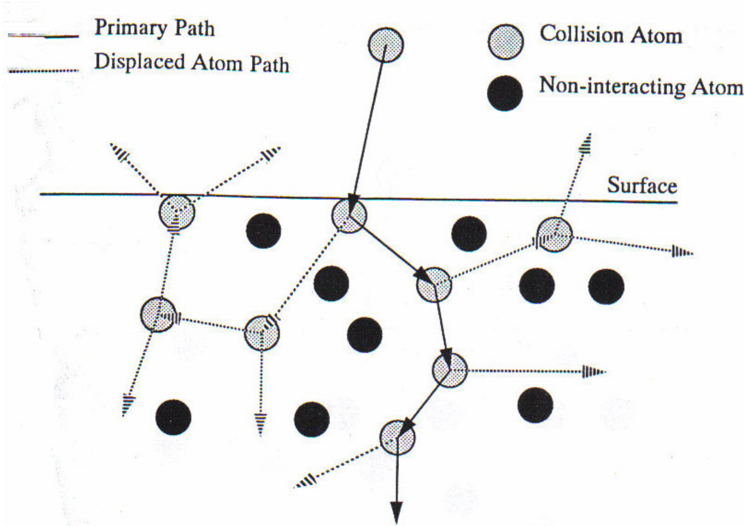


**Figure 2.1: Two dimensional diagram of a typical collision cascade[22].** *Three particles escape the surface for one incident particle giving* Y = 3 *atoms/ion.*

Experiments involving sputtering by atoms or ions require that the incident particle have a well defined energy, which, in the lab, is overwhelmingly accomplished by accelerating ions through controlled electric fields. Due to this methodology, using "ion" to refer to the incident particle is a convenient (though

somewhat misleading) way to discuss sputtering processes and is a convention that this thesis will follow. An ion with an energy less than 10 keV is usually neutralized within 4-6 Å of a target surface[18], while collisional effects don't occur until 10 Å of the surface. Hence, incident particles are, in actuality, all neutral atoms (for the energies discussed in this thesis). At higher energies, it is pointed out that ions can be stripped of most (or sometimes all) of their electrons as they plow deep into a surface and become highly ionized particles.

Sputtering yields depend on several factors relating to the incident ion and target material. These factors include ion mass, ion energy, ion angle of incidence, atomic mass of target atoms, target atomic structure (crystal orientation/lattice system and whether target is polycrystalline, amorphous, or comprised of a single crystal), target surface binding energy, and target texture[23]. Sputtering yields tend to increase with increasing incident ion mass[25]. At incident ion energies below the threshold energy, $E_{th}$, sputtering will not occur. Above $E_{th}$, sputtering yields generally increase with the increase of incident ion energy. At ~ 0.1 MeV, yields will start to decline due to the incident ion's energy being deposited too far away from the surface layer where most sputtered particles originate[24]. Sputtering yields vary with increasing target atomic masses in a cyclical nature, which roughly correlate to the target atom's location on the periodic table[25]. Sputtering yields increase from normal incidence ($\beta = 0°$) with increasing angle of incidence until approximately $\beta = 60°$, where the yield starts declining and reaches a value of zero at $\beta = 90°$. As the angle of incidence increases, more of the ion's energy gets deposited closer to the surface, until the ion is at near glancing incidence when the ion begins to be increasingly repulsed by the target surface atoms[29].

Single crystal targets "tunnel" the collision cascade (due to the repeating crystal lattices) creating the "spot pattern" distributions noted by Wehner as in Figure 1.8, while amorphous and polycrystalline targets behave in a more isotropic manner. Microscopic surface features and texturing create localized changes in the angle of incidence from the bulk of the surface, changing the local yield. These features may "shadow" other areas of the surface (especially at oblique incidences) thus creating localized areas of reduced sputtering[26]. Target materials with higher surface binding energies allow fewer atoms to be sputtered, thus lowering $Y$.

Sputtering is one of many effects that may occur when an energetic ion interacts with a surface. Other possible effects (Figure 2.2) include: secondary electron emission (2), sputtered target atom in an excited or ionized state (3,), desorbed atom (4), adsorption (5), surface diffusion (6), surface reaction (7), incident particle implantation (8), heating (9), photon emission (10), and sputtering of target atom clusters (11). Of the sputtered particles (2, 3, 11), approximately 80-95% are single neutral target atoms, 5-20% are target atomic clusters, 1% are electronically excited target atoms, and 1% are ionized target atoms[28]. Many incident ions (1) remain implanted in the surface (8) at depths of tens of nanometers to just below the surface layer. Other incident ions are adsorbed or reflected from the surface. If an incident ion is chemically reactive, it may react with target atoms (noble gas incident ions do not chemically react, but can be adsorbed onto the surface and entrained into near surface regions). The collisions created by the incident ion may create photonic emission (10), when excited electrons drop to their ground state or electronic emission (2). Much of the incident particle's energy goes into heating the surface (9) via collisions that set target atoms oscillating about their lattice points that eventually relax to their pre-impact state through coupling of phonons into the bulk material of the target.

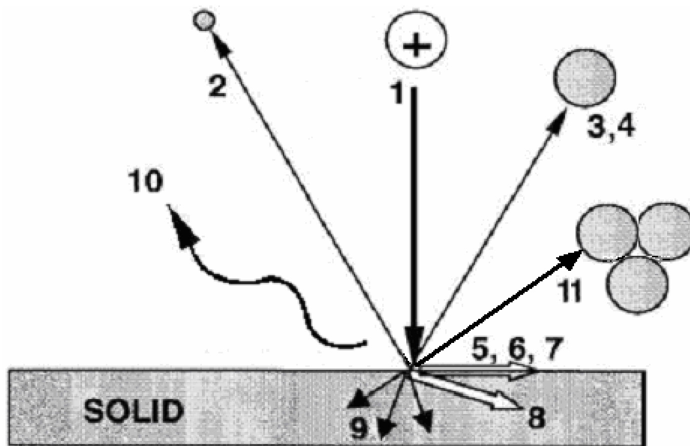


**Figure 2.2: Possible effects with ion bombardment[27].** *2) secondary electron emission 3) sputtering 4) desorption 5) adsorption 6) surface diffusion 7) surface reaction 8) implantation 9) heating 10) photon emission 11) cluster sputtering. (From ref 28.)*

Sigmund[12] has identified three sputtering regimes that can be classified by the incident ion's energy (Table 2, Figure 2.3). In the single knock-on regime, collision cascades are not created. The sputtered particles are created by undergoing a collision with the primary particle and having a very small

number of collisions which direct it toward the surface. The linear cascade regime is characterized by the generation of a full collision cascade, in which interaction of two moving target atoms is negligible. The linear cascade framework lends itself to being described by transport theory. The spike regime produces collision cascades, except that the interaction between moving atoms and other target atoms is no longer negligible. In ion propulsive devices undergoing sputtering at low energy and relatively low flux, most sputtering occurs in the single knock-on regime, with a smaller amount happening in the linear cascade regime. Unfortunately, the single knock-on regime has the least extensive theoretical underpinnings[28] and is also the hardest of the regimes to measure yields experimentally.

**Table 2: Sputtering Regimes**

| Regime | Approx. Energy Range | Characteristic |
|---|---|---|
| Single knock-on | < 1 keV | Only primary recoils are created |
| Linear cascade | 1 keV – 300 keV | 2nd and above generation recoils are created, collisions between moving (displaced) atoms and (1) other atoms and (2) subsequent incoming particles are rare |
| Spike | > 100 keV, also can occur at lower energies when ions arrive at high flux levels | Collision cascade area becomes "molten" (i.e. all atoms are displaced), majority of collisions are between moving particles. Moving particles can be struck by subsequent incoming ions when ion flux is high. |

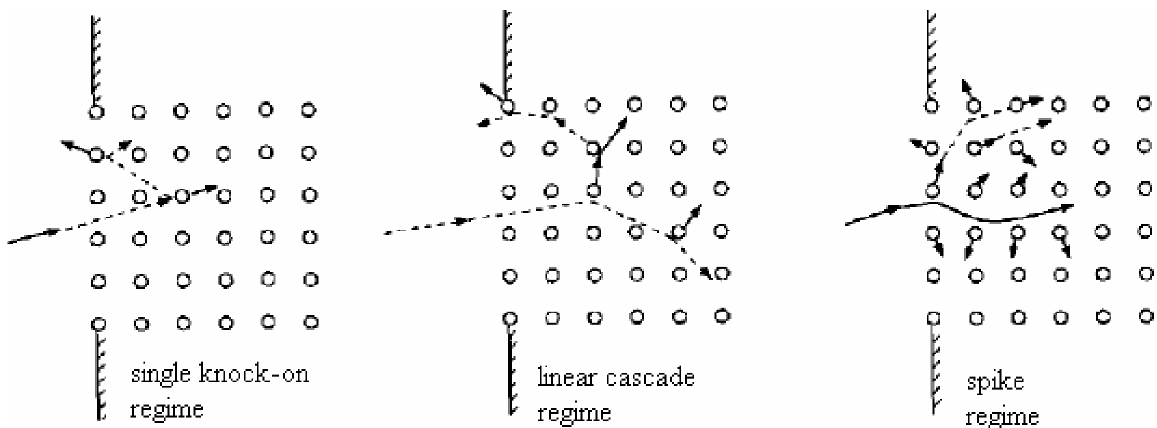


**Figure 2.3: Two dimensional diagrams of the three sputtering regimes[28].**

## 2.2 Sputtering Models

There exist many different sputtering models each tailored to a specific area of study, simplicity, energy range, etc. The rest of this chapter will focus on some of the more common sputtering models

(empirical and theoretical) and also other lesser known models that describe sputtering experiments discussed in this document. The models will be presented and will include varying levels of discussion, statement of basic assumptions, and applicable conditions. The theoretical underpinnings/derivations will not be discussed as these exist elsewhere and would be out of the scope of this thesis.

A basic algorithm to quantitatively analyze the sputtering process consists of four[29] parts: (1) determination of the amount of energy deposited by the energetic incident particles near the surface; (2) determination of how many recoil atoms are created from this energy deposition; (3) determination of how many of these recoil atoms go to the surface; (4) determination of how many of the recoil atoms at the surface have sufficient energy to overcome the surface binding force. An important concept in determining these values is that of cross sections. Cross sections ($\sigma$, units of area) state the probability of a specified interaction occurring between one particle and another.

Cross sections vary as a function of particle energy and particle/target species. High energy ion and atom scattering cross sections are needed to determine parts (1) and (2), while low energy atom scattering cross sections are needed to determine parts (2) and (3). Cross sections in sputtering are divided into two main categories: one involving the elastic nuclear collisions (subscript $n$) called the *nuclear stopping cross section*, $S_n(E)$, and one involving the inelastic electronic interactions (subscript $e$) called the *electronic stopping cross section*, $S_e(E)$. In electric propulsion devices, nuclear stopping cross sections effects dominate. The sum of these cross sections (the *stopping cross section*, $S(E)$) describes the energy loss of an ion as it travels through a target per unit length ($x$) of travel:

$$S(E)N = S_n(E)N + S_e(E)N = \frac{dE}{dx} = \left(\frac{dE}{dx}\right)_n + \left(\frac{dE}{dx}\right)_e \qquad \textbf{(2.1)}$$

There are several methods that estimate the cross section and each method may only be valid in one or two sputtering regimes. Some are based on experiment, others on theory, and yet others a combination of the two. Examples include various Coulomb-based screening radius methods for nuclear cross sections: Thomas-Fermi-Sommerfeld[12,30], Lenz-Jensen, Bohr, Lindhard, and Moleire. For electronic stopping, the Lindhard-Scharff[18,12] and ZBL[31] methods are most commonly used. Several documents[12, 31, **Error! Bookmark not defined.**, 18, 20 (not exhaustive)] exist that discuss different methods to get the cross section values, and

will not be discussed at length here. In these equations parameters with subscripts of "1" will refer to the incident ion, while subscripts of "2" will refer to the target (e.g., $M_1$ is the mass of the incident ion, $M_2$ is the mass of a target atom).

### 2.2.1 Sigmund Total Yield Formula

The Sigmund formula[12] is probably the most widely used to obtain total sputtering yields and is most accurate in the linear cascade regime. It assumes an amorphous or polycrystalline target material, normal ion incidence and is based off of Boltzmann transport theory.

$$Y(E) = \frac{0.042\text{Å}^2}{U_b}\alpha' S_n(E) \qquad \text{For E > 1 keV} \qquad \textbf{(2.2)}$$

$$Y(E) = \frac{3}{\pi^2}\frac{\alpha'}{U_b}\frac{M_1 M_2}{(M_1 + M_2)^2}E \quad \text{For E < 1 keV and E > } 10U_b \qquad \textbf{(2.3)}$$

$M_1$ and $M_2$ are the incident particle atomic mass (amu) and target atom mass respectively. $U_b$ is the surface binding energy (eV). Note that Eqn. 2.3 is a linear approximation.

$$a_I = \frac{0.468\text{Å}}{\left(Z_1^{2/3} + Z_2^{2/3}\right)^{1/2}} \qquad \textbf{(2.4)}$$

$Z_1$ is the incident particle atomic number, $Z_2$ is the target atom atomic number

$$\varepsilon = \frac{M_2 E(eV)}{M_1 + M_2}\frac{a_I}{Z_1 Z_2 e^2} \qquad \textbf{(2.5)}$$

where $e^2$ = 14.4 eV- Å.

$$\alpha' = 0.15 + 0.13\frac{M_2}{M_1} \qquad \textbf{(2.6)}$$

for $\varepsilon$ >1 (ref. 32). If $\varepsilon$ < 1, use figures provided in Sigmund[12]:

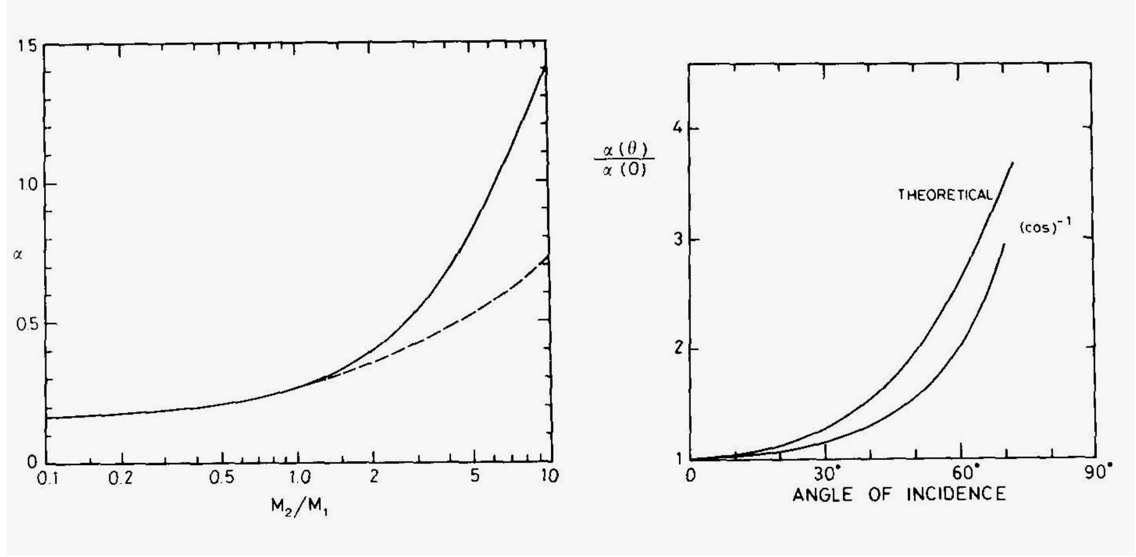


**Figure 2.4: (Left) α' factors for mass ratio at normal incidence, α'(0); (right) and normalized α factors for oblique incidence[29].**

Sigmund[12] used the Thomas-Fermi nuclear cross-section formula for high energy ($\varepsilon$ >1):

$$S_n(E) = 4\pi a_I Z_1 Z_2 e^2 \frac{M_1}{M_1 + M_2} s_n(\varepsilon) \qquad \textbf{(2.7)}$$

with Bohdansky modified[33] Thomas-Fermi screening:

$$s_n(\varepsilon) = \frac{3.441\sqrt{\varepsilon}\ln(\varepsilon + 2.718)}{1 + 6.355\sqrt{\varepsilon} + \varepsilon(6.882\sqrt{\varepsilon} - 1.708)} \qquad \textbf{(2.8)}$$

A simple variation of Sigmund's formula for $\varepsilon$ >1 is proposed by Zalm[32]:

$$Y(E) = \frac{(Z_1 Z_2)^{5/6}}{3U_b}\left[\frac{\frac{1}{2}\ln(1+\varepsilon)}{\varepsilon + 0.14\varepsilon^{0.42}}\right] \qquad \textbf{(2.9)}$$

## 2.2.2 Yamamura & Tawara Semi-Empirical Total Yield Formula

The Yamamura & Tawara (YT) semi-empirical formula[33] is based upon Sigmund's theoretical construct, with modifications made for low energy and fits to experimental/simulation data. YT based their fit parameters on a survey of experimental results and on values returned from their ACAT Monte Carlo

numerical simulation code. The formula is for use with normal incident particles and, as with most sputtering models, is most accurate in the linear cascade regime.

$$Y(E) = .042\frac{Q(Z_2)\alpha^*(M_2/M_1)}{U_b}\frac{S_n(E)}{1+\frac{W(Z_2)}{1+(M_1/7)^3}k_e\varepsilon^{0.3}}\left[1-\sqrt{\frac{E_{th}}{E}}\right]^s \quad \textbf{(2.10)}$$

Where $Q(Z_2)$, $s(Z_2)$, and $W(Z_2)$ are experimental fit parameters (Table 3) and functions of target material. $S_n(E)$, $\varepsilon$, and $s_n(\varepsilon)$ are given in (2.7), (2.5), and (2.8);

$$\alpha^* = \begin{cases} 0.0875(M_2/M_1)^{-0.15} + 0.165(M_2/M_1) & \text{for } M_1 \geq M_2 \\ 0.249(M_2/M_1)^{0.56} + 0.0035(M_2/M_1)^{1.5} & \text{for } M_1 \leq M_2 \end{cases} \quad \textbf{(2.11)}$$

$$E_{th} = \begin{cases} 6.7\frac{U_b}{\gamma} & \text{for } M_1 \geq M_2 \\ \left(\frac{1+5.7(M_1/M_2)}{\gamma}\right)U_b & \text{for } M_1 \leq M_2 \end{cases} \quad \textbf{(2.12)}$$

$$\gamma = \frac{4M_1M_2}{(M_1+M_2)^2} \quad \textbf{(2.13)}$$

$$k_e = 0.079\frac{(M_1+M_2)^{3/2}}{M_1^{3/2}M_2^{1/2}}\frac{Z_1^{2/3}Z_2^{1/2}}{\left(Z_1^{2/3}+Z_2^{2/3}\right)^{3/4}} \quad \textbf{(2.14)}$$

**Table 3: $U_b$, $Q(Z_2)$, $W(Z_2)$, $s(Z_2)$ from Yamamura and Tawara[33]**

| target | $Z_2$ | $U_b$ | Q | W | s |
|---|---|---|---|---|---|
| Be | 4 | 3.32 | 1.66 | 2.32 | 2.5 |
| B | 5 | 5.77 | 2.62 | 4.39 | 2.5 |
| C | 6 | 7.37 | 1.70 | 1.84 | 2.5 |
| Al | 13 | 3.39 | 1.0 | 2.17 | 2.5 |
| Si | 14 | 4.63 | 0.66 | 2.32 | 2.5 |
| Ti | 22 | 4.85 | 0.54 | 2.57 | 2.5 |
| V | 23 | 5.31 | 0.72 | 2.39 | 2.5 |
| Cr | 24 | 4.10 | 0.93 | 1.44 | 2.5 |
| Mn | 25 | 2.92 | 0.95 | 0.88 | 2.5 |
| Fe | 26 | 4.28 | 0.75 | 1.20 | 2.5 |
| Co | 27 | 4.39 | 1.02 | 1.54 | 2.5 |
| Ni | 28 | 4.44 | 0.94 | 1.33 | 2.5 |
| Cu | 29 | 3.49 | 1.0 | 0.73 | 2.5 |
| Ge | 32 | 3.85 | 0.59 | 2.08 | 2.5 |
| Zr | 40 | 6.25 | 0.54 | 2.50 | 2.8 |
| Nb | 41 | 7.57 | 0.93 | 2.65 | 2.8 |
| Mo | 42 | 6.82 | 0.85 | 2.39 | 2.8 |
| Ru | 44 | 6.74 | 1.31 | 2.36 | 2.5 |
| Rh | 45 | 5.75 | 1.14 | 2.59 | 2.5 |
| Pd | 46 | 3.89 | 0.85 | 1.36 | 2.5 |
| Ag | 47 | 2.95 | 1.08 | 1.03 | 2.8 |
| Sn | 50 | 3.14 | 0.47 | 0.88 | 2.5 |
| Tb | 65 | 4.05 | 0.90 | 1.42 | 2.5 |
| Tm | 69 | 2.42 | 0.65 | 0.85 | 2.5 |
| Hf | 72 | 6.44 | 0.65 | 2.25 | 2.5 |
| Ta | 73 | 8.1 | 0.56 | 2.84 | 2.8 |
| W | 74 | 8.9 | 0.72 | 2.14 | 2.8 |
| Re | 75 | 8.03 | 1.03 | 2.81 | 2.5 |
| Os | 76 | 8.17 | 1.11 | 2.86 | 2.5 |
| Ir | 77 | 6.94 | 0.96 | 2.43 | 2.5 |
| Pt | 78 | 5.84 | 1.03 | 3.21 | 2.5 |
| Au | 79 | 3.81 | 1.08 | 1.64 | 2.8 |
| Th | 90 | 6.2 | 0.63 | 2.79 | 2.5 |
| U | 92 | 5.55 | 0.66 | 2.78 | 2.5 |

### 2.2.3 Oblique Ion Incident Total Yield Models

Total yields from off-normal sputtering (oblique, Figure 2.5) increase as the angle of incidence increases due to more energy becoming increasingly available in the near surface region until a maximum is reached and then the yield quickly drops to zero by as $\beta$ approaches 90° (Figure 2.7). Sigmund's analysis[29] suggests the following model for $0< \beta < 70°$:

$$Y(\beta) = Y(0)\cos^{-f}(\beta) \quad \textbf{(2.15)}$$

Where *Y(0)* represents the yield at normal incidence and *f* (Figure 2.6) is a parameter that is based upon atomic spatial moments[29]; a good approximate value is 5/3. The Sigmund analysis does not predict the measured drop in yield near $\beta = 90°$. The *f* parameter can also be experimentally determined by plotting $\ln(Y(\beta)/Y(0))$ vs. $\cos(\beta)$ and taking the slope to be equal to $-f$.

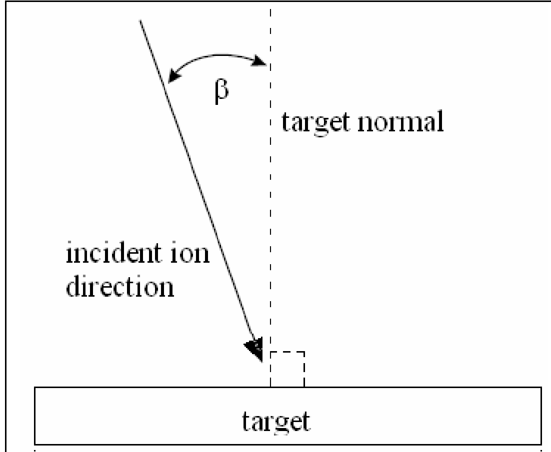


**Figure 2.5: Definition of oblique angle $\beta$**

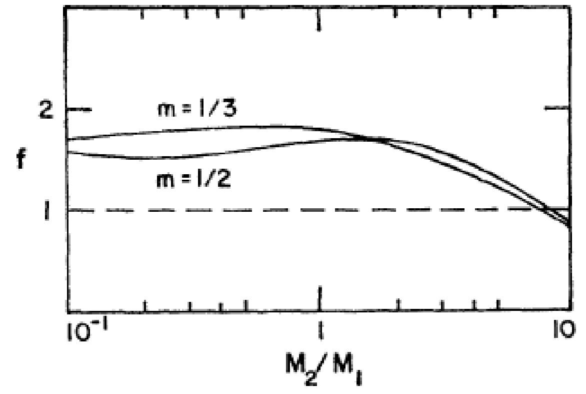


**Figure 2.6: f parameter, m = ½ for E>5keV, m = 1/3 for E<5 keV (approximate values) from [ref 29]**

Yamamura[34] also modified Sigmund's oblique sputter yield model to attempt to account for the drop in yield near $\beta = 90°$:

$$Y(\beta) = Y(0)\cos^{-f_y}(\beta)\exp\left[-B\left(\cos^{-1}(\beta) - 1\right)\right] \quad \textbf{(2.16)}$$

where *B* and $f_y$ are adjustable parameters and are related by the angle of incidence where the maximum total yield occurs ($\beta_{opt}$, Figure 2.7)[34]:

$$\beta_{opt} = \mathrm{acos}\left(\frac{\mathrm{B}}{f_y}\right) \quad \textbf{(2.17)}$$

Yamamura fit a curve[34] to several *f* parameters (based on Sigmund, [2.15]) and related it to $E_{th}/E$:

$$f_y = f\left[1 + 2.5\frac{(E_{th}/E)^{1/2}}{1 - \left((E_{th}/E)^{1/2}\right)}\right] \quad \textbf{(2.18)}$$

where *f* is the value predicted by the Sigmund model [2.15].

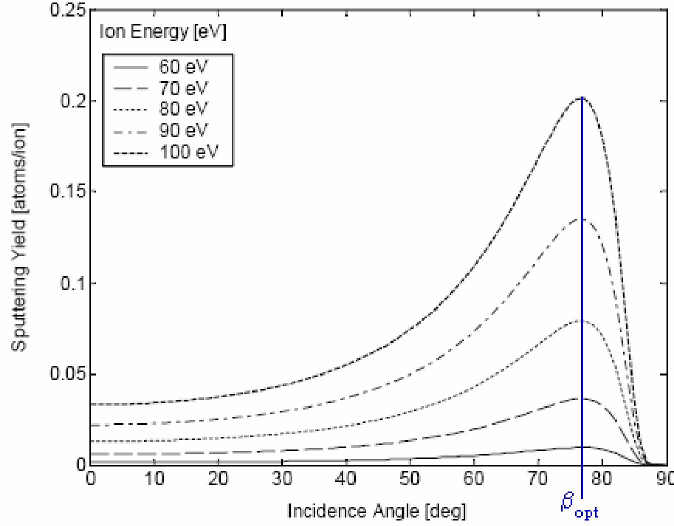


**Figure 2.7: Typical plot of total yield vs. incidence angle from [ref 20, $Xe^+$ on Mo].**

Zhang[35] derived a modified version of Yamamura's 3D model[36] (introduced and discussed in more detail in Section 2.2.4 below):

$$Y(\beta) = 0.042 \frac{\alpha'(M_2 / M_1, \beta) S_n(E)}{U_b} \left[ 1 - \left( \frac{E_{th}}{E} \right)^{1/2} \cos\beta \right] \tag{2.19}$$

This equation relies on the *α'* term to account for the drop in yield near glancing incidence, which does not occur in the theoretical constructs (see Figure 2.4, right) as the ratio approaches infinity at $\beta = 90°$.

## 2.2.4 Differential Sputter Yields and Models

Until this point, only total sputter yields (*Y*) have been discussed. Another important parameter used to describe the sputtering process is that of the spatial *differential* sputter yield ($y(\alpha, \phi)$ or $dY/d\Omega$) which describes the number of sputtered atoms per incident ion, that end up traveling away from the surface in a particular direction (solid angle, $\Omega$). Differential sputter yields (i.e. "angular emission distribution of sputtered particles") have units of atoms/ion/steradian and are functions of both polar ejection angle ($\alpha$) and azimuthal ejection angle ($\phi$) as shown in Figure 2.8. A second type of differential sputtering yield often mentioned in literature is that of *energetic* differential yield ($y(E)$ or $dY/dE$), which describes the number of sputtered atoms per incident ion with a certain kinetic energy (i.e. "energy

distribution of sputtered particles"). This thesis will focus on the spatial differential yield and any further reference to the differential yield will be implied to mean that of the spatial differential yield.

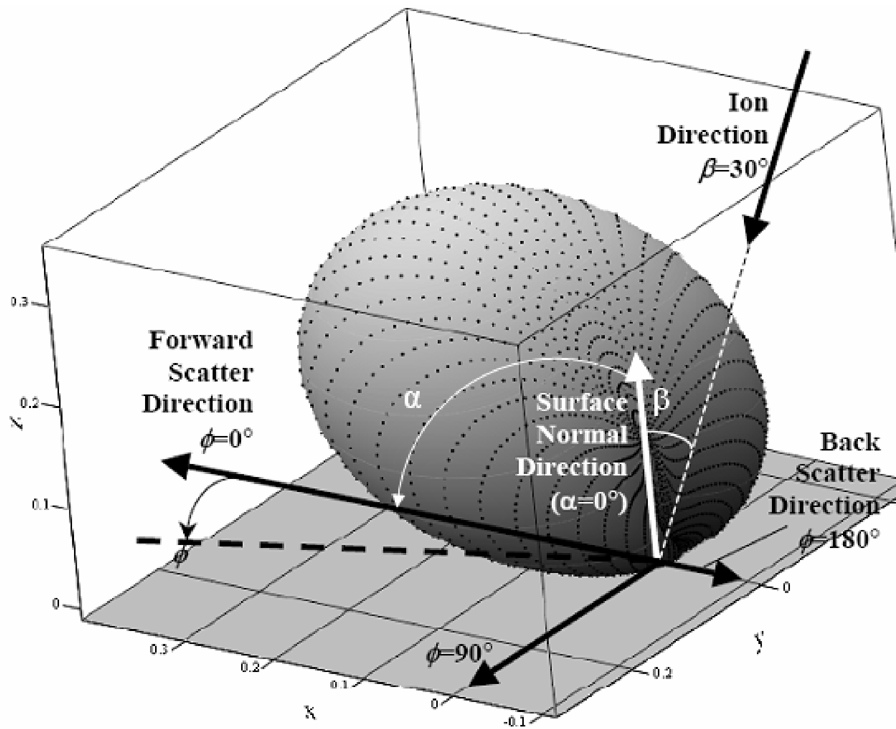


**Figure 2.8: 3D spherical plot of a differential yield distribution with definitions of *α*, *β*, and *ϕ*[37].**

Differential yields are important parameters because they provide deeper insight into the veracity of proposed sputtering yield theories and formulae than total yield measurements can provide[38]. Differential sputter yields are also important for modeler attempting to account for re-deposited material. Examples are seen with Seeliger/Sommermeyer and Wehner's spot patterns as described in 1.3.1 of this document. The angular distribution predicted by Sigmund's theory is a diffuse or cosine distribution, $y(\alpha) = Y(E)cos^d(\alpha)/\pi$, which is independent of incidence angle[38] or azimuthal angle. The cosine distribution is often roughly valid at moderate to high energy, but is not observed experimentally at low energies. Hence, the differential yield data indicate that Sigmund's theory is not adequate to encompass low energy sputtering.

In electric propulsion and as mentioned above, differential yield data are useful in determining thruster locations where sputtered material can deposit. Such deposits can lead to build-up and flaking that may cause electrical or contamination problems. Thus, the differential yield data are of paramount importance when determining where equipment sensitive to surface contamination (e.g. optical devices and

photovoltaics) can be located. The lifetime of some sputtered devices may be higher than predicted when using an erosion analysis tool based solely on total yields due to unanticipated re-coating from other sputtered surfaces. A model incorporating differential yield information would be able to determine total sputtered particle fluxes from one surface to another, and thus result in a more accurate lifetime prediction. Also, when designing vacuum chamber beam dumps used in ion engine testing, the differential yield data could be used to determine the optimum orientation of surfaces that minimizes deposition of back-sputtered beam dump material onto EP test devices, thereby considerably improving the quality of wear test measurements. Accordingly, differential yield data can be used to significantly increase the accuracy of ion optics wear models. In terrestrial applications, an accurate differential sputter model could help optimize film deposition uniformity, minimize waste and reduce contamination in semiconductor manufacturing.

Yamamura (as shown in Zhang[35]) derived an analytic model for the description of differential yield distributions based on Sigmund's theory:

$$y(E,\beta,\alpha,\phi) = 0.042\frac{\alpha'\left(\frac{M_2}{M_1},\beta\right)S_n(E)}{U_s} \times\left[\cos\alpha\left[1-\frac{1}{2}\left(\frac{E_{th}}{E}\right)^{1/2}\left\{\cos\beta G(\alpha)+\frac{3}{4}\pi\sin\beta\sin\alpha\cos\phi\right\}\right]\right] \quad \textbf{(2.20)}$$

$$G(\alpha) = \frac{3\sin(\alpha)^2-1}{\sin(\alpha)^2}+\frac{\cos(\alpha)^2\left(3\sin(\alpha)^2+1\right)}{2\sin(\alpha)^3}\ln\left(\frac{1+\sin\alpha}{1-\sin\alpha}\right) \quad \textbf{(2.21)}$$

Zhang[35] modified Yamamura's equation to account for some perceived errors with regard to $E_{th}$:

$$y(E,\beta,\alpha,\phi) = 0.042\frac{\alpha'\left(\frac{M_2}{M_1},\beta\right)S_n(E)}{\pi U_s} \times\left[\cos\alpha\left[1-\frac{1}{4}\left(\frac{E_{th}}{E}\right)^{1/2}\left\{\cos\beta G(\alpha)+\frac{3}{2}\pi\sin\beta\sin\alpha\cos\phi\right\}\right]\right] \quad \textbf{(2.22)}$$

which when integrated over a hemisphere to obtain the total yield results in an expression for total yield as a function of ion incidence [2.19]

Roosendaal and Sanders (as described in Whitaker[39]) proposed a similar model (with $n$ = 1; $n$ is a fitting parameter Whitaker added) based on Sigmund's theory that accounted for the anisotropic distributions seen in experimental data:

$$y(E,\beta,\alpha,\phi) = B(E)\cos(\alpha)^{n} \times\left\{1 + 6U^{1/2}(\gamma E)^{-1/2}\left[-\cos\beta F(\alpha) + \frac{3\pi}{8}\sin\beta\sin\alpha\cos\phi\right]\right\} \qquad \textbf{(2.23)}$$

$$F(\alpha) = \left[\frac{2-3\cos(\alpha)^{2}}{4\sin(\alpha)^{2}} - \frac{\cos(\alpha)^{2}}{2\sin\alpha}\left(1+\frac{\cot(\alpha)^{2}}{4}\right)\log\left(\frac{1-\sin\alpha}{1+\sin\alpha}\right)\right] \qquad \textbf{(2.24)}$$

*B(E)* varies the intensity of the function and can be measured experimentally. *U* is an energetic measure of the disruption that occurs near the surface at the time of particle ejection and could be interpreted as $U_b$ but is seen to vary with ion energy.

## 2.3 Summary

The physical processes that occur during sputtering are complex and present a challenge to being accurately modeled. As such, many models of varying complexity, with differing assumptions, and differing levels of success have been developed. Differential sputter yields are important data to obtain via experiment and to be modeled as they help to refine the theories of sputtering and improve computer models of EP erosion and lifetime prediction.

# Chapter 3 Methods for Measuring Sputter Yields

The main techniques used to obtain total and differential sputtering yield measurements are presented in the following sections. The first section of this chapter will investigate the methods used to obtain the total sputtering yield.

## 3.1 Total Sputtering Yields

A vast majority of the sputtering yields that have been reported are for total yield (i.e. how many surface atoms are ejected per incident ion). This section describes several methods[41,40] of obtaining total sputtering yields and will be divided into four main categories: weight loss, depth profiling, gas phase spectroscopy, and accumulation on an adjacent surface.

### 3.1.1 Weight Loss

Due to the simplicity, the most common measurement method for obtaining total yields is the weight loss technique. By accurately weighing a target sample before and after being sputtered, and by accurately keeping track of the number of ions hitting the target ($N_{ion}$), one can easily obtain a total sputtering yield:

$$Y = \frac{m_f - m_i}{(M_t)(N_{ion})} N_A \qquad \textbf{(3.1)}$$

where $m_f$ is final mass of target sample, $m_i$ is the initial mass, $N_A$ is Avogadro's number, and $M_t$ is the atomic mass of the target material (in amu).

This method requires that a relatively large number of target atoms be sputtered (i.e. one must run an experiment for extended times and at high ion current densities) in order for a microbalance scale (sensitivities ~ 5 μg) to detect a change in target mass[41]. Due to the nature of the measurement, any yield data obtained will be a summation of all effects that went on during the sputtering (i.e., transient effects are smeared into one constant result). Other considerations when using this type of measurement technique include being aware of any contaminations of the target (ion implantation during measurement, dust particles present on surface during weighing, etc.) and being aware of any effects that may interfere with the counting of the number of ions hitting the target (e.g., Auger and secondary electron emissions from the target when one attempts to measure ion current to the target surface).

A variation on the weight loss method described above, is the use of in-situ gravimetric microbalances (with sensitivities ~0.1 μg) during the sputtering process[41]. The obvious advantage to this is that the change in target weight can be monitored continuously during the sputtering process and transient effects can be discerned, unlike the method described above. This particular measurement technique has not been widely used because of the intricacy of the system involved and because of the existence of other, more attractive in-situ measurement techniques[41].

### 3.1.2 Depth Profiling

Depth profiling uses various techniques to measure the thickness (or similarly, the areal density) of a sputtered area. Changes in the thickness of the sputtered area are interpreted to be a sputtered away volume, thus allowing the number of sputtered particles to be obtained.

Rutherford Backscattering (RBS) is a technique that uses a high energy ion beam (usually ~2 MeV $He^+$) to probe a thin film target[41,42]. The ions travel into the thin film and have inelastic electronic collisions with target atom valence electrons, until it completely stops inside the thin film or, until it has an elastic collision with a target atom nucleus (at depth $z$) causing it to "backscatter" out of the thin film (still having inelastic collisions with target atom valence electrons, Figure 3.1). These backscattered atoms are then collected with a particle detector that is at a fixed relative angle to the ion beam. The detector "counts" a particle and measures the kinetic energy that the particle has.

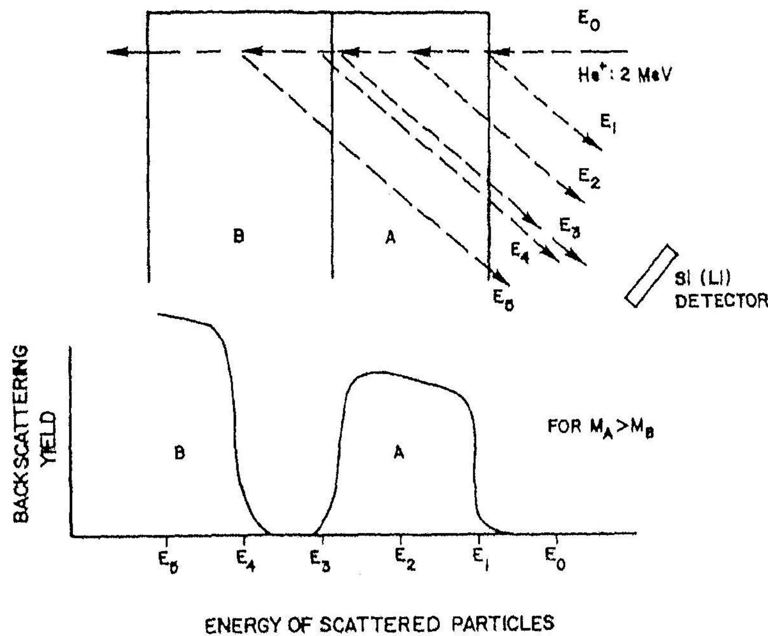


**Figure 3.1: Obtaining RBS spectrum ($E_1$>$E_2$>$E_3$, etc.)[41].**

Due to the energy lost via inelastic collisions on the particle's way in and out, and in the elastic backscattering collision with the target atom, the deeper the particle penetrates the thin film, the lower the energy will be measured. Using the collected energy spectrum, knowing the stopping power of the thin film, and using momentum transfer equations, the areal density ($Nz$, atoms/cm$^2$ in a plane perpendicular to the surface of the thin film) can be calculated. By monitoring the change in the areal density of the thin film, the total sputtering yield is calculated[57]:

$$Y = \frac{dA_{sputter}(\Delta Nz)q}{dJ_B(\Delta t)} \quad \textbf{(3.2)}$$

where the term $dJ_B/dA_{sputter}$ is the ion flux (number of arrival sputtering ions per area) on a differential thin film surface element, $q$ is the electronic charge, and $t$ is time. To clarify, there are typically two different bombarding ion species in these sputtering measurements: 1) the high energy $He^+$ beam used to probe the areal density and 2) the beam used to sputter the target.

The technique of Proton Induced X-Ray Emission (PIXE) is very similar to RBS in that a high energy particle ($H^+$) is used to probe a target, while an x-ray detector collects the generated x-rays[41,43]. The intensity of the x-ray is proportional to the areal density. PIXE needs absolute yield data in order to

calibrate the proportional x-ray intensity signals to a true yield. This is often done using the yields provided via RBS measurements. PIXE has worse depth resolution than RBS[44] (although probing depth is higher than RBS), but PIXE has the ability to detect separate elemental species for multi-component sputtering via emitted Auger electrons (if an electron detector is present). Auger spectrometry can also be used to detect areal density by assuming higher intensity peaks are related to a thicker film.

Another method of obtaining sputter yields[67] is that of using a transducer (profilometer) to measure the surface topography of a target (Figure 3.2). The concept is that if the surface topography is known before sputtering and after sputtering, the sputtering yield can be determined by assuming that the volume of missing material ($V$) was sputtered and that the target density ($\rho$, atoms/cm$^3$) is constant:

$$Y = \frac{V\rho q}{J_B(\Delta t)} \quad \textbf{(3.3)}$$

where $J_B$ is the ion beam current, and $q$ is the electronic charge. Optical styli can give a depth resolution of 0.1 nm, while typical contact styli have ~ 1 nm resolution (with the exception being the atomic force microscope that can obtain resolutions several orders of magnitude better). Typical monolayer thicknesses are on the order of a few Angstroms to tens of Angstroms, hence the absence of a sputtered away monolayer of atoms is usually detectable.

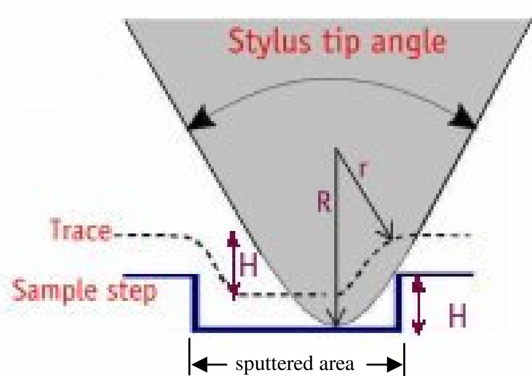


**Figure 3.2: Profilometer measuring sputtered area[45].**

Unfortunately, the profile method can not dynamically determine sputter yields, and the most accurate measurements are made while the sample is in a high vacuum environment to minimize the accumulation of oxide layers on the target surface that occur when it is exposed to atmospheric gases. In

the act of bombarding the target with ions, the density of the target material may change. In addition, styli that make physical contact with the sample may damage it. These effects add some error into the measurement.

In a similar manner, a laser interferometer[Error! Bookmark not defined.,41] may be used to probe the depth of a point on a sputtered area with the reference beam monitoring an un-sputtered area of the target to determine the sputter yield dynamically (Figure 3.3). With care, this method can result in 1 nm depth resolution[41], however, the target must have a reflectivity such that the laser parameters can be detected, and the beams reflected off of the target must leave the wavelengths unchanged[41]. The depth sputtered, $z$, is related to the phase difference ($\phi$), and the laser wavelength ($\lambda$)[41]:

$$z = \frac{\lambda \phi}{4\pi} \quad \mathbf{(3.4)}$$

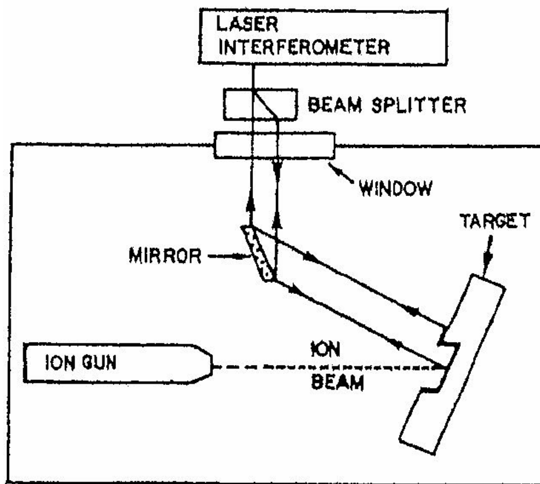


**Figure 3.3: Laser interferometer set-up to measure sputtered depth[41].**

Instead of attempting to measure changes in sputtered depth, another method[Error! Bookmark not defined.] uses a thin film of known thickness ($z$, often measured using RBS), area ($A$), and density on a substrate of differing material while monitoring the time to sputter through the thin film (Figure 3.4). The sputtered particles are monitored using a spectrometer, and when particle optical emissions coming from sputtered substrate atoms are noted, it is assumed that the thin film of known thickness has been sputtered through. The amount of time to reach this point is recorded and a sputter yield can be determined:

$$Y = \frac{\rho A z}{J_B (\Delta t)} \tag{3.5}$$

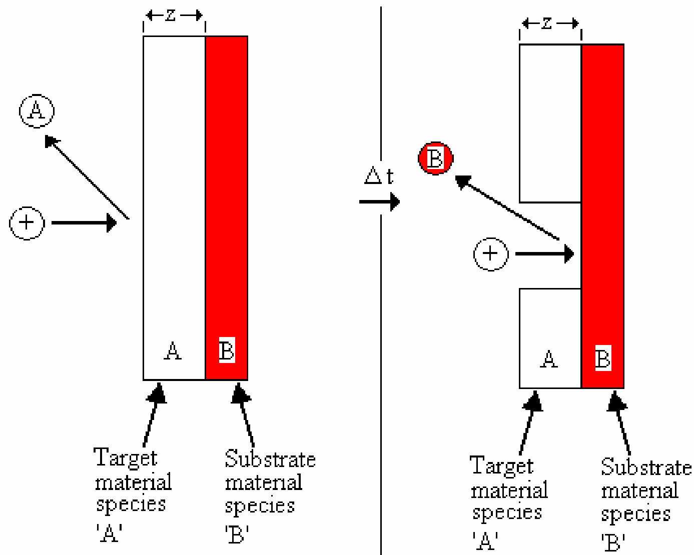


**Figure 3.4: Film 'A' of known thickness is sputtered for time, Δt, until substrate 'B' is detected in the gas phase.**

## 3.1.3 Gas Phase Spectroscopy

Gas phase spectroscopy measures the number particles that have been sputtered away before they re-condense on other surfaces. Optical spectroscopy measures the number of gas phase particles by monitoring the emission of light (induced or naturally occurring) from sputtered particles. Mass spectrometry uses ionized particles in the gas phase to obtain a measurement.

One technique to measure sputter yields using lasers is that of Cavity Ring-Down Spectroscopy (CRDS)[46]. This spectrographic method detects the concentration of sputtered species in the gas phase above the target in the laser beam's line of sight. CRDS is based on the Beer-Lambert law which states that the intensity of light transmitted ($I_t$) through an absorbing medium is related to the intensity of the incident light ($I_0$) as:

$$I_t = I_0 \exp(-\sigma l N) \tag{3.6}$$

where $\sigma$ is the absorbance cross section, $l$ is the length the light travels through the absorbing medium, and $N$ is the number density of the absorbing particles.

In CRDS sputter measurement (Figure 3.5), the frequency of a laser pulse (ν) is tuned such that it matches an absorption line in the spectrum of the sputtered species being measured. The density of sputtered species in the gas phase is typically too low to absorb a detectable amount of light on a single pass. However, if the laser beam is placed between two highly reflective mirrors ($R$ > .999), the beam will take many passes (~1000 to 10,000) through the gas phase region, thus allowing differences in intensity to be discerned by dramatically increasing $l$. The region between the two mirrors is referred to as the optical cavity.

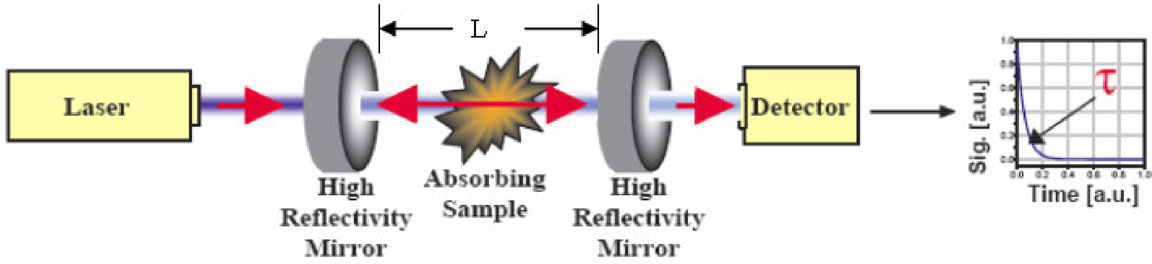


**Figure 3.5: Simplified CRDS set-up showing ring down signal[46].**

Due to the mirrors not having a reflectivity of $R$ = 1, a small amount light will be lost during the pulse's interaction with the mirror on each pass. If a detector is placed outside the optical cavity, the intensity of this lost light can be measured and plotted versus time. The intensity of the detected signal decays exponentially with time as[46]:

$$I(t) = I_0 \exp\left(\frac{-t}{\tau}\right) \quad \textbf{(3.7)}$$

where $\tau$ is the decay constant and can be determined by using curve fits to the ring-down signal. If the decay constant of the optical cavity is determined with no absorbing sample ($\tau_0$), then the absorbance, $A$, can be calculated[46]:

$$A = \frac{L}{c}\left(\frac{1}{\tau} - \frac{1}{\tau_0}\right) \quad \textbf{(3.8)}$$

where $L$ is the length of the optical cavity, and $c$ is the speed of light.

Tuning the laser's frequency around the absorption peak in question will give a plot of A(ν) from which the sputtered species' total number density along the optical cavity can be calculated. To obtain

sputtering yields, the number density of the particles must be known in a plane above the target. These densities can be measured directly by changing the position of the optical cavity in the plane in question or symmetry arguments may be imposed in certain situations in which only one optical cavity position density measurement needs are made.

Another laser based spectrographic method for in-situ measurement of sputtering yields is Laser Induced (Excited) Fluorescence (LIF)[39]. In this method, a laser beam is tuned to a frequency such that it puts the measured species' atoms in an excited state. The electron in the excited level will then drop back to the unexcited state after several nanoseconds and, in the process, emit a photon of a known frequency (fluorescence). An optical spectrometer placed perpendicular to the laser beam then measures this fluorescence spectrum. From this spectrum, data such as particle velocity and number density can be obtained. Particle velocity is obtained by observing the broadening and shifting of the fluorescence spectrum and is a relatively straightforward measurement to make. In order to obtain the number densities (and hence sputtering yields), detailed knowledge of hard to obtain atomic energy level populations and quenching rates are required[41]. Calibration of the LIF signal to absolute yield data can also be used to obtain absolute sputtering yields when angular distribution assumptions are made. Some sputtered particles already leave the surface in an excited state and therefore the same spectrographic measurement techniques can be used without the use of a laser, if there is a detectable amount of fluorescing occurring.

A non-laser based spectrographic technique is called Secondary Neutral Mass Spectrometry (SNMS). In this method, the neutral gas phase target atoms that have been sputtered (the majority of sputtered particles) are ionized and then collected by a mass spectrometer[17,47]. The intensity of the measured signal is proportional to the sputter yield (assuming an angular distribution), but requires calibration through other absolute yield measurement techniques, such as RBS. A similar technique is Secondary Ion Mass Spectrometry (SIMS)[48], where charged gas phase target atoms (i.e. ions) that have been sputtered are collected by the mass spectrometer. SNMS has the advantage of being more quantifiable than SIMS, while SIMS has a lower detection limit than SNMS[17].

Nuclear Recoil Implantation (NRI) is a radiographic technique where the first few μm of a surface is made radioactive by implanting radioactive nuclei in a target[49]. During sputtering, the intensity of the

radioactive signal will decrease[50] (over and above the expected signal decay due to the natural half-life of the radioactive particle), and thus a sputter yield can be measured.  Surface Layer Activation (SLA) is a similar technique that bombards a target with protons of energy on the order of 10 MeV, creating radioactive isotopes of the target material in the first few μm of the target surface[51].  Alternatively, instead of activating the first few microns of a target, the target bulk may be made radioactive by exposing it to a nuclear reactor with a high neutron flux.

### 3.1.4 Accumulation

Other methods make use of the condensation (accumulation) of sputtered particles on adjacent surfaces.  Often this is accomplished by placing a collecting enclosure over the target[20].  An aperture is provided in the enclosure for the incident ion beam to pass through.  Sputtering occurs for a length of time that is sufficient for a detectable thin layer to form on the enclosure's inner surface, but not so long that the film flakes.  The film's thickness on the enclosure's surface can be measured with depth profiling techniques and a sputtering measurement can be determined if the sticking coefficient of the sputter particle to the enclosure is known.  This method has been widely used to obtain completely spatially resolved sputtering yields (radial and azimuthal). A device called the quartz crystal microbalance (QCM), and also referred to as a quartz oscillator microbalance, can be used to measure total yield as either an accumulation device or a weight-loss device. QCMs are described in more detail in the following section.

## 3.2 *Quartz Crystal Microbalance*

The method used to obtain sputter yields presented in this thesis involves the Quartz Crystal Microbalance (QCM).  This technique is based on monitoring the resonance frequency of a piezoelectric quartz crystal and can detect changes in mass on the order of 1 ng/cm$^2$ of sensor area (assuming a 0.1 Hz instrument resolution)[18].  The typical QCM has a disc made of quartz that has one metallic electrode on each side of the disc (Figure 3.6).  When periodic, pulsed voltage is applied between these electrodes, the bulk crystal oscillates at the material's resonant frequency (due to the piezoelectric nature of quartz).

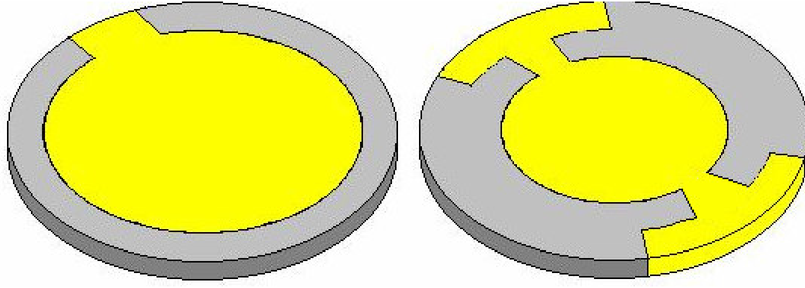

**Figure 3.6: Quartz crystal (grey) and electrode placement (gold) used in a typical microbalance [iNANO, http://www.inano.dk/sw2524.asp].**

If an amount of mass is uniformly added to one of the electrode surfaces, the crystal will oscillate at a lower resonant frequency. Conversely, if material is removed from the electrode, it will oscillate at a higher resonant frequency. Hence, changes in the resonant frequency are interpreted as changes in mass as related by the Sauerbrey equation[52]:

$$\Delta f = -C_f \frac{\Delta m}{A} \qquad \textbf{(3.9)}$$

where Δm is the change in mass, Δf is the change in resonant frequency, *A* is the active crystal area, and $C_f$ is a constant incorporating material properties of the crystal[18]:

$$C_f = \frac{2nf_0^{\ 2}}{\sqrt{\rho_c \mu_c}} \qquad \textbf{(3.10)}$$

where *n* is the resonant harmonic (typically *n*=1), $f_0$ is the resonant frequency of the crystal material, $\rho_c$ is the mass density of the crystal, and $\mu_c$ is the shear modulus of the crystal.

Figure 3.7 is an electrical model[52] of a QCM device where the QCM is assumed to consist of a resistor ($R_m$), that represents the vibrational losses due to the QCM mounting, an inductance ($L_m$) that is related to the oscillating mass of the quartz crystal system (the quartz crystal mass and deposition mass), a capacitance ($C_m$) that represents the stored vibrational energy of the quartz crystal (related to its elasticity), and a second capacitance ($C_0$) which represents all of the capacitance losses in the QCM system (electrode, holder, wiring, etc.). When a mass is uniformly added to the surface of the crystal's electrodes, $L_m$ increases.

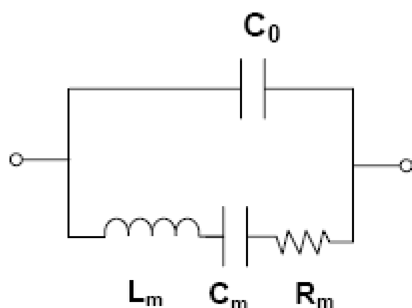


**Figure 3.7: Electrical model of a QCM[52].**

Some concerns[Error! Bookmark not defined.,41] arise from the use of a quartz crystal microbalance. The first is that of the need to have a uniformly coated deposition on the crystal surface because of the assumptions made in the simple resonance model. Although this is a valid concern it is pointed out that there are more complicated models[18] that allow non-uniform coatings to be accounted for without loss of mass resolution. A second major concern is that changes in temperature will cause small changes in the density of the quartz material, thus causing small but detectable changes in the resonant frequency not due to an actual mass change. A way to minimize the sensitivity of the quartz crystal to temperature changes is to use the AT cut crystal (AT cut shown in Figure 3.8), which is designed to drastically reduce (compared to the X cut) the effect changes in temperature near 25°C has on resonance.

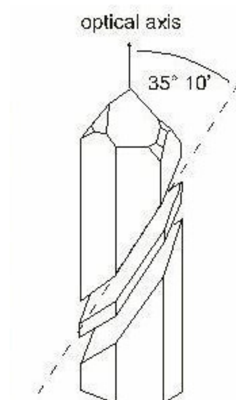


**Figure 3.8: AT cut crystal[53]**

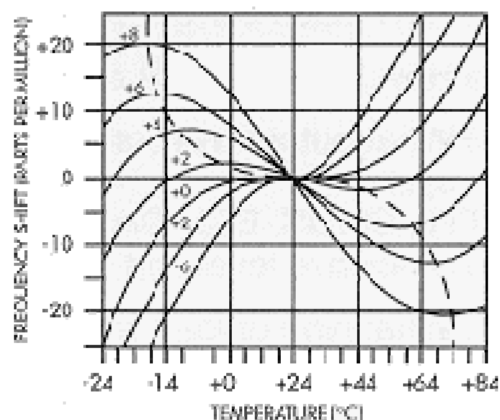


**Figure 3.9: Frequency shift with change in temperature with AT cut crystal[54]**

Changes in resonant frequency due to changes in temperature with the AT cut quartz are on the order of 3 Hz/°C (or 19.6 ng/°C for a sensor with an active area of 0.535 $cm^2$) near room temperature[18]. Accurate temperature calibration charts can be used to correct for unavoidable excursions from room

temperature (Figure 3.9). Figure 3.10 shows two temperature-frequency shift curves before and after a thin film was deposited onto a QCM[55]. It is seen that through a majority of the temperature range (20°C), the frequency difference (~21.1 Hz) remains almost constant. From 60°C to 78°C, a ~0.3 Hz discrepancy can be detected, giving an average change in resonant frequency of 0.02 Hz/°C or about 0.1 ng/°C for a sensor with an active area of 0.535 cm$^2$. It is commonly observed that by monitoring differences in frequency shifts, most of the error from small temperature changes can be made small.

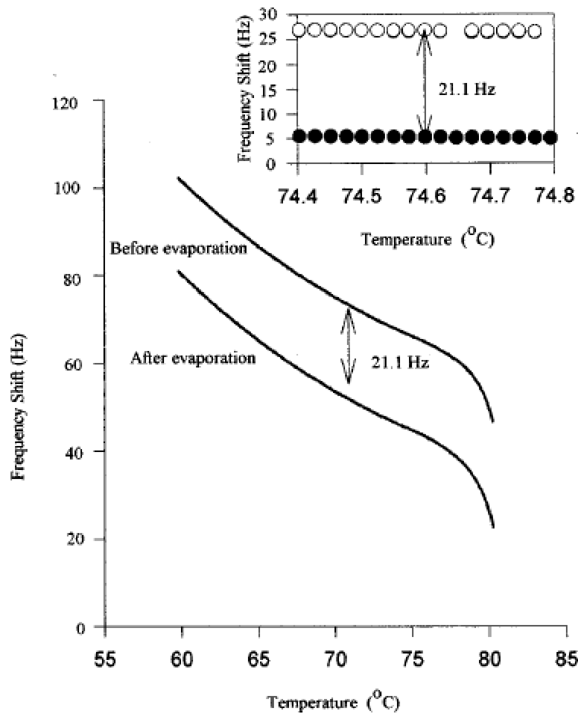


**Figure 3.10: Frequency shift of QCM with temperature before thin film application and after thin film application[55]. Inlay: zoom of a section of data.** ***Note that at all temperatures, the difference in frequency is approximately 21.1 Hz.***

In a typical total yield sputtering measurement, QCMs have a thin film of target material applied to the QCM surface and are then placed under an ion beam. As the thin film sputters away, the change in mass with time is recorded, providing a variant to the weight loss technique[56]. A sputtering yield can then be determined:

$$Y = \frac{\Delta m N_A q}{\Delta t J_B M_t} \quad \textbf{(3.11)}$$

In the experiments presented in this thesis, the QCM was used as an accumulation device. The QCM was moved above the target to measure changes in sputtered particle flux, thus providing differential sputtering yields.

## 3.3 *Differential Sputtering Yields*

While differential sputter yield values, $y(\alpha, \phi)$, can be estimated with Monte Carlo programs (popularly, TRIM.SP) and molecular dynamics programs, experimentally measured values provide the greatest insight. Differential yields are usually measured in one of two ways: 1) using collector plates (Figure 3.11) or shrouds around a sputtered target and 2) changing the relative angle of a sensor to the sputtered target. Both methods attempt to measure the number of sputtered particles at known locations relative to the sputtering source. The first method uses the plates to accumulate a condensed thin film of a sputtered material, whose thickness is later probed at various locations. The most common thickness probing methods are RBS[20,57,11] and Auger/XPS spectroscopy[58,59]. Other thickness probing methods include optical reflectance/opaqueness measurements and optical/physical profilometry.

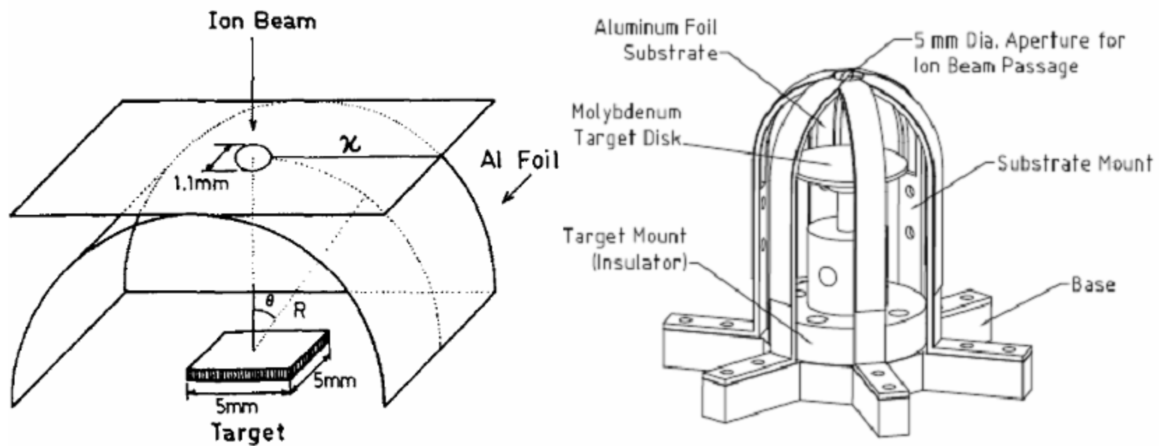


**Figure 3.11: Examples of shrouds used to collect sputtered particles, note the holes for ion beam passage.** ***Accumulated thin film will later be analyzed. Left, a cylindrical collector plate[60]; Right, a series of strips formed in a spherical pattern above the target[20].***

The second method adjusts the location of a sensor that can measure instantaneous yield. This can mean moving the sensor itself, the target, the ion source, or any combination to get measurements at

different locations. Examples of moved sensors used in these measurements are LIF detectors[39], Quadrapole Mass Spectrometers (Residual Gas Analyzers) [48], SIMS/SNMS detectors, and Quartz Crystal Microbalances[37,61]. The method used in the experiments presented in this thesis is changing the relative angle of a QCM sensor with respect to the target.

Obtaining the solid angle subtended by the finite spot being measured is an important step in differential sputter yield measurements. If the source area of the sputtered particle is assumed to be a small size then, the solid angle is given by:

$$\Omega = A_{sensor} / R^2 \tag{3.12}$$

where $R$ is the distance from the sputtered source area to the location of the sensor.

and the differential yield measurement becomes:

$$y(a,\phi) = \frac{N_{sp}(\alpha,\phi)}{N_{ion}\Omega} \tag{3.13}$$

where $N_{sp}$ is the number of sputtered particles measured by the sensor at a finite spot above the target, and $N_{ion}$ is the number of incident ions on the target. If measurements (or assumptions) are made over the entire "northern" hemisphere (where sputtered particles are ejected), the *total* yield can be arrived at by[62]:

$$Y(\alpha,\phi) = \int_0^{2\pi} \int_0^{\pi/2} y(\alpha,\phi)\sin(\alpha)\,d\alpha\,d\phi \tag{3.14}$$

(see Figure 2.8 or Figure 3.13 for definition of coordinate system)

Most often, differential yield measurements are made when the ions are at normal incidence. This situation provides differential yield distributions that are symmetric about the target normal if the target material is amorphous or polycrystalline (Figure 3.12). The use of this argument allows the entire distribution to be obtained by measuring only from α = 0° to 90° (0 to π/2).

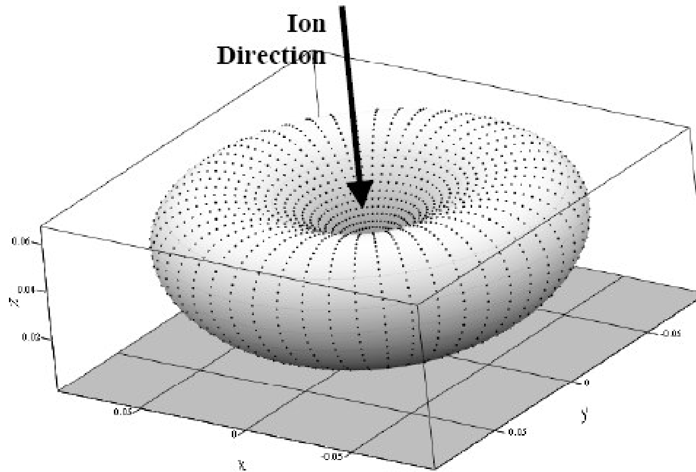


**Figure 3.12: Symmetry of differential sputter yields about the target normal for 350 eV $Xe^+$ on Mo at normal incidence[37].**

For oblique (non-normal) ion incidence at low energy, measurement locations are required above at least half of the "northern hemisphere" for amorphous or polycrystalline targets, and east-west symmetry arguments can be made to determine the differential yields for the other half hemisphere (Figure 3.13). Experiments presented in this thesis measure the differential yield only along this east-west symmetry plane, though an investigation into full hemispherical measurements is briefly described.

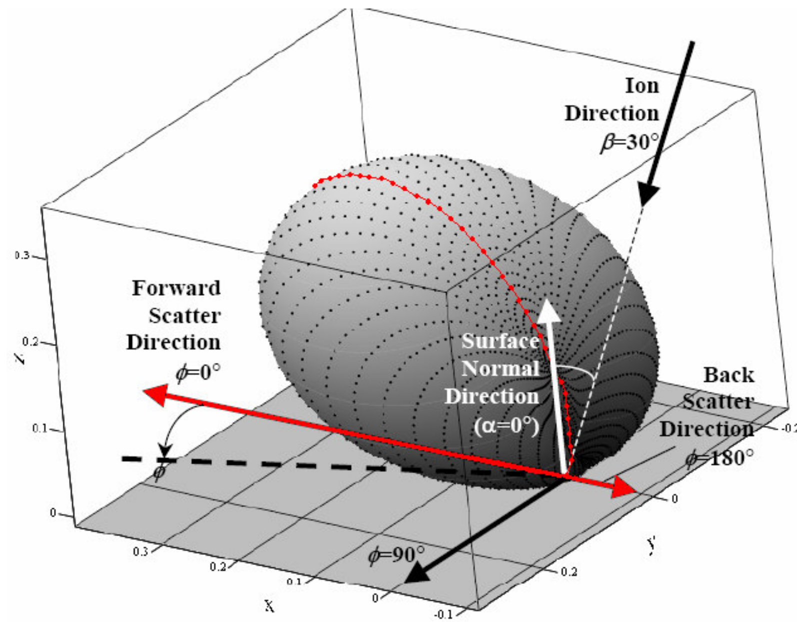


**Figure 3.13: Differential sputtering yield distribution for oblique angle ion incidence for 350 eV $Xe^+$ on Mo[37].** ***Note the symmetry about the $\phi = 0° = 180°$ plane (red).***

## 3.4 *Summary*

This chapter outlined some common methods used to obtain total sputtering yields. The use of the quartz crystal microbalance sensor as a detector was identified. Differential sputtering yield measurement considerations were also discussed.

# Chapter 4 Experimental Set-up and Measurements

Many measurements have been performed in the work described herein where the QCM was positioned along an arc that contained both the target normal vector and the ion beam vector. These tests are referred to as non-azimuthal experiments to differentiate them from a fewer number of tests that were performed when the QCM was positioned throughout the hemisphere above the target. A description of the non-azimuthal experimental setup is presented first. Next, descriptions of the vacuum chamber, ion source/target geometry, ion beam characteristics, QCM, measurement procedures, data acquisition, and data analysis are provided. A brief discussion of the validity of an infinitesimal beam spot on the target is also presented along with analysis results. Finally, a description is provided of the setup used to perform full-azimuthal measurements in the hemisphere above the target.

## 4.1 Vacuum Chamber

A 0.125 $m^3$ stainless steel vacuum chamber (43 cm ID x 76 cm long main section), equipped with a 1500 liter/s CTI-8 cryogenic pump, was used for all of the experiments described herein. With a base pressure of $5\times10^{-7}$ Torr (after 8-hour bake out), the pumping system maintained a working pressure of between $5\times10^{-5}$ Torr to $9\times10^{-5}$ Torr during all testing. The main background gas contaminate measured by a Ferran MPA residual gas analyzer (RGA) was $N_2$ (or CO) at a pressure of 2 x $10^{-7}$ Torr followed by $H_2O$ at $1.2\times10^{-7}$ Torr.

## 4.2 Ion Source and Target

The ion source shown in the electrical layout in Figure 4.1 was comprised of a discharge chamber, into which neutral gas was flowed at a set flow rate. The neutral gas was ionized using a tungsten hot-filament cathode, and the ion optics used to extract and focus the ion beam consisted of a two-grid Poco graphite system. A tungsten hot-filament neutralizer was located 1 cm downstream of the accelerator grid. The neutralizer emission current was set at 150% of the beam current to negate the space charge effect and neutralize the extracted ion beam. The anode voltage ($V_{anode}$) was set between 30 V and 35 V to minimize the number of multiply charged ions produced. Three different gases were used in the process of this investigation: xenon, krypton, and argon.

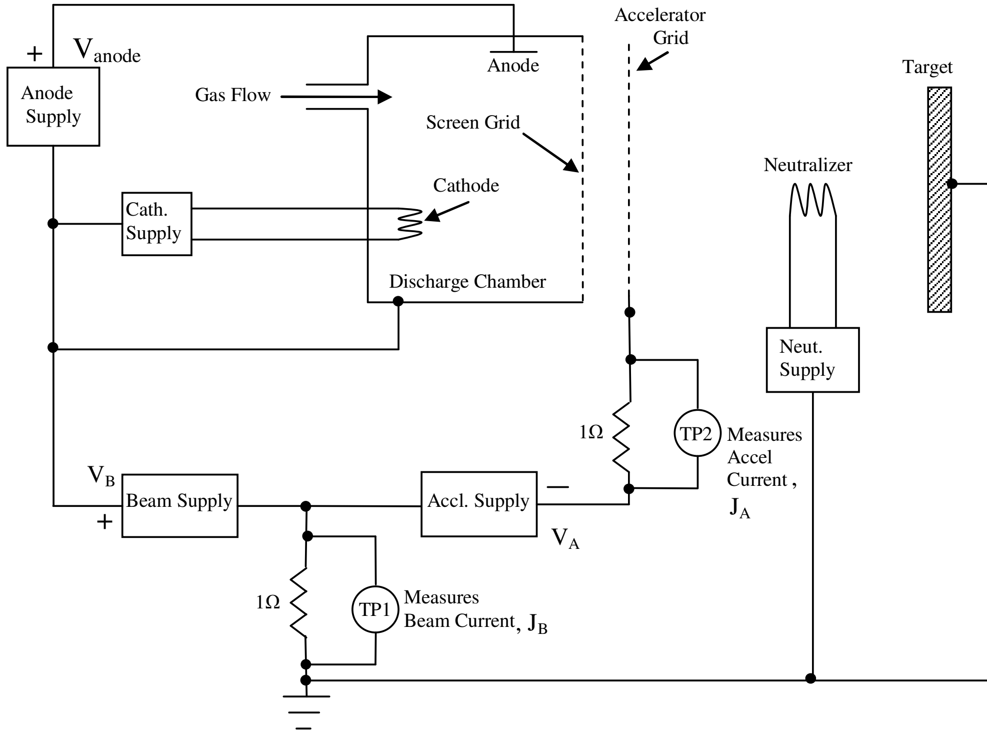


**Figure 4.1: Electrical diagram of the Kaufman type ion source system used in experiments.** ***TP1 and TP2 are test points where voltages across the 1 Ω resistors are measured (1 mV =1 mA).***

A rotatable, water-cooled target was placed 23 cm downstream of the ion source. Target materials investigated were molybdenum, tantalum, and tungsten; all of which were at least 99.9% pure. The ion beam extracted from the ion source was directed toward the target as indicated in Figure 4.2. For each

configuration, a QCM was used to obtain the differential sputter yield distribution by sweeping it over the target (about the axis of target rotation) so as to ensure the viewing of the same point on the target throughout the sweep. The QCM was placed, via an extended arm, 17.4 cm ($r_{qcm}$) from the target center. The polar angle of the QCM from the target normal is defined as $\alpha$, whereas the angle of the ion beam from the target normal is defined as $\beta$ (the angle of incidence). Sputtered particles with $\alpha > 0$ are referred to as forward-sputtered and, conversely, $\alpha < 0$ as back-sputtered.

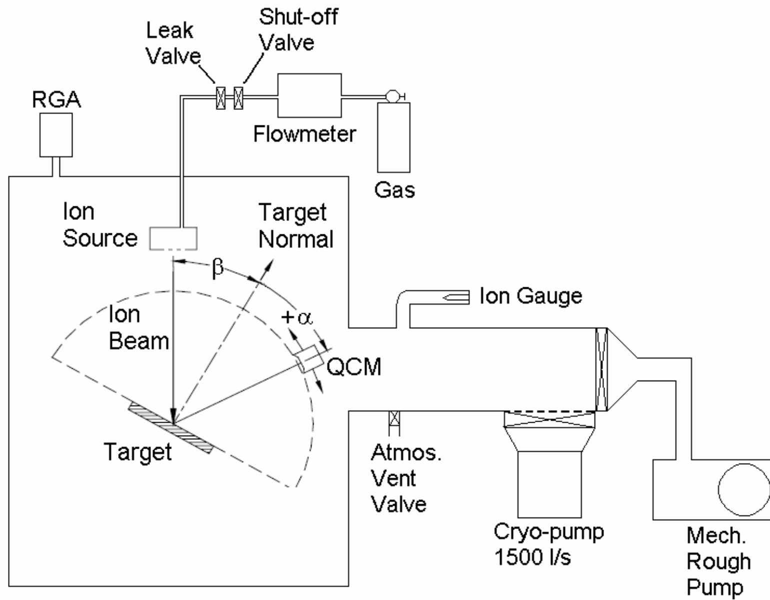


**Figure 4.2: Vacuum system and ion source set-up.**

Two assumptions are made with the QCM method: 1) the beam spot size on the target is small and 2) all the ions arrive at the same angle of incidence, $\beta$. These assumptions provided a straightforward way to calculate the differential yield at a given value of $\beta$. A screened Faraday probe was used to measure the current density variation of the ion beam at the target to investigate the validity of this beam spot assumption in our set-up.

For each beam energy investigated, a set of Faraday probe measurements were taken in the $\beta = 0°$ target plane in order to identify the operating conditions that resulted in a minimized ion beam diameter, or the "optimized condition". A 25,000-step per revolution stepper motor was mounted outside of vacuum and attached to a rotating push/pull rod. A stainless-steel arm, with the Faraday probe mounted near the end, was attached to the rod and the Faraday probe was pointed at the ion source. The Faraday probe's

radial position was adjusted so that its circular path passed through the centerline of the ion beam (+/- 0.5 cm) as shown in Figure 4.3. A fine nickel mesh of 75% transparency was placed over the orifice that serves as the entrance to the Faraday probe. The screen and Faraday probe body were biased at -35 V to repel plasma electrons from entering the probe through the orifice. The collector plate located inside the Faraday probe was biased at +20 V to inhibit secondary electron emission and repel low energy ions that might be present in the beam plasma.

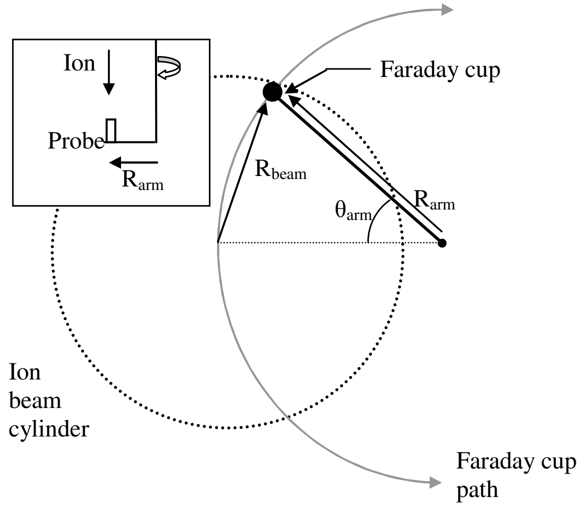


**Figure 4.3: Diagram of the Faraday cup path through the ion beam.** ***Main view is looking down the axis of the ion beam "cylinder". Inset is a side view of the main view.***

In order to characterize the beam, a measurement of current density vs. radial position ($R_{beam}$) is used (Figure 4.4). The raw data from a trace was obtained as current density vs. the angular position of the motor ($\theta_{arm}$). The geometry shown in Figure 4.3 is used to yield the following relationship:

$$R_{beam} = 2\sin(\theta_{arm}/2)R_{arm} \tag{4.1}$$

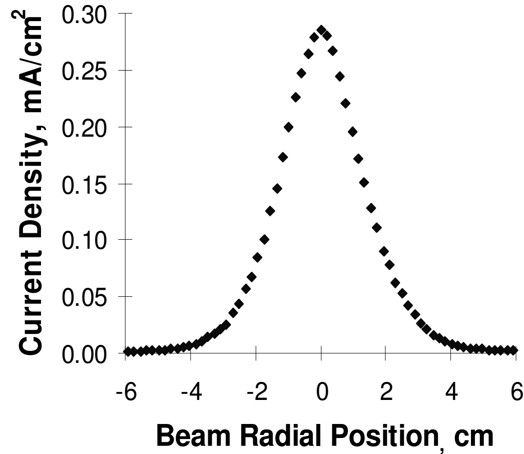


**Figure 4.4: Beam profile for 1000eV $Xe^+$.**

The radial center of the ion beam was defined to coincide with the location of the peak current density. The resulting profiles were fit with sixth order polynomial curve-fits which were subsequently integrated (and corrected for charge exchange losses) to obtain the total beam current flowing from the ion source. In general, the integrated beam currents ($J_{b,int}$) agreed with the indicated beam currents displayed by the power supply ($J_b$) to within ±15%. The analysis of the radial data showed optimized $Xe^+$ beams (see Table 4) whose full width-at-half-maximum (FWHM) value varied from 2.7 cm to 3 cm. For gases other than Xe, the beam current was adjusted to ensure perveances matched those in Table 4 with the assumption that a similar perveance level would result in a similar beam profile.

**Table 4**

| $V_b$, V | $V_a$, V | $J_b$, mA | $J_{b,int}$, mA | FWHM, cm | 90% radius, cm |
|---|---|---|---|---|---|
| 500 | -38 | 1.5 | 1.27 | 3.0 | 3.8 |
| 750 | -50 | 2.5 | 2.29 | 2.7 | 4.2 |
| 1000 | -50 | 4.0 | 3.80 | 2.7 | 3.5 |
| 1500 | -100 | 4.0 | 3.99 | 2.9 | 6.0 |

The radii within which 90% of the beam current was contained were large enough to put the small beam spot assumption into question. Also, the maximum divergence angle in the low current density (fringe) regions of the ion beam could be as much as 20°, which results in a spread in the actual ion incidence angle on the target. These issues are discussed in more detail in Section 4.6.

An ExB probe investigation was performed on a 5 mA, 1000 eV Xe ion beam (xenon having the lowest 2nd ionization potential of the three gases tested) utilizing a discharge voltage of 31 V. The results (Figure 4.5) indicated the doubles-to-singles current ratio was 3.9%, implying that for every 100 singly charged ions in the beam there were ~1.9 doubly charged ions. Note that the doubly charged ions possess twice the energy of their single-charged counterparts, and in the energy regime of interest herein have roughly twice higher sputter yields.

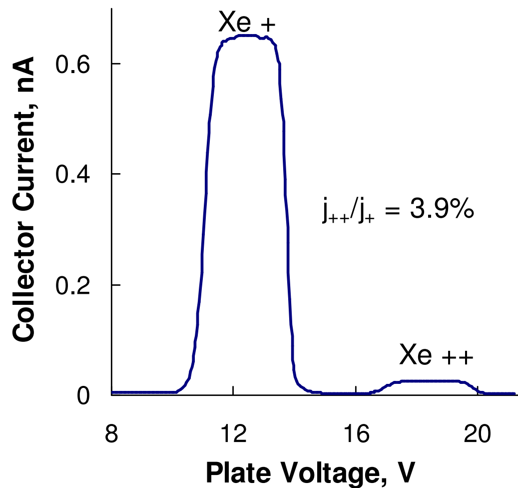


**Figure 4.5: E x B probe profile of a 5 mA, 1000 eV $Xe^+$ beam at a $V_d$ = 31 V.**

In the analysis, the presence of doubly charged ions is corrected for by counting each one as two singly charged ions. Owing to the relatively small number of doubly charged ions and their twice higher yields, such a treatment has a minimal effect on the resulting measured sputter yields. It is noted that for most materials this assumption begins to fail at ion energies below ~250 eV, due to the high sensitivity of sputter yield to energy in this regime.

## 4.3 Quartz Crystal Microbalance Sensor

A QCM was used to measure the differential sputtering distributions. The QCM works by detecting changes in mass on its surface (caused by deposited condensable sputter products) by sensing the change in the crystal's resonant frequency. Each crystal used in these experiments initially resonated at a frequency of ~6 MHz and had a surface coating of gold to ensure a high initial sticking coefficient. As

more mass accumulated on the exposed crystal area, $A_s = 0.535$ cm$^2$, the resonant frequency dropped until a resonant frequency of ~5.7 MHz was reached, at which point the crystal was considered un-useable and was replaced. To ensure consistent sticking coefficients for new crystals, a 10μg coating of target material was accumulated before initiating a test. The QCM acceptance angle is 165° and is able to receive a particle from any location on the target that is directed toward the QCM.

In general, there are two potential problems**Error! Bookmark not defined.**,[41] associated with using QCMs as sputtering measurement devices: 1) Measurement instabilities due to thermal changes in the environment and 2) Ensuring the QCM sensor face has a uniform flux of particles. The QCM is unaffected by the second problem in the tests described herein owing to the inherent set-up of the system, i.e. the QCM position is sufficiently far from the sputtering target to ensure that the arrival flux of sputtered material is spatially uniform. The first concern is minimized in two ways. The crystal holder was water-cooled at a temperature of ~28°C to accommodate the majority of the thermal stabilization of the system. This temperature value fluctuated approximately 0.1°C every 10 minutes and was considered to have a negligible effect on the mass readings.

Due to the movement of the QCM with respect to the ion source and its hot filaments, certain angular locations in the experiment had higher heat fluxes than others. As a result, when the angular position changed, transient heating of the QCM was observed to slightly affect the sputter readings. As indicated by Figure 3.10, a QCM will measure the same difference in resonant frequency ($f_f - f_i$) at any temperature, as long as $T_f = T_i$. Therefore, a 70 second long thermal stabilization period was implemented whenever the QCM angular position changed by 10° (to ensure $T_f = T_i$) and all data were based off of differences in resonant frequencies made at the same QCM position to ensure a consistent QCM reading at any steady state temperature.

## 4.4 Measurement Procedure

The polycrystalline targets used were much larger (15.24 cm × 15.24 cm) than the ion beam spot size to ensure that the vast majority of particles bombarded only the target. The targets were cleaned using an acetone solution but were not mechanically polished prior to being sputtered. The targets were attached

to a water cooled copper plate in order to keep the target at a relatively low temperature and minimize out-gassing. The target was leveled in the $\beta = 0°$ position with an angular accuracy of +/- 1°.

After target preparation, the chamber was evacuated and baked-out for an 8-hour period. Background gases were monitored with an RGA sensitive to species in the 1-100 amu range. In addition, the ion source was set to produce a 1500 eV beam and the target was sputter-cleaned for 1-3 hours. The QCM was held at a fixed $\alpha$ where a moderate amount of deposition would occur so that changes in the differential sputter yield could be monitored as shown in Figure 4.6. If this yield reached a stable value at the end of the sputter cleaning period, sputtering tests were commenced.

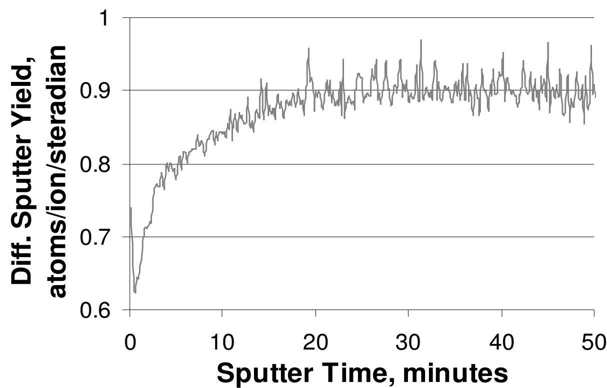


**Figure 4.6: Change in differential sputter yield as the Mo target is sputter cleaned.** ***Readings were stable after approximately 20 minutes.***

Typically, the QCM was placed at an angle $\alpha = 90°$ and a measurement was taken. The QCM's angular position was then decreased in 10° increments (excluding $\alpha = 0°$ due to beam blockage) until an angle of $\alpha = -90°$ was reached. A typical measurement involved waiting 70 seconds to allow for the thermal stabilization of the QCM followed by 7-10 differential yield measurements; these were averaged to obtain the final reading. If the standard deviation from the averaged value was greater than 5%, the measurement was repeated. A typical differential yield distribution is shown in the top of Figure 4.7 for an angle of incidence of 15°, for 500 eV xenon ions on molybdenum. The differential yield measurements were repeated in this way to obtain differential sputter distributions for $\beta = 0°$, 15°, 30°, 45° and 60° for each beam energy of interest (300-1500 eV for Ta, 500-1500 eV for Mo and W), bombarding ion (xenon, argon, and krypton), and target material (molybdenum, tantalum, and tungsten) combination for a total of

185 distributions. Normal incidence sputter yields for Tantalum were extended from the normal 500-1500 eV range to include 150 eV, 200 eV, and 400 eV. If an atmospheric vent was required (to change the target material, replace the QCM crystal, etc.), the bake-out/target cleaning procedure was implemented before differential sputter yield measurements continued.

## 4.5 Data Acquisition and Analysis

When the QCM was placed in a polar angular position, $\alpha$, for a given time, $t$, the number of sputtered target atoms deposited onto the crystal increases to a value that is proportional to the differential yield. The change in the crystal's frequency is interpreted as a mass reading (in units of μg) by a deposition monitor device. When a differential sputter yield measurement was initiated, the initial QCM mass and initial time were recorded by a LabView program. A delay of several seconds to tens of seconds allowed more target atoms to be deposited on the QCM surface. In this delay period, beam current measurements (from the power supply) are taken every 0.5 seconds. At the end of the delay, the final QCM masses and times were recorded in the program to compute the mass accumulation rate, $R(\alpha)$, in gm/s. The beam current measurements were averaged to provide $J_{B,avg}$ (C/s). Using the molecular weight of the target atoms ($M_t$ in g/mol), the distance from the target center to the QCM ($r_{qcm}$ = 17.4 cm), the QCM sensor area ($A_s$ = 0.535 cm$^2$), the electronic charge ($q$ = $1.6\times10^{-19}$ C/ion), and Avogadro's number ($N_A$ = $6.023\times10^{23}$ atoms/mol), a differential yield value can be extracted as shown in Eq. (4.2)[62]:

$$y(\alpha) = \left[R(\alpha) N_A q r_{qcm}^{\ 2}\right] / \left[M_t J_{B,avg} A_s\right] \tag{4.2}$$

where the term $A_s / (r_{qcm}^{\ 2})$ provides the solid angle (in steradians) that the QCM sensor subtends, thus giving $y(\alpha)$ units of atoms/ion/steradian (assuming the beam spot size is small).

In order to compare our results to total yield results available in literature, it was necessary to integrate the differential yield results over the hemisphere above the target. As mentioned previously, the differential yield profile was only measured in a single arc above the target for most tests. (Differential sputter yield measurements as a function of both polar and azimuthal angles are discussed in Section 4.7). The arc of $y(\alpha)$ data from $0° < \alpha < 90°$ is defined to correspond to an azimuthal angle ($\phi$) of 0° that represents forward sputtered material and $y(\alpha)$ data from $-90° < \alpha < 0°$ is defined to correspond to an

azimuthal angle of $\phi$ = 180° that represents back sputtered material. With this method, no additional information is available at other azimuthal angles. Consequently, an assumption was made that the forward sputtered distributions are uniform over the range of $\phi$ from -90° < $\phi$ <90°, and back sputtered distributions are uniform over the range of $\phi$ from 90°< $\phi$ <270° (see Figure 4.7).

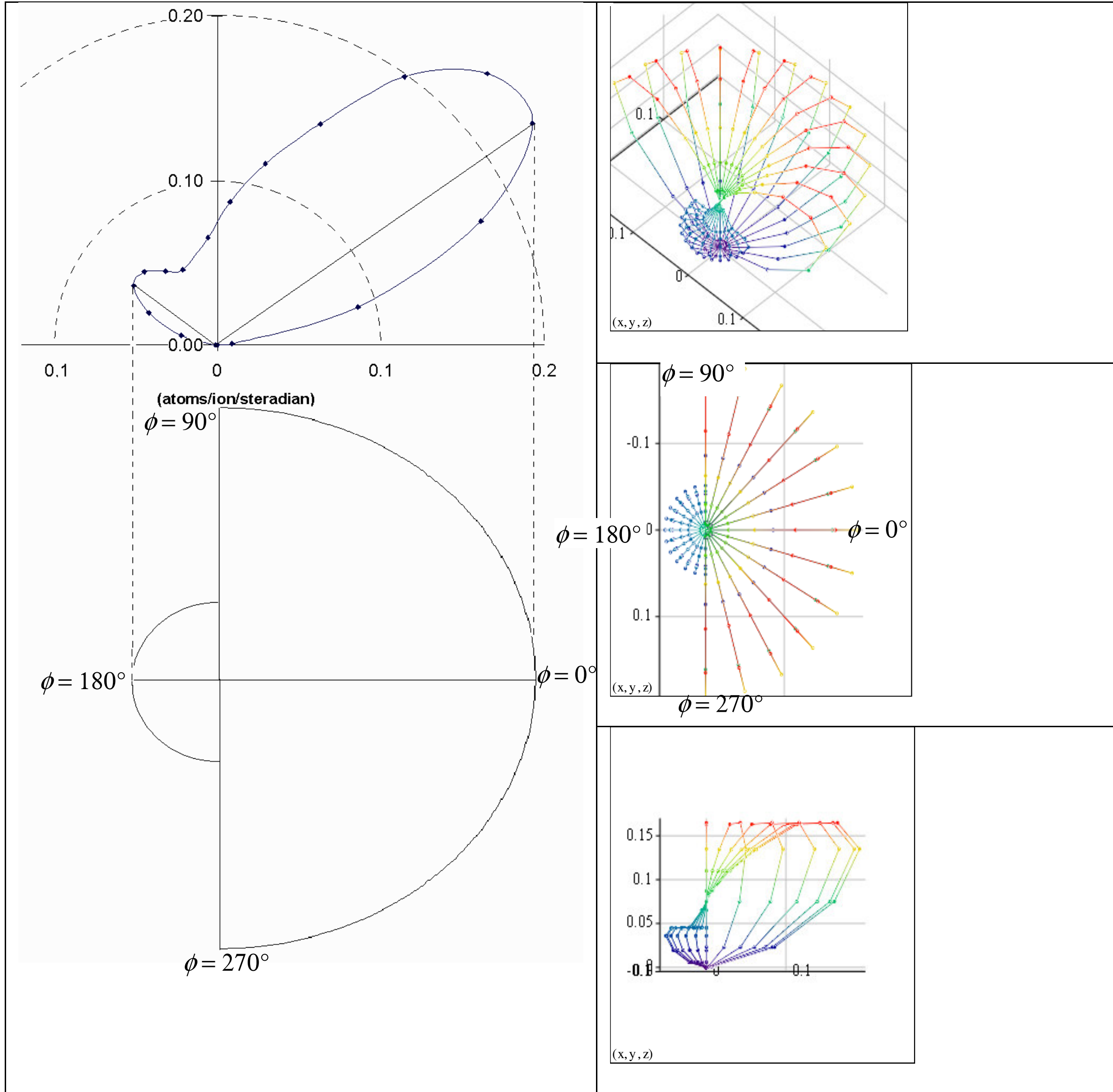


**Figure 4.7: Azimuthal distribution assumption. Left** ***is a polar plot of the distribution with a projection of the distribution into azimuthal components*****.** ***Right is an isometric view, top view, and side view of a 3D plot of assumption.***

This physically unrealistic symmetry assumption allows the integration of the differential sputter yield distributions to obtain the total sputter yield as shown in Eq. (4.3). This assumption is equivalent to assuming a linear variation from the back sputtered distribution to the forward sputter distribution.

$$Y = \int_0^{2\pi} \left( \int_0^{\pi/2} \sin(\alpha)\, y(\alpha,\phi) d\alpha \right) d\phi \tag{4.3}$$

The differential yield data were first fit using two sixth-order polynomial curve-fittings according to Eqs. (4.4) and (4.5) after *y(α)* was plotted versus cos(*α*)[62,63]. One curve-fit was applied to the differential yields in the forward sputtered direction (*A* coefficients), and the other was fit to the back sputtered direction (*B* coefficients). It is noted that results are presented and discussed in Chapter 5. The *A* and *B* coefficients obtained from the measurements are included in Appendix A. Using the azimuthal distribution assumption described, Eq. (4.3) is reduced to Eq. (4.6). While the aforementioned assumption on the azimuthal behavior is not physically correct for non-normal incidence, it provides a practical means of determining total sputter yields, and gives values that agree reasonably well with published yields.

$$y(0 \le \alpha \le 90) = A_6 \cos^6(\alpha) + A_5 \cos^5(\alpha) + \ldots + A_1 \cos(\alpha) \tag{4.4}$$

$$y(-90 \le \alpha \le 0) = B_6 \cos^6(\alpha) + B_5 \cos^5(\alpha) + \ldots + B_1 \cos(\alpha) \tag{4.5}$$

$$Y = \sum_{i=1}^{6} \frac{\pi}{i+1} A_i + \sum_{i=1}^{6} \frac{\pi}{i+1} B_i \tag{4.6}$$

## 4.6 Infinitesimal Beam Spot Assumption Analysis

As Figure 4.4 and Table 4 indicate, the ion beam spot size on the target has a finite value. In the data analysis, the differential yield was calculated assuming a point source for the emission of the sputtered atoms. A numerical investigation into the effect of the non-infinitesimal beam on the differential yield is described in this section. The analysis was performed in several steps: 1) the beam spot on the target was “meshed” with computational node locations, 2) variables necessary to compute the differential yield of each node were assigned, and 3) differential yield at inputted $\alpha$, $\beta$, and $\phi$ were computed based on the

cumulative total from each node. The algorithm still used the same azimuthal distribution assumption shown in Figure 4.7.

The first main step is to produce the computational mesh of the beam spot on the target. At normal incidence, this mesh is simply a circle, while increasingly oblique incidences produce increasingly eccentric elliptical meshes regions (Figure 4.8). The node to node spacing is variable so that the computation time and precision can be balanced.

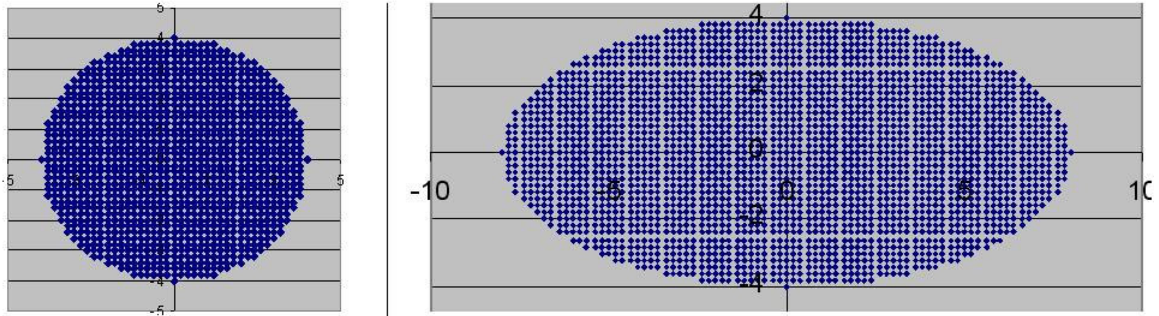


**Figure 4.8: Computational meshes for a beam radius of 4 cm for $\beta = 0°$ (left) and $\beta = 60°$ (right).**

Each node is assigned a cell identification number, global coordinates ($X,Y,Z$) and target coordinates ($x,y,z$). Figure 4.8 is shown as meshed in target coordinates. Inspection of the two coordinate systems (Figure 4.9) shows that both $Y$ (global) and $y$ (local) will have the same value, and that the nodes in the target coordinates have zero altitude ($z = 0$ for all nodes). From these values, each node is also assigned an $(r, \phi)$ coordinate is assigned to each node.

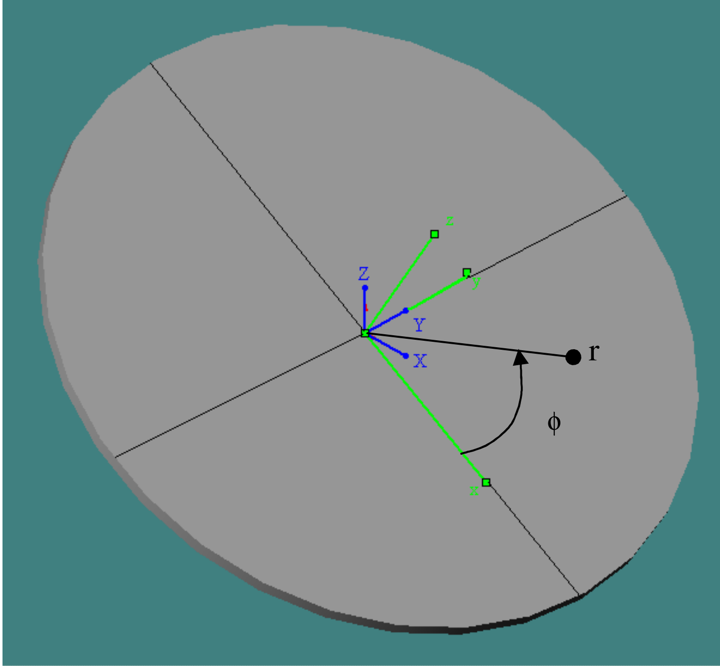


**Figure 4.9: Global (blue, upper case) and local (green, lower case) coordinate definition for target mesh.** ***Z is ion beam axis; z is target normal; x is gradient of target rotation; Y and y are collinear with target's axis of rotation. Coordinates r and $\phi$ are defined.***

The next step was to assign variables necessary to calculate the differential yield from each node. The inputs that are needed include the $A_1$-$A_6$ and $B_1$-$B_6$ coefficients of Eqs. 4.4 and 4.5 (for $\beta$ = 0°, 15°, 30°, 45°, and 60°), the coefficients of the curve fit to the Faraday probe data, and the polar coordinate position of a "simulated" QCM sensor. The use of the Faraday probe data allows the assignment of the number of arrival particles to the area surrounding each node and the calculation of a particle's actual angle of incidence at each node (measured beam divergence). Using the coefficients from Eqs 4.4 and 4.5, the calculated actual particle incidence, and the vector from each node to the simulated QCM location, a differential yield value is assigned to each node. The strength of this yield is scaled using the relative number of arrival particles. The summation of these scaled yields over all of the nodes gives the differential yield that the QCM would read at the simulated position *not* assuming an infinitesimal beam spot.

The last step was to repeat each simulated QCM position for all desired position (polar angles and azimuthal angles). A differential yield distribution can then be obtained and compared to experimental measurements. These simulated yields are based on the actual yield data (calculated assuming an

infinitesimal beam spot), hence if a comparison is made between the simulated distribution and the measured distribution and are similar, then the infinitesimal beam spot assumption is valid. If dissimilar, the shapes of the inputted measured distributions need to be changed until both the measured and simulated distributions are satisfactorily similar, at which point the inputted distribution may be assumed to be the correct distribution.

Results of a simulation are shown in Figure 4.10 along with experimental data for the worst case scenario of a 1500 eV beam, and acceptable agreement is observed. Most simulated non-infinitesimal beam spot differential yield measurements were found to be in acceptable agreement with the experiment measurements. There seemed to be two polar angle regions ($\alpha$ = 0° and 45°) where there was a difference of approximately 5-7%, according to the simulation. The simulated differential sputter distribution values were typically less than the measured distribution values. Because the simulation very closely matched the measured direction, data was not corrected. However, it is noted that the simulation attempts to predict a distribution by inputting a distribution that is already known, and therefore the results may appear more favorable than what is actually occurring.

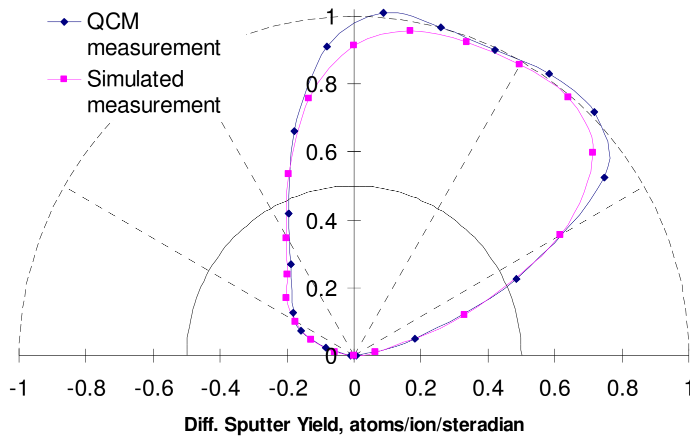


**Figure 4.10: Actual QCM measurement vs. a simulated measurement for 1500 eV $Xe^+$ on Mo at $\beta$ = 45°.** *The simulation accounts for a large beam spot size and differing angles of incidence due to beam divergence.*

## 4.7 Azimuthal Measurement Description

The assumed azimuthal sputtering distribution shown in Figure 4.7 was noted as not being physically realistic. An experimental investigation was devised to obtain sputter yield data at multiple azimuthal angles. The design of the QCM hardware constrained its swept path to lie on a single arc for a given azimuthal angle. Hence, it was necessary to design a fixture to rotate the target to obtain multiple azimuthal measurements.

The fixture, shown in Figure 4.11 and Figure 4.12, consists of a base plate, a shaft with a 25000-step stepper motor attached to control the azimuthal angle and the target height, and a target mount allowing tilt to change the angle of incidence. The base plate and target were made of molybdenum, while the arm and mount were made of stainless-steel. The target was sufficiently large to prevent any of the components beneath it from exposure to the ion beam.

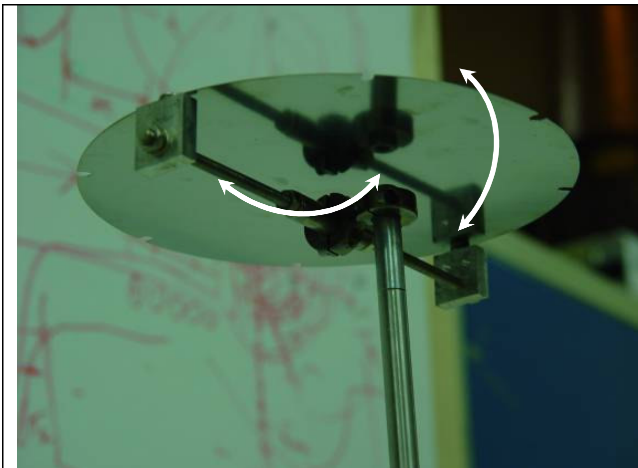

**Figure 4.11: Target fixture showing target, mount and top portion of the arm.**

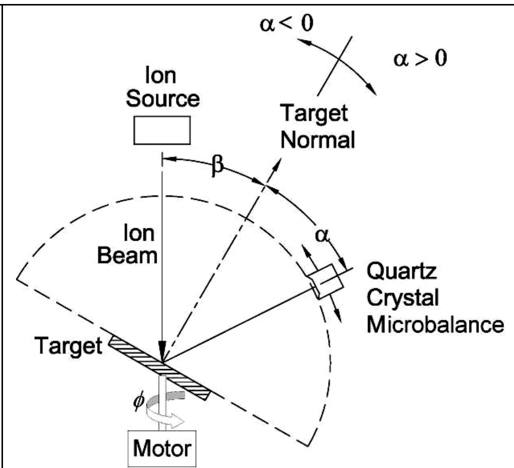


**Figure 4.12: Diagram of target fixture and QCM in vacuum chamber.**

Before each measurement set, the target was aligned to ensure correct height, angle of incidence, and azimuthal angle zero position of the motor. Once aligned, the chamber was evacuated, baked out, and the target was sputter cleaned for 3 hours at a beam energy of 1500 eV to remove any surface contaminants on the target. Measurements proceeded as described above, excepting that instead of changing the incidence angle, $\beta$, the target was rotated by 15° azimuthally until all azimuthal measurements had been

taken (see Figure 4.13). The chamber was then vented to atmosphere and the angle of incidence was changed and the target realigned.

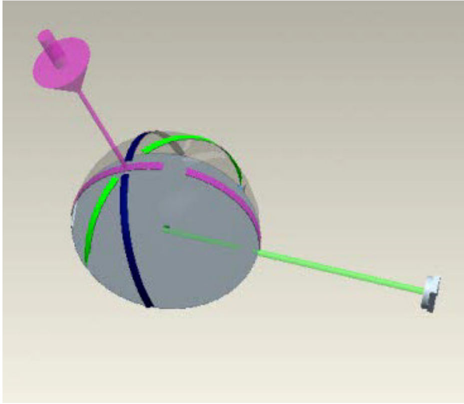

**Figure 4.13: Azimuthal measurement paths (not shown are rotations of 15°,60°,75°).** *Ion beam is represented by pink arrow, QCM view by green rod, and the path of the QCM by the "ribbons". Note that in only the pink ribbon case do the values of $\phi$ stay constant.*

All data is collected using a *global* α, $\phi$ (defined as the A and Φ) coordinate system, which has $\alpha_{global}$= A = 0° direction aligned with the center of the ion beam. The $\phi_{global}$ = Φ = 0° direction is defined by the plane above the target containing the ion beam center and the target normal. A more convenient *local* coordinate system (polar angle is α, azimuthal angle is $\phi$) to present data in is the coordinate system with α = 0° aligned with the target normal. The $\phi$= 0° is still defined by the plane containing the ion beam center and the target normal. The A, Φ coordinates can be converted to α, $\phi$ coordinates by converting the A, Φ coordinates into XYZ coordinates associated with the global spherical coordinate system. The XYZ coordinates are next converted (using Eq. Set 1) to xyz coordinates associated with the local spherical coordinate system (but with y = Y). X,Z are converted to x,z using a standard rotation transform defined by Eq. Set 2 where β is the angle of incidence. The xyz coordinates are then converted to α, $\phi$ coordinates using Eq. Set 3.

$$X = \sin A \cos \Phi$$
$$Y = \sin A \sin \Phi$$
$$Z = \cos A$$

Equation Set 1

$$\begin{bmatrix} x \\ z \end{bmatrix} = \begin{bmatrix} \cos\beta & \sin\beta \\ -\sin\beta & \cos\beta \end{bmatrix} \begin{bmatrix} X \\ Z \end{bmatrix}$$

Equation Set 2

$$\alpha = \arccos(z)$$
$$\phi = \arcsin\left( \frac{y}{\sqrt{x^2 + y^2}} \right)$$

Equation Set 3

Results from these experiments are discussed in Chapter 5.

## 4.8 Summary

A description of the equipment and the experimental procedure used to obtain the differential yield profiles was provided. The results from the experiments are discussed in Chapter 5.

# Chapter 5 Results & Discussion

This chapter will investigate trends observed seen in the data collected with the experimental apparatus described in Chapter 4. All data are summarized in tabular form in Appendices A, B, and C.

## 5.1 Normal Incidence

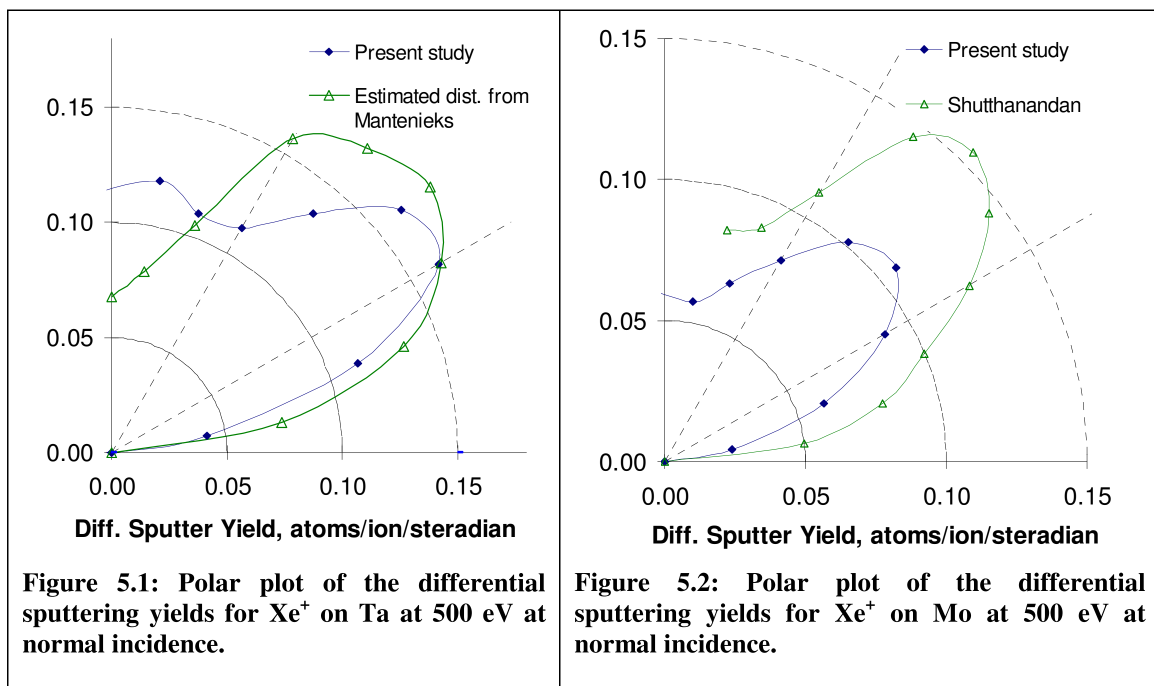


**Figure 5.1: Polar plot of the differential sputtering yields for $Xe^+$ on Ta at 500 eV at normal incidence.**

**Figure 5.2: Polar plot of the differential sputtering yields for $Xe^+$ on Mo at 500 eV at normal incidence.**

At normal incidence, the forward and backward distributions were found to be very similar, which supports the symmetry assumption for normal incidence and provides a rough check on the data. Figure 5.1 and Figure 5.2 compare the QCM-based sputtering distributions to other groups[57,64] who used RBS

measurement techniques performed on semi-circular foil collector strips that are exposed to materials sputtered from a target located below the foil. The distributions shown have a distinctive under-cosine shape typical of the low energy xenon sputtering regime of most materials. This study's *y(α)* distributions measured in the forward direction were very similar to those recorded by Shutthanandan[64] (Figure 5.2), however, this study's magnitudes were about 30% lower. Due to the lower *total* yield measurements (discussed below) for molybdenum at normal incidence, it is likely that Shutthanandan's measurements have more accurate distribution magnitudes. When compared to a distribution measured by Mantenieks[57] (Figure 5.1), this study's magnitudes were similar although the distribution shape was quite different from $\alpha = 0°$ to 40°.

Figure 5.3 through Figure 5.8 compare some of this study's integrated (normal incidence) total sputter yields with data from other groups[57,64,33,65,66, 67]. This study's total yields were lower than most other experimentally obtained sputter yields, although good agreement to Yamamura and Tawara curve fits[33] [Eqn. 2.10] was observed in general.

The distributions about the $\alpha = 0°$ axis were expected and observed (within a few percent) to be symmetric in most of the normal incidence cases. In the distributions where symmetry was not observed, a slight deviation from target level was detected after the test, thereby indicating high sensitivity of distribution shapes to the angle of incidence near $\beta = 0°$.

For each distribution, as the energy of the bombarding ion is increased, the distribution at normal incidence becomes less under-cosine and more cosine or over-cosine[62,63]. For all $Z$ ratios ($Z_{ion}/Z_{target}$) investigated in this study, the distributions at 1000 eV for normal incidence had either cosine or over-cosine distributions. For all $Z$ ratios greater than 0.5, the distributions at 500 eV had clear under-cosine shapes at normal incidence. This implied that the collision cascades at these conditions did not produce many sputtered atoms with energies greater than the surface binding energy that were ejected in the direction normal to the target. For $Ar^+$ on Ta and W ($Z$ ratio ~0.24) at 500 eV, the distributions were found to be nearly cosine.

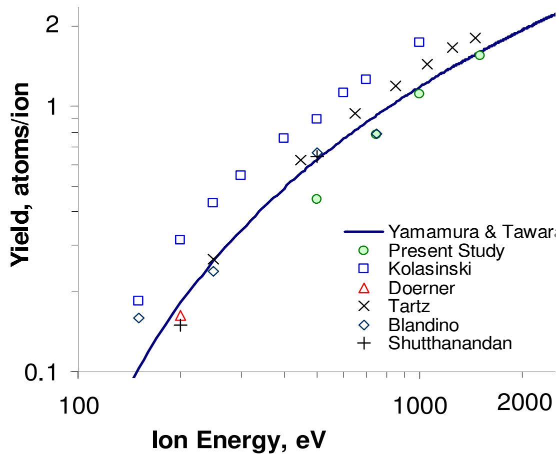

Figure 5.3: Total yields for $Xe^+$ on Mo.

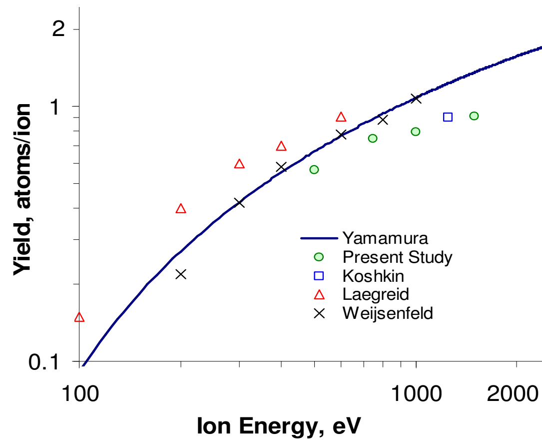

Figure 5.4:Total yields for $Ar^+$ on Mo

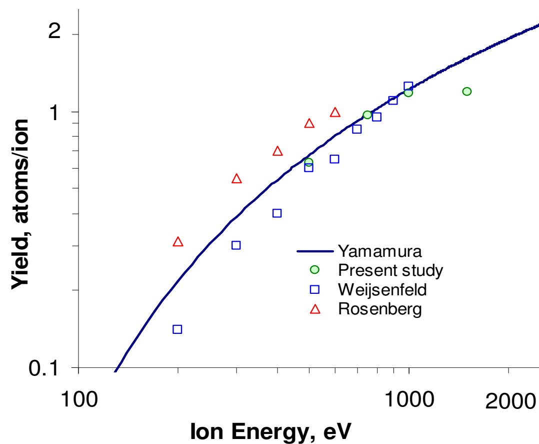

Figure 5.5: Total yields for $Kr^+$ on Mo.

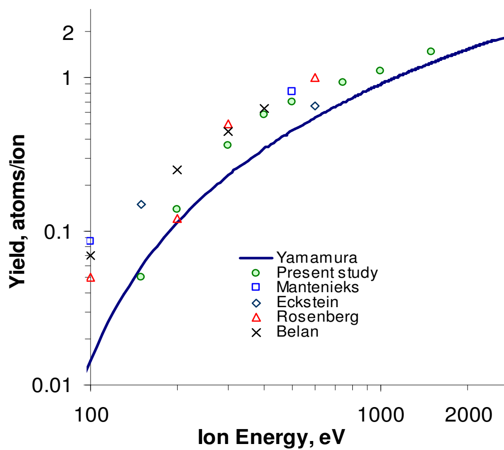

Figure 5.6: Total yields for $Xe^+$ on Ta.

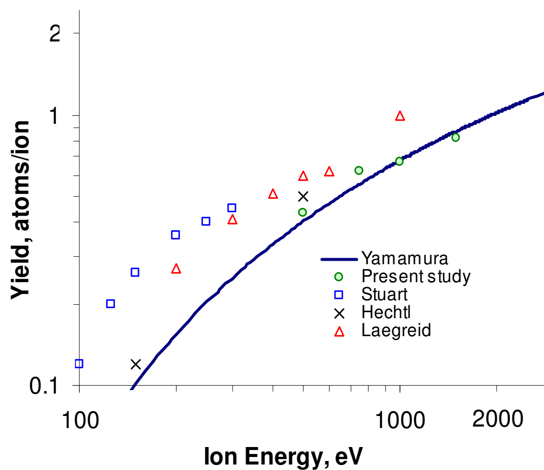

Figure 5.7: Total yields for $Ar^+$ on Ta.

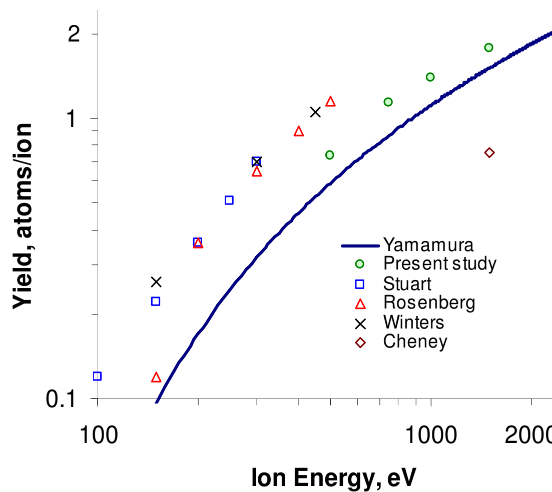

Figure 5.8: Total yields for Xe+ on W.

## 5.2 Non-normal Incidence

Figure 5.9 and Figure 5.10 compare total yield data calculated from differential yield measurements to those measured by various groups[56,68] for oblique incidence conditions. Again, this study's total sputtering yields are shown to be lower than those of other groups. However, the initial rates of rise of each group's results in both figures are almost identical. Tartz shows a maximum yield occurring at an angle of incidence of 60°-70° in Figure 5.9, while both Kolasinski's and this study's results have maxima in the 50°- 60° range.

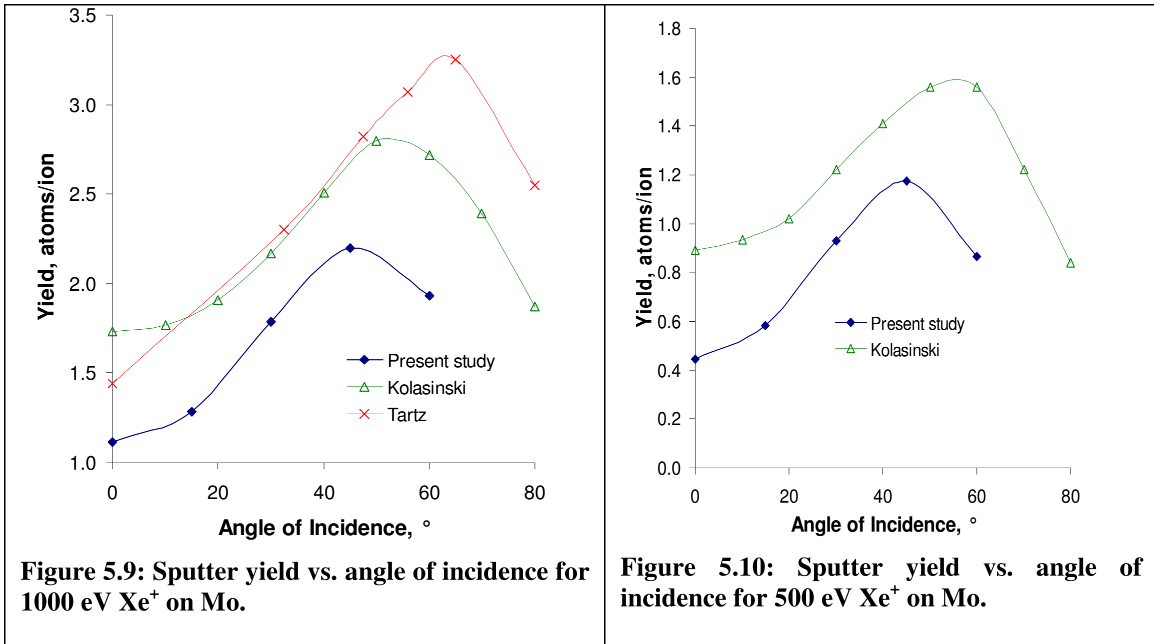


**Figure 5.9: Sputter yield vs. angle of incidence for 1000 eV $Xe^+$ on Mo.**

**Figure 5.10: Sputter yield vs. angle of incidence for 500 eV $Xe^+$ on Mo.**

Two models were used to curve fit (using the least squares method) the total sputtering yields at varying ion incidences. The first model was that of Sigmund (Eqn. 2.15). As can be seen in Figure 5.11 (Left), the Sigmund model diverges from the measured data after $\beta$ = 45°, therefore the curve fitting parameter, $f$, was only fit to data points with $\beta \leq 45°$. For 500 eV $Xe^+$ on Mo, an $f$ value of 3.22 was obtained (Sigmund suggested 1.667). Figure 5.11 (Right), shows that as ion energy is increased, the $f$ parameter approaches Sigmund's suggested value, although it cannot be generalized as so without taking more high energy data points.

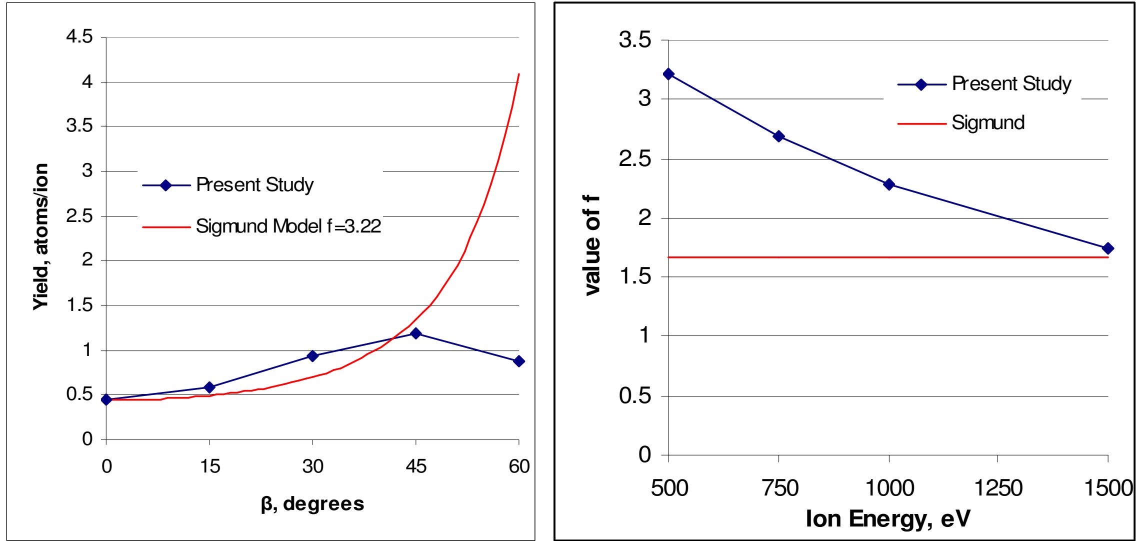


**Figure 5.11: Left; Comparison of 500 eV $Xe^+$ on Mo data to Sigmund's model (f = 3.22, Eqn. 2.15). Right; The fitted values of f as a function of energy for $Xe^+$ on Mo.** *Sigmund suggests f = 1.667.*

The second model used was Yamamura's (Eqn. 2.16). Figure 5. (Left) shows that the Yamamura fit correlated very well to the measured data. Yamamura's fit uses two fit parameters ($f_y$, $B$, based on $E_{th}$), that are related to $\beta_{opt}$ as related in Eqn. 2.17. The $\beta_{opt}$ (based on the curve fits) for all energies measured for $Xe^+$ on Mo were 50°. Figure 5. (Right) shows the values of the fit parameters at different ion energies. Both curves have nearly identical lineshapes that decrease steadily with increasing ion energy.

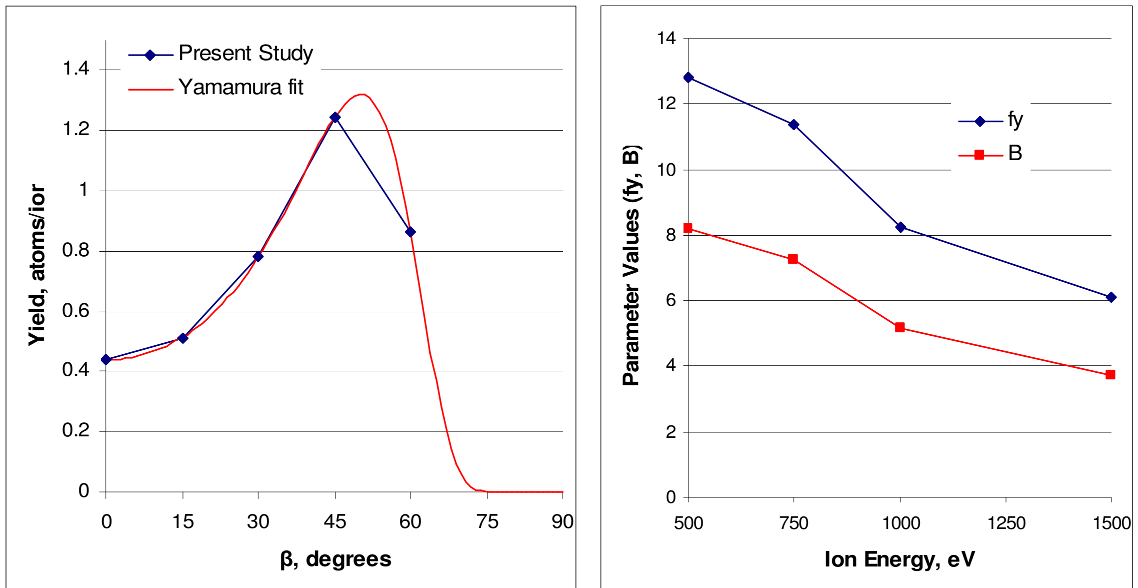


**Figure 5.12: Left; Comparison of 500 eV $Xe^+$ on Mo data to Yamamura's model ($f_y$ = 12.8, B = 8.2, $\beta_{opt}$= 50°; Eqn. 2.16). Right; The fitted values of $f_y$ and B as a function of energy for $Xe^+$ on Mo.**

For the distributions where the *Z* ratio was greater than 0.5 (i.e., for $Xe^+$ on Mo, Ta, and W and $Kr^+$ on Mo), 500 and 750 eV ions caused more material to be forward sputtered as the angle of incidence was increased from 15° to 45° (see Figure 5.13 for 500 eV data). At a higher incidence angle of 60°, less forward sputtering and more back sputtering was observed, which gave the distributions a more rounded shape. When the *Z* ratio was less than 0.5 (see Figure 5.14) at ion energies of 500 and 750 eV, a similar trend was observed, but the distributions were noticeably broader. At higher energies (1000 eV and 1500 eV), more broadening of the distributions was observed along with a definite shift toward over-cosine behavior at all incidence angles when $Z < 0.5$ (e.g., see Figure 5.15 and Figure 5.16 for 1500 eV data). This same behavior was seen with $Ar^+$ on W at all angles of incidence. In general, as the beam energy was increased, distributions at all angles of incidence approached a cosine or over-cosine distribution.

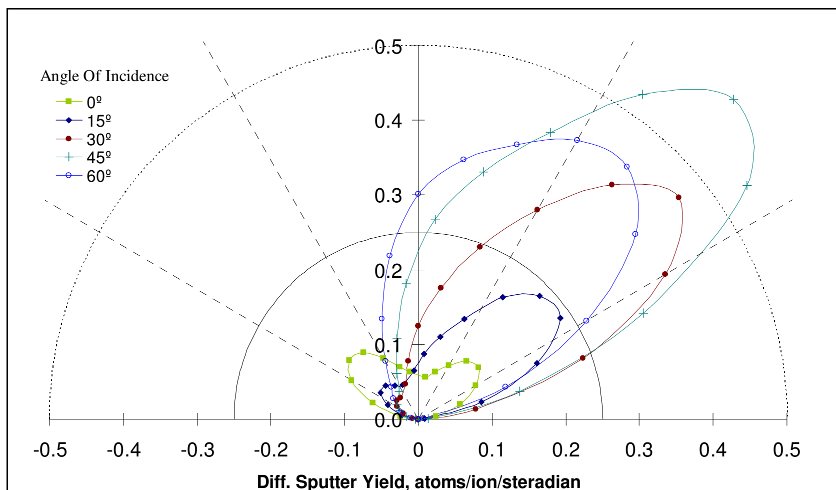


**Figure 5.13: Differential yield distributions at varying angles of incidence for 500 eV $Xe^+$ on Mo.** ***Typical of Z ratio > 0.5 results at low energy***

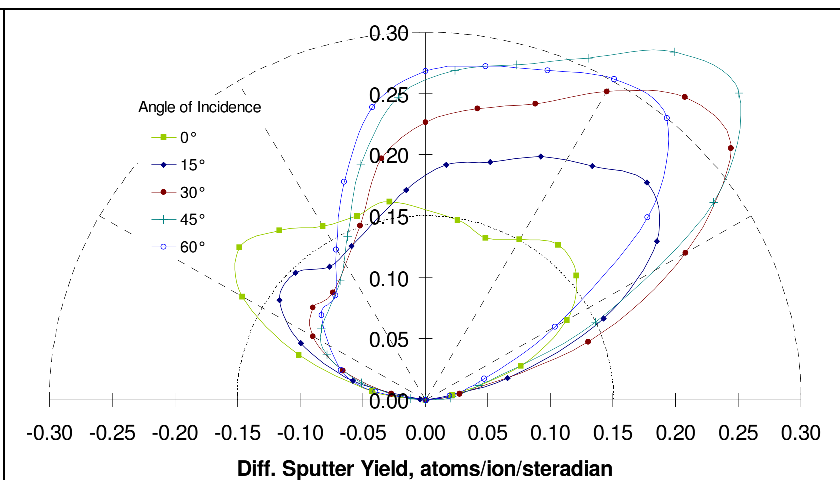


**Figure 5.14: Differential yield distributions at varying angles of incidence for 500 eV $Kr^+$ on W.** ***Typical of Z ratio < 0.5 results at low energy.***

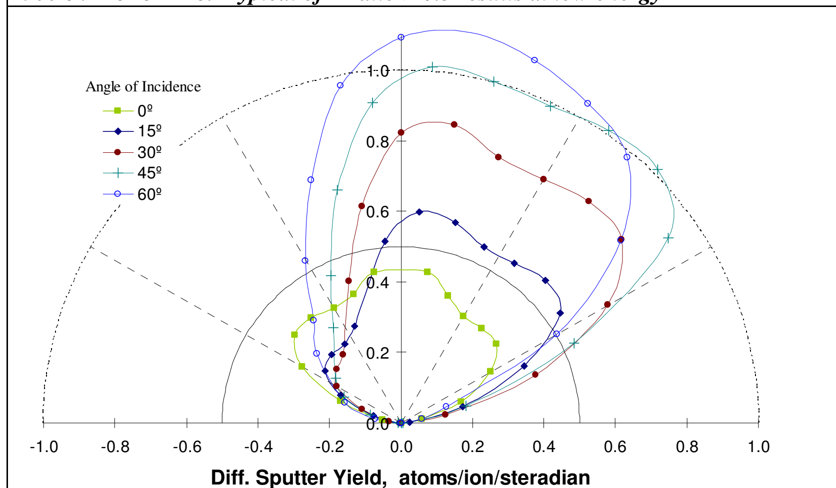


**Figure 5.15: Differential yield distributions at varying angles of incidence for 1500 eV $Xe^+$ on Mo.** ***Typical of Z ratio > 0.5 results at high energy***

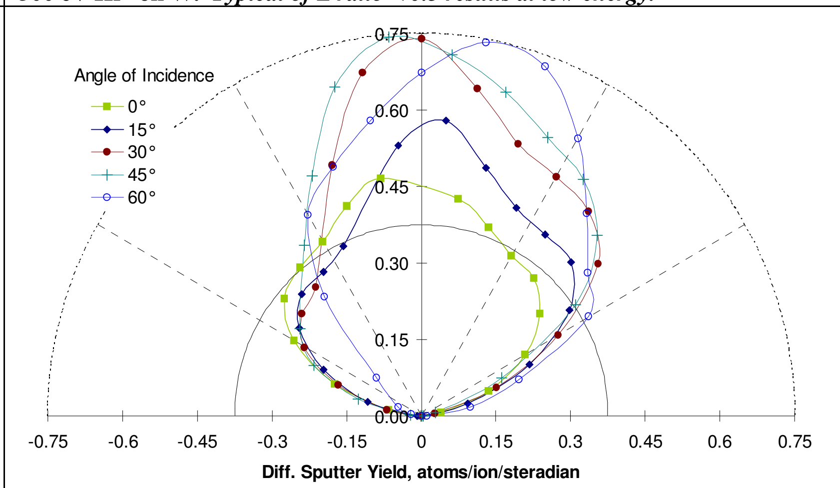


**Figure 5.16: Differential yield distributions at varying angles of incidence for 1500 eV $Kr^+$ on W.** ***Typical of Z ratio < 0.5 results at high energy***

The differential yield measurements for $Xe^+$ on Mo, $Xe^+$ on W, $Kr^+$ on Mo, $Ar^+$ on W, and $Kr^+$ on W (see Appendix B) had modified Zhang curve fits[69] (only in the $\phi = 0°$ direction) applied to them (using the least squares method):

$$y_{MZ}(E,\beta,\alpha,\phi) = \frac{Y^*}{1-\sqrt{\frac{E^*}{E}}\cos\beta} \cdot \frac{\cos\alpha}{\pi} \times \left[1-\frac{1}{4}\sqrt{\frac{E^*}{E}}\left(\cos\beta \cdot G(\alpha)+\frac{3}{2}\pi\sin\beta\sin\alpha\cos\phi\right)\right] \quad \textbf{(5.1)}$$

The $Y^*$ value is the total yield and is used as a scaling factor. $E^*$ is related to $E_{th}$ (a constant for the target material), but is used as a free line shape parameter here.

Results of the curve fits for $Xe^+$ on Mo are shown in Figure 5.17 to Figure 5.21. The $Y^*$ yield based off of the fits were within 15% of the $Y$ yield values based off of experimental data and the azimuthal assumption outlined in Chapter 4. In general, the Zhang fits correlated with the experimental data very well. The fits were able to accommodate a majority of the line-shape features seen in the experimental data. A noted exception to this are regions of the experimental data that come to a sharp peak (especially in the $\alpha = 45°$ region), where the fit seemed to be comparatively shallow. $E^*$ values for varying ion angle of incidence for 500eV $Xe^+$ on Mo ranged from 197eV to 270eV.

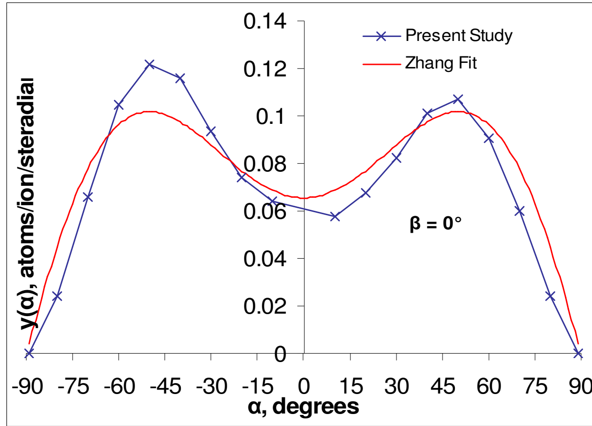


**Figure 5.17: Zhang fit for 500 eV $Xe^+$ on Mo, β= 0°. Y*=0.47 atoms/ion, E*=197 eV, Y=0.44 atoms/ion**

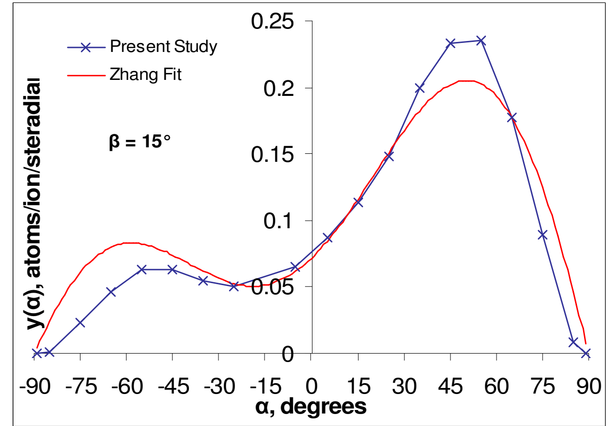


**Figure 5.18: Zhang fit for 500 eV $Xe^+$ on Mo, β= 15°. Y*=0.65 atoms/ion, E*=235 eV, Y=0.58 atoms/ion**

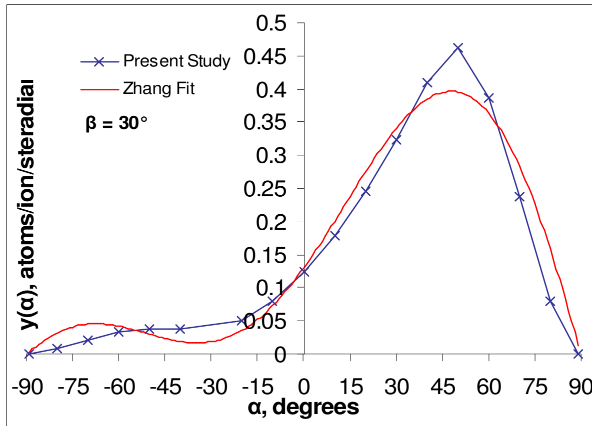


**Figure 5.19: Zhang fit for 500 eV $Xe^+$ on Mo, β= 30°. Y*=0.98 atoms/ion, E*=270 eV, Y=0.93 atoms/ion**

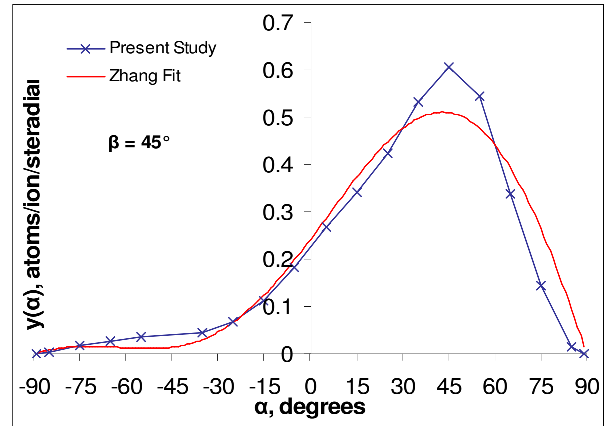


**Figure 5.20: Zhang fit for 500 eV $Xe^+$ on Mo, β= 45°. Y*=1.20 atoms/ion, E*=197 eV, Y=1.18 atoms/ion**

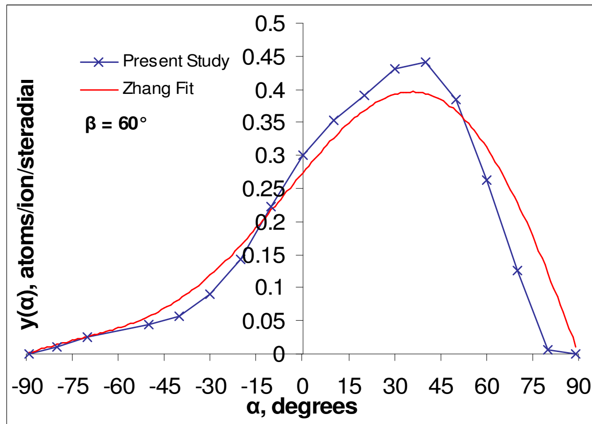


**Figure 5.21: Zhang fit for 500 eV $Xe^+$ on Mo, β= 60°. Y*=1.02 atoms/ion, E*=208 eV, Y=0.87 atoms/ion**

A plot of $E$ vs. $E^*$ for all measured energies at normal ion incidence is shown in Figure 5.22. Yalin[69] noted a trend of $E^*$ values for $Xe^+$ on Mo at normal incidence (see Figure 5.23) approaching $E_{th}$ at a value of $E=E_{th}$ in a similar plot, although Yalin investigated lower ion energies. In Figure 5.22, a pattern such as this cannot be discerned as three of the five target/ion combinations have values of $E^*$ that decrease with increasing $E$, and two (below 1000 eV) have values of $E^*$ that increase with increasing $E$. One note is that ion/target combinations with a $Z$ ratio greater than 0.8 seem to follow this directly proportional relationship with $E$ (below 1000 eV), although investigation into lower energy is needed to further compare to Yalin. It is also noted that the ion/target combinations in Figure 5.22 with a $Z$ ratio greater than 0.8 both have Mo as the target material.

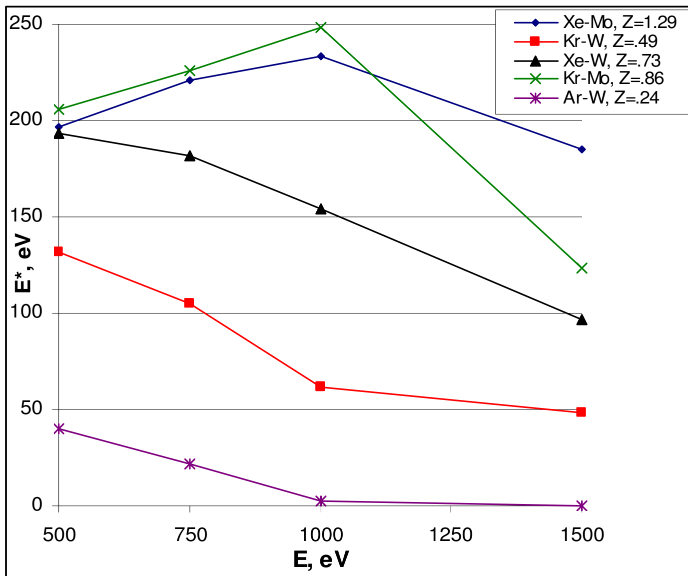


**Figure 5.22: E vs. E* (Zhang fit) for normal incidence of five ion/target combinations.**

Yalin's data also indicated a linear trend of $E$ vs. $E^*$ for all angles of incidence. The data in this study do not show a linear behavior. However, the data collected at 500 and 750 eV for this study (see Figure 5.24) may begin to show this linear behavior, but the existing data does not extend into a low enough energy to confirm this tendency. For non-normal angles of incidence, the extrapolation of the slope between 500 and 750 eV tend toward the origin, as Yalin observed. A similar extrapolation for data collected at normal incidence in this study would tend toward $E^* \sim 150$ eV at $E = 0$ eV. One possible factor contributing to the differences between Yalin and the present study is that the $E^*$ values in this study are based on a single azimuthal plane, whereas Yalin's data was collected above the entire target

hemisphere. Another possible factor is that the present study used a water-cooled plate whereas Yalin's experimental set-up could not accommodate such a cooling scheme, which may slightly affect $E_{th}$.

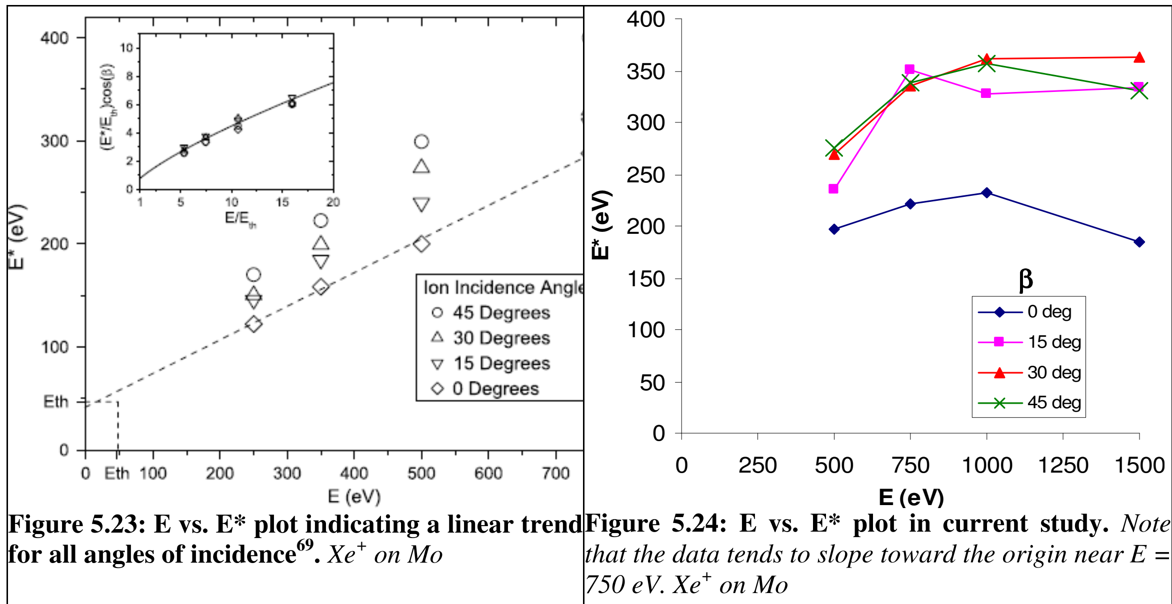


**Figure 5.23: E vs. E* plot indicating a linear trend for all angles of incidence[69].** *$Xe^+$ on Mo*

**Figure 5.24: E vs. E* plot in current study.** *Note that the data tends to slope toward the origin near E = 750 eV. $Xe^+$ on Mo*

The values of the normalized *E*/E* values changed with differing ion incidence angles. Figure 5.25 is a typical $\beta$ vs. *E*/E* plot for the ion/target combinations analyzed. The *E*/E* values would (typically) start at a relatively high value and slowly climb higher until at $\beta$ = 30°, where *E*/E* would decrease steeply. *E** values were noted to be very close to zero for any line-shape that approximated that of a cosine distribution. In

Figure **5.26**, the average of all the *E*/E* values (*E*/E* of all energies and ion incidences) for each ion/target combination is plotted versus the *Z* ratio. A near linear relationship is seen. It is expected that *E*/E* change with differing targets (due to the nature of $E_{th}$), although it is unclear how the combination of ion/target atomic number would create a linear relationship in *E*/E*.

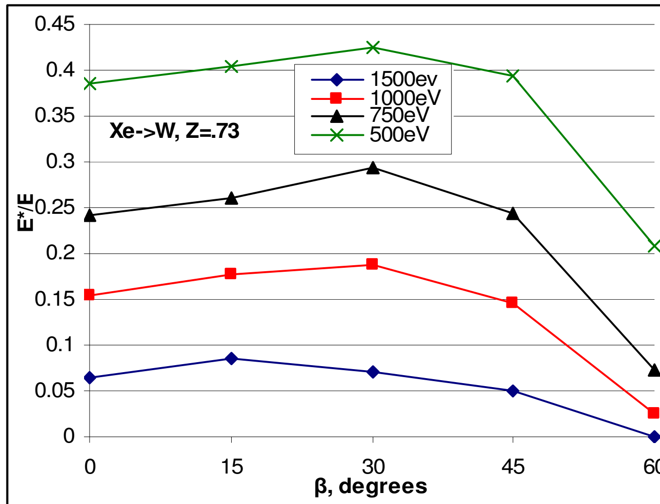


**Figure 5.25: β vs. E*/E for Xe$^+$ on W for four energies.** ***Shape of curves are typical of all data in the current work.***

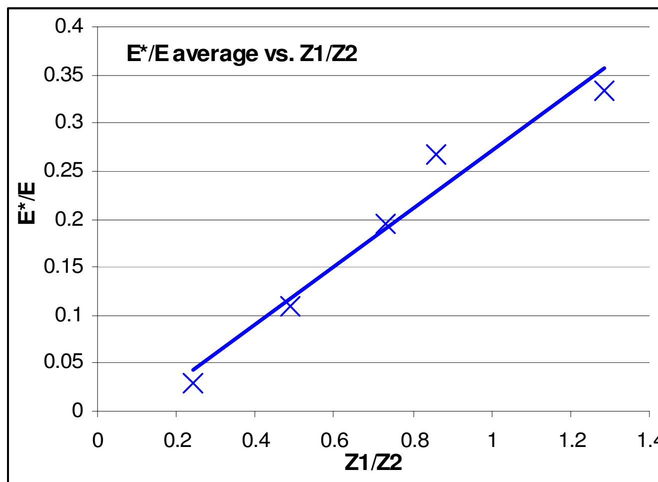


**Figure 5.26: Z ratio versus E*/E average. The E*/E average is the average of all E*/E values for an Ion/Target combination (i.e. at all angles of incidence and at all ion energies).**

## 5.3 Azimuthal Measurements

The azimuthal data (see Appendix C) were obtained using previously described procedures and reduced using the coordinate transform described in Section 4.7. Two programs were used to visualize the data: contours were plotted on Surfer and three dimensional values were plotted on Matlab as shown in Figure 5.27 to Figure 5.34. For β = 45° (Figure 5.27, Figure 5.28), the maximum differential sputter yield occurred at $\phi$= 15°. Intuitively, this maximum should occur along $\phi$= 0° (as the rest of the figures do).

A likely reason for this inconsistency is that for the first measurement, the $\phi = 0°$ position coincided with a limit switch so that when the current to the motor was shut-off, the limit switch moved the target out of position. This would not affect the angle by more than 3°, hence this effect doesn't fully explain the inconsistency. For $\beta = 30°$ (Figure 5.29, Figure 5.30), the limit switch problem was fixed by putting the limit switch 8° from the $\phi = 0°$ position.

The data near the maximum differential sputter yield point display a jump in $\phi = 15°$ direction. The $\beta = 0°$ case (Figure 5.33, Figure 5.34) shows the expected symmetric nature of the normal incident case, although the data is not completely symmetric. Most of the general trends that were expected are seen in these data: The largest maximum occurs in the $\beta = 45°$ case and as the angle of incidence is decreased that maximum value gets smaller and differential yields in the $\phi = 90°$-$180°$ directions get larger. One important trend was that of the $\alpha = 0°$ location having a similar value at all azimuthal angles for a particular angle of incidence.

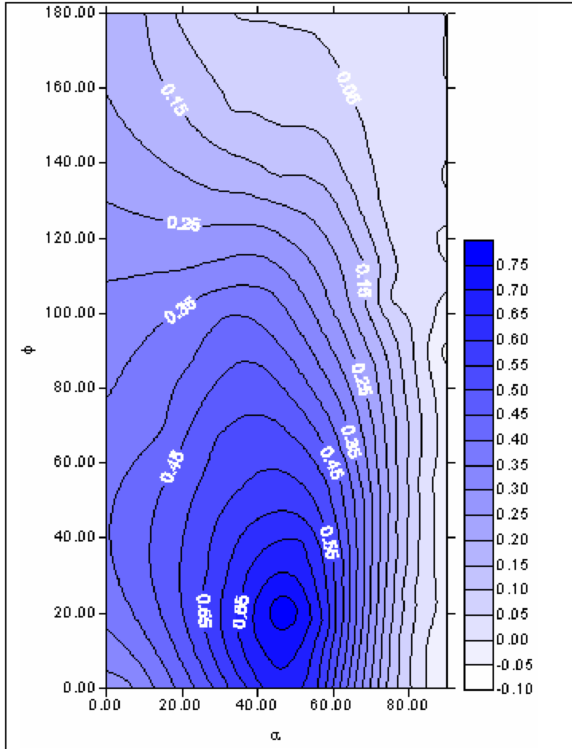


Figure 5.27: Contour plot of differential sputter yields for β = 45°, 500 eV Xe+ on Mo.

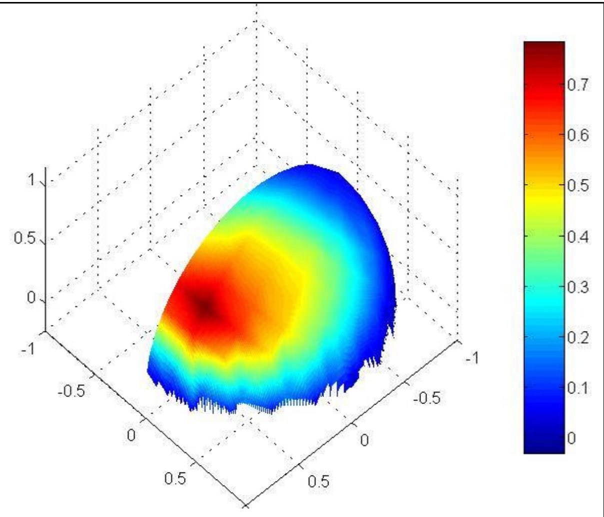


**Figure 5.28: Surface plot on arbitrary sphere showing differential sputter yields in atoms/ion/steradian for β = 45°, 500 eV $Xe^+$ on Mo. Axes are Cartesian (not spherical) coordinates.**

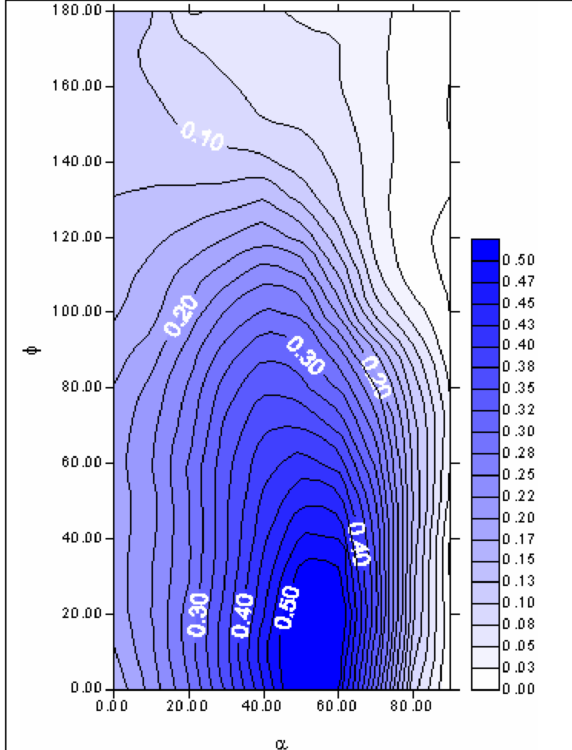


**Figure 5.29: Contour plot of differential sputter for β = 30°, 500 eV $Xe^+$ on Mo.**

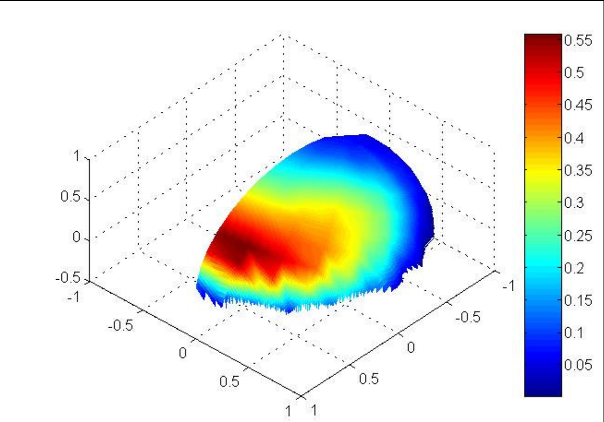


**Figure 5.30: Surface plot on arbitrary sphere showing differential sputter yields in atoms/ion/steradian for β = 30°, 500 eV $Xe^+$ on Mo. Axes are Cartesian (not spherical) coordinates.**

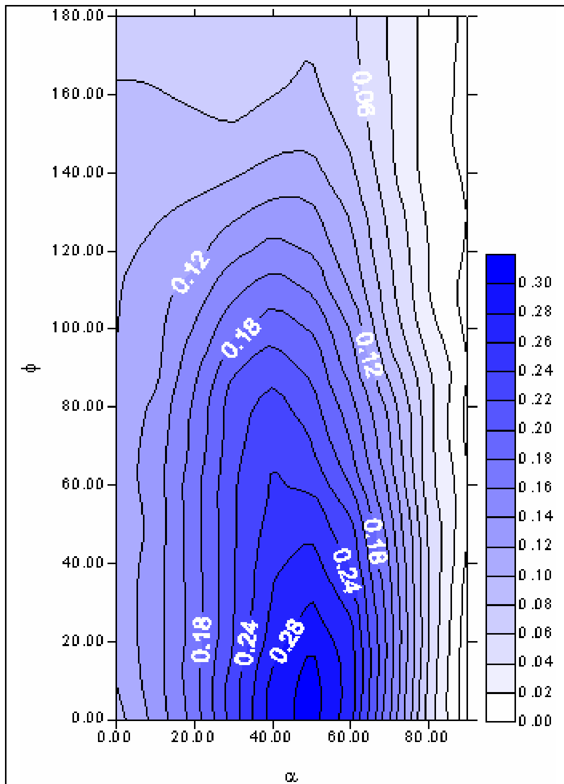


**Figure 5.31: Contour plot of differential sputter for β = 15°, 500 eV $Xe^+$ on Mo.**

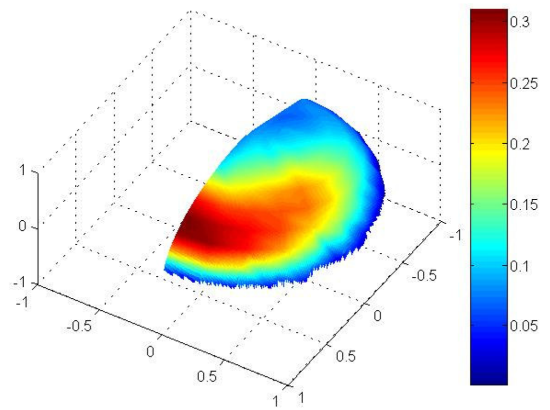


**Figure 5.32: Surface plot on arbitrary sphere showing differential sputter yields in atoms/ion/steradian for β = 15°, 500 eV $Xe^+$ on Mo. Axes are Cartesian (not spherical) coordinates.**

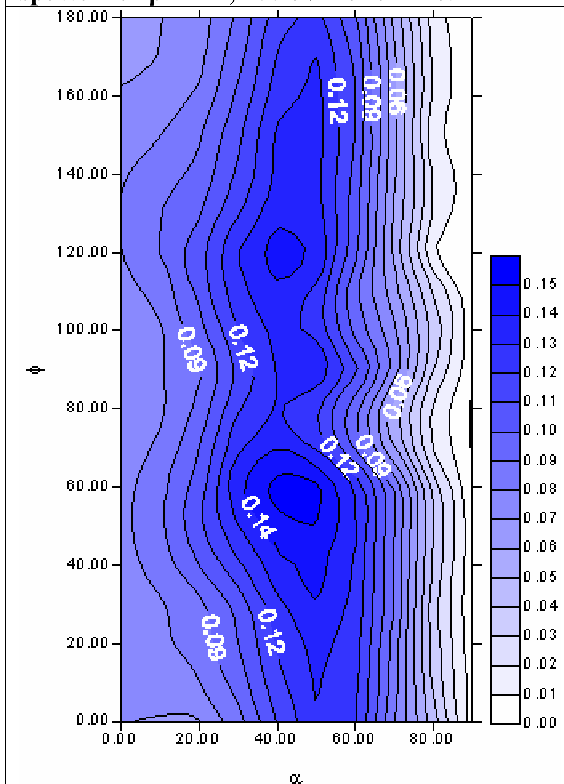


**Figure 5.33: Contour plot of differential sputter for β = 0°, 500 eV $Xe^+$ on Mo.**

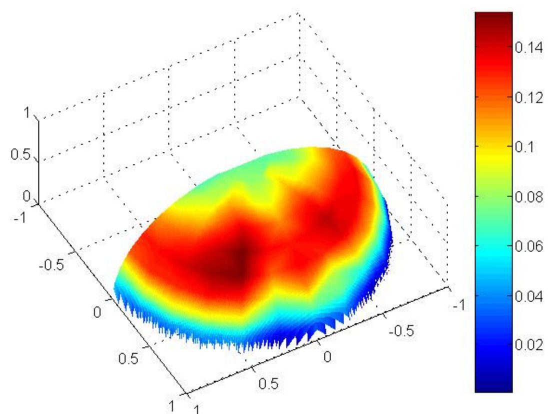


**Figure 5.34: Surface plot on arbitrary sphere showing differential sputter yields in atoms/ion/steradian for β = 0°, 500 eV $Xe^+$ on Mo. Axes are Cartesian (not spherical) coordinates.**

Modified Zhang fits were also applied to the data from the azimuthal experiments to determine if the Zhang fit would correlate well in azimuthal directions other than $\phi = 0°$. To view all the data and the fit to the data in a concise manner, each data point was assigned a number (x-axis) and the differential yield value was plotted on the y-axis. It was found that the Modified Zhang fit correlated very well to the line-shapes of the experimental data (including data at various azimuthal angles). As noted previously, however, the Zhang fit does not resolve the sharp features of the experimental data.

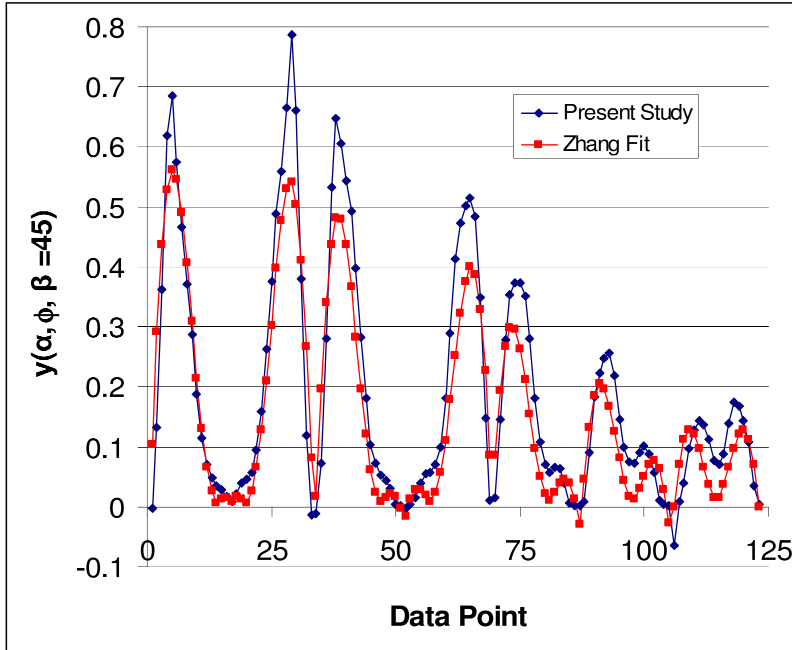


**Figure 5.35: Plot of measured differential sputter yields in β = 45° azimuthal measurement domain to Zhang fit differential sputter yields for 500 eV $Xe^{+}$ on Mo. Y*=1.31 atoms/ion, E*=281 eV.**

## 5.4 Summary

Total sputtering yields at normal incidence were compared to other published values and Yamamura & Tawara curve fits. Trends observed in differential sputtering yield data were discussed and the differential yields were fitted with modified Zhang functions to high levels of correlation.

# Chapter 6 Conclusion and Suggestions for Future Work

A QCM based technique has been used to obtain differential sputtering yield distributions in a single azimuthal plane for ion and target combinations of interest to the EP community. Angles of incidence investigated were 0°, 15°, 30°, 45°, and 60° and bombarding ion energies were from 150 eV to 1500 eV. All experimental distributions obtained in this study are tabulated in Appendix A. The differential yield distributions were integrated using a simple azimuthal assumption to obtain total sputter yields, and these yields were compared to values of other researchers.

The total yields were generally lower than, but comparable to, other groups' experimental values. Comparisons of the differential distributions to those measured by other research groups have shown satisfactory agreement. The total yields measured, as a function of angle of incidence, were also lower than other researchers, however, fits to Yamamura's "angle of incidence" model showed very high correlation, whereas fits to Sigmund's "angle of incidence" model started to diverge sharply near $\beta = 45°$.

This study's measurements show that at 1000 eV and 1500 eV, differential yield distributions at angles of incidence below 60° approach an over-cosine or cosine shape. At lower energy (<800 eV), it was observed that less material was sputtered in the $\alpha = 0°$ region than in the higher energy cases. Distributions for ion and target combinations with a $Z$ ratio less than 0.5 were found to be nearly cosine for lower energies and became over-cosine as the energy increased. Also, at low energies, for ion and target combinations having a $Z$ ratio greater than 0.5, a majority of particles were sputtering in $\alpha = +30°$ to $+60°$ directions, while at high energies these combinations approached a more cosine-like distribution.

The Zhang numerical model was used as a fit to differential sputter yield data. The Zhang fits matched the data very well when the $E_{th}$ parameter was replaced with an $E^*$ parameter that was allowed to vary with ion energy, ion incidence, and $Z$ ratio. The $Y$ parameter in the Zhang fits correlated well to the

total yields obtained when using the azimuthal distribution assumption. In regard to the experimentally obtained azimuthal measurements, the Zhang fit showed good agreement between the general lineshapes.

Analyses of two major assumptions in the experiments were conducted. A simulation was done to investigate the effects of the finite divergence angle and beam spot-size on the differential yield results. The simulations indicated there is a small (5%) discrepancy between measured and simulated QCM values for polar angles near $\alpha = 0°$ and near $\alpha = 45°$, with smaller discrepancies at all other polar angles. However, the small discrepancy may be a result of inputting a known distribution to obtain the desired simulated distribution.

Future work should include measuring sputtering distributions at lower energies (owing to their importance to EP). An experimental investigation into the change in sputtering distributions with changing beam spot sizes should also be done, to verify the simulated results. A more thorough investigation into azimuthal sputter distributions should be made by obtaining more azimuthal distributions with differing ion/target, ion energy, and angle of incidence combinations. The Zhang model should be used as a basis for analysis and further investigation into the relationship between $E^*$ and $E_{th}$ should be completed. Considering that there is a great need to understand sputtering of the Hall thruster insulator channel material, boron nitride, methods to accurately obtain differential sputtering yields for multi-component targets need to be perfected.

# Bibliography


[1] Jahn, R.G. and Choueiri, E.Y., "Electric Propulsion", *Encyclopedia of Physical Science and Technology*, 3rd Edn, vol. 5, 2002, pp. 125-141.

[2] Myers, R.M., "Overview of Major U.S. Industrial Electric Propulsion Programs", *40th Joint Propulsion Conference*, AIAA 2004-3331, Ft. Lauderdale, FL, 2004.

[3] Futron Corporation, "Space Transportation Costs: Trends in Price Per Pound to Orbit 1990-2000", Bethesda, MD, 2002.

[4] Sutton, G. P. and Biblarz, O., *Rocket Propulsion Elements*, 7th ed., New York, John Wiley & Sons, 2001.

[5] Choueiri, E.Y., "A Critical History of Electric Propulsion: The First 50 Years (1906–1956)", *Journal of Propulsion and Power*, Vol. 20, No. 2, 2004, pp. 193-203.

[6] Gallimore, A., "The Past and Future of Rocket Engine Propulsion", Fathom Online Courses, University of Michigan, http://www.fathom.com/course/21701743/session3.html

[7] Mattox, D.M., *The Foundations of Vacuum Coating Technology*, pp. 11-19, Noyes Publications, New York, 2003.

[8] Grove, W.R., "On the Electrochemical Polarity of Gases", *Philosophical Transactions Royal Society (London)*, B142, 87, 1852.

[9] Wright, A.W., "On the Production of Transparent Metallic Films by Electrical Discharge in Exhausted Tubes", *American Journal of Science and Arts*, Vol. 13, pp. 49-55, 1877.

[10] American Vacuum Society, "Vacuum Science and Technology Timeline: 1500-2003", www.avs.org/pdf/timeline.pdf.

[11] Bay, H.L., Bohdansky, J., Hofer, W.O., and Roth, J., "Angular Distribution and Differential Sputtering Yields for Low-Energy Light-Ion Irradiation of Polycrystalline Nickel and Tungsten", *Applied Physics*, Vol. 21, 1980, pp. 327-333.

[12] Sigmund, P., "Sputtering by Ion Bombardment: Theoretical Concepts", *Sputtering by Particle Bombardment I*, pp. 9-71, ed. Behrisch, R., Springer-Verlag, Berlin, 1981.

[13] Stocker, B.J., "Cathode Sputtering in Inert-gas Glow Discharges", *British Journal of Applied Physics*, Vol. 12, 1961, pp. 465-468.

[14] Keywell, F., "Measurements and Collision-Radiation Damage Theory of High Vacuum Sputtering", *Physical Review*, Vol. 97, no. 6, 1955, pp. 1611-1619.

[15] Wehner, G.K., "Controlled Sputtering of Metals by Low-Energy Hg Ions", *Physical Review*, Vol. 102, no. 3, 1956, pp. 690-704.

[16] Alexander, C., "The Neutral Source for the Exosphere of Ganymede from Sputtering and Sublimation Processes Combined", *American Geophysical Union Fall meeting*, San Francisco, CA, 1999.

[17] Baragiola, R.A., “Sputtering: Survey of Observations and Derived Principles”, *Philosophical Transactions Royal Society of London A.*, Vol. 362, pp. 29-53

[18] Duchemin, O.B., *An Investigation of Ion Engine Erosion by Low Energy Sputtering*, Ph. D. Dissertation, California Institute of Technology, Pasadena, CA, 2001.

[19] Monheiser, J.M. and Wilbur, P.J., “Advanced Electric Propulsion Research”, NASA CR-187103, 1991.

[20] Nakles, M.R., *Experimental and Modeling Studies of Low Energy Ion Sputtering for Ion Thrusters*, M.S. Thesis, Department of Aerospace Engineering, Virginia Polytechnic Institute, Blacksburg, VA, 2004.

[21] Kolasinski, R.D. and Polk, J.E., “Cathode Keeper Orifice Wear Measurements Using Surface Layer Activation”, 41st *Joint Propulsion Conference*, AIAA Paper 2005-3664, Tucson, AZ, 2005.

[22] Dolaghen, J.S., *Monte Carlo Simulation of Molecular Redistribution in an Enclosure due to Sputtering*, M.S. Thesis, Department of Mechanical Engineering, Colorado State University, Fort Collins, CO, 1991.

[23] Behrisch, R., “Introduction and Overview”, *Sputtering by Particle Bombardment I*, pp. 1-8, ed. Behrisch, R., Springer-Verlag, Berlin, 1981.

[24] Behrisch, R., “Introduction”, *Sputtering by Particle Bombardment III*, pp. 1-13, ed. Behrisch, R., Springer-Verlag, Berlin, 1991.

[25] Smentkowski, V.S., Wei, C., and Browall, K., “Summary of Sputter Yield Literature”, General Electric Research and Development Center, General Electric Company, 1999.

[26] Stepanova, M., Dew, S.K., Shoshnikov, I.P., “Sputtering from Ion-Beam-Roughened Cu Surfaces”, *Physical Review B*, Vol. 66, 2002, pp. 125407-1 to 125407-8.

[27] Wilbur, P.J., “Surface Interactions Handout”, Course: *Broad Beam Ion Sources*, Colorado State University, Fort Collins, CO, 2005.

[28] Betz, G. and Wien, K., “Energy and Angular Distributions of Sputtered Particles”, *International Journal of Mass Spectrometry and Ion Processes*, Vol. 140, 1994, pp. 1-110.

[29] Sigmund, P., “Theory of Sputtering. I. Sputtering Yield of Amorphous and Polycrystalline Targets”, *Physical Review*, vol. 184, no. 2, 1969, pp. 383-416.

[30] Wilson, W.D., Haggmark, L.G., and Biersack, J.P., “Calculation of Nuclear Stopping, Ranges, and Straggling in the Low-Energy Region”, *Physical Review B*, vol. 15, no. 5, 1977, pp. 2458-2468.

[31] Ziegler, J.F., Biersack, J.P., and Littmark, L., *The Stopping and Range of Ions in Solids*, Permagon Press, New York, 1985.

[32] Zalm, P.C., “Energy Dependence of the Sputtering of Silicon Bombarded with Neon, Argon, Krypton, and Xenon Ions”, *Journal of Applied Physics*, vol. 54, no. 5, 1983, pp. 2660-2666.

[33] Yamamura, Y. and Tawara, H., “Energy Dependence of Ion Induced Sputtering Yields from Monatomic Solids at Normal Incidence”, *Atomic Data and Nuclear Data Tables*, Vol. 62, 1996, pp. 149-253.

[34] Yamamura, Y., “An Empirical Formula for Angular Dependence of Sputtering Yields”, *Radiation Effects*, vol. 80, 1984, pp.57-72.

[35] Zhang, Z. and Zhang, L., "Anisotropic Angular Distributions of Sputtered Atoms", *Radiation Effects and Defects in Solids*, vol. 159, 2004, pp. 301-307.

[36] Yamamura, Y., "Contribution of Anisotropic Velocity Distribution of Recoil Atoms to Sputtering Yields and Angular Distributions of Sputtered Atoms", *Radiation Effects*, vol. 55, 1981, pp. 49-56.

[37] Yalin, A., Williams, J., et. al., "Azimuthal Differential Sputter Yields of Molybdenum by Low Energy $Xe^+$ Bombardment", *42nd Joint Propulsion Conference*, AIAA Paper 2006-4336, Sacramento, CA, 2006.

[38] Hofer, W., "Angular, Energy, and Mass Distribution of Sputtered Particles", *Sputtering by Particle Bombardment III*, pp. 15-90, ed. Behrisch, R., Springer-Verlag, Berlin, 1991.

[39] Whitaker, T., Li, A., Jones, P., and Watts, R., "Angular Distributions of Sputtered Zirconium Atoms", *Journal of Chemical Physics*, vol. 98, 1993, pp. 5887-5898.

[40] Duchemin, O.B., et. al., "A Review of Low Energy Sputtering Theory and Experiments", *25st International Electric Propulsion Conference*, IEPC Paper 97-068, Cleveland, OH, 1997.

[41] Fine, J., "Absolute Sputtering Yield Measurement Methods: A Review", *The Physics of Ionized Gases*, ed. Matic, M., pp. 379-420, Boris Kidric Institute of Nuclear Sciences, Belgrade, Serbia, 1980.

[42] Charles Evans Group, "Rutherford Backscattering Spectrometry Theory Tutorials", http://www.cea.com/training/tutorials/rbs_theory_tutorial/

[43] Govil, I.M., "Proton Induced X-ray Emission-A Tool for Non-destructive Trace Element Analysis", *Current Science*, vol. 80, 2001, pp. 1542-49.

[44] Lawerence Berkeley National Laboratory, "Ion Beam Techniques for Material Characterization", http://www.lbl.gov/~msd/Internal/Facilities/MSD_Ion_Beam.html

[45] Wafer Bumping, http://www.wafer-bumping.com/documents/techno/metrology.html

[46] Surla, V., *Sputter Erosion Measurements by Cavity Ring-down Spectroscopy*, M.S. Thesis, Department of Mechanical Engineering, Colorado State University, Fort Collins, CO, 2004.

[47] Ray, P.K., and Shutthanandan, V., "Low-Energy Sputtering Research", NASA CR-1999-209161, 1999.

[48] Oyarzabel, J., Yu, J., Hanna, J., Tynan, G., Doerner, R., Taylor, K., and Schmid, K., "Molybdenum and Carbon Cluster Angular Sputtering Distributions Under Low Energy Xenon Ion Bombardment", *41st Joint Propulsion Conference*, AIAA Paper 2005-3525, Tucson, AZ, 2005.

[49] Kelson, I., Levy, Y., and Redmard, E., "Recoil Implantation of Alpha Sources for Thickness Measurement of Thin Films", *Journal of Applied Physics D*, vol. 28, 1995, pp. 100-104.

[50] Southwest Research Institute, "Overview of the Bulk Activation Radioactive Tracer Test Method", http://www.swri.org/4org/d03/vehsys/radtrace/PDFs/rattpaper.pdf

[51] Polk, J., Jaskowsky, W., Kelly, A., and Jahn, R., "Measurement of MPD Thruster Erosion Using Surface Layer Activation", *Journal of Propulsion and Power*, vol. 3, 1987, pp. 33-38.

[52] Stanford Research Systems, Inc., "QCM100-Quartz Crystal Microbalance Theory and Calibration", http://www.thinksrs.com/downloads/PDFs/ApplicationNotes/QCMTheoryapp.pdf

[53] Tel Aviv University, "Quartz Crystal Microbalance (QCM)", http://www.tau.ac.il/~phchlab/experiments/QCM/QCM.html

[54] International Crystal Manufacturing Co, Inc., "Crystal Data", http://www.icmfg.com/technicaldata.html.

[55] Narine, S. and Slavin, A., "Use of the Quartz Crystal Microbalance to Measure the Mass of Submonolayer Deposits: Measuring the Stoichiometry of Surface Oxides", *Journal of Vacuum Science Technology A.*, vol. 16, 1998, pp. 1857-1862.

[56] Kolasinski, R., "Oblique Angle Sputtering Yield Measurements for Ion Thruster Grid Materials", *41st Joint Propulsion Conference*, AIAA paper 2005-3526, Tuscon, AZ, 2005.

[57] Mantenieks, M., Ray, P., Shutthanandan, S., and Thevuthasan, T., "Low Energy Xenon Ion Sputtering Yield Measurements", *27th International Electric Propulsion Conference*, IEPC Paper IEPC-01-309, Pasadena, CA, 2001.

[58] Huange, W., "Angular Resolved Sputtering Yields of Noble Metals and an Au-Ag Alloy", *Surface and Interface Analysis*, vol. 14, 1989, pp. 469-476.

[59] Smith, P., and Ruzic, D., "Low Energy (10 to 700 eV) Angularly Resolved Sputtering Yields for $D^+$ on Beryllium", *Nuclear Fusion*, vol. 38, 1998, pp. 673-680.

[60] Chini, T., Tanemura, M., and Okuyama, F., "Angular Distribution of Sputtered Ge Atoms by Low keV $Ar^+$ and $Ne^+$ Ion Bombardment", *Nuclear Instruments and Methods in Physics Research B*, vol. 119, 1996, pp. 387-391.

[61] Mannami, M., Kimura, K., and Kyoshima, A., "Angular Distribution Measurements of Sputtered Au Atoms with Quartz Oscillator Microbalances", *Nuclear Instruments and Methods*, vol. 185, 1981, pp. 533-537.

[62] Williams, J., Johnson, M., and Williams, D., "Differential Sputtering Behavior of Pyrolytic Graphite and Carbon-Carbon Composite Under Xenon Bombardment", *40th Joint Propulsion Conference*, AIAA Paper 2004-3788, Fort Lauderdale, FL, 2004.

[63] Williams, J., Gardner, M., Johnson, M., and Wilbur, P., "Xenon Sputter Yield Measurements for Ion Thruster Materials", NASA CR-2003-212306, 2003.

[64] Shutthanandan, V., Ray, P., Shivaparan, N., Smith, R., Thevuthasan, T., and Mantenieks, M., "On the Measurement of Low-Energy Sputtering Yield Using Rutherford Backscattering Spectrometry," *25th International Electric Propulsion Conference*, IEPC-97-069, Cleveland, OH, 1997.

[65] Doerner, R., Whyte, D., and Goebel, D., "Sputtering Yield Measurements During Low Energy Xenon Plasma Bombardment," *Journal of Applied Physics*, vol. 93, 2003, pp. 5816-5823.

[66] Doerner, R., and Goebel, D., "Sputtering Yields of Ion Thruster Grid and Cathode Materials During Very Low Energy Xenon Plasma Bombardment," *39th Joint Propulsion Conference*, AIAA Paper 2003-4561, 2003

[67] Blandino, J., Goodwin, G., and Garner, C., "Low Energy Sputter Yields for Diamond, Carbon-Carbon, Composite, and Molybdenum Subject to Xenon Ion Bombardment," *Diamond and Related Materials*, vol. 9, 2000, pp. 1992-2001.

[68] Tartz, M., Neumann, H., Fritsche, B., Leiter, H., and Esch, J., "Investigation of Sputter Behaviour of Ion Thruster Grid Materials," *40$^{th}$ Joint Propulsion Conference*, AIAA Paper 2004-4114, 2004.

[69] Yalin, A, Williams, J., Surla, V., and Zoerb, K., "Differential Sputter Yield Profiles of Molybdenum due to Bombardment by Low Energy Xenon Ions at Normal and Oblique Incidence", *Journal of Applied Physics D*, vol. 40, 2007, pp. 3194-3202.

## Appendix A:

## Table of Polynomial Curve Fit Coefficients to Experimental Data

## Eqn. 4.4 to Eqn. 4.6

| E (eV) | β ° | Target | Ion | Y (atoms/ion) | A6 | A5 | A4 | A3 | A2 | A1 | B6 | B5 | B4 | B3 | B2 | B1 |
|---|---|---|---|---|---|---|---|---|---|---|---|---|---|---|---|---|
| 500 | 0 | W | Xe | 0.74 | 5.166E+00 | -1.432E+01 | 1.572E+01 | -9.500E+00 | 3.196E+00 | -1.579E-01 | 1.675E+00 | -3.437E+00 | 2.703E+00 | -2.133E+00 | 1.158E+00 | 1.393E-01 |
| 500 | 5 | W | Xe | 0.74 | 9.299E+00 | -2.738E+01 | 3.175E+01 | -1.916E+01 | 6.013E+00 | -3.908E-01 | 1.224E+01 | -3.425E+01 | 3.706E+01 | -2.022E+01 | 5.667E+00 | -3.676E-01 |
| 500 | 15 | W | Xe | 0.83 | 1.119E+00 | -1.411E+00 | 4.254E-01 | -2.337E+00 | 2.531E+00 | -1.881E-01 | 9.066E+00 | -2.497E+01 | 2.674E+01 | -1.441E+01 | 3.852E+00 | -1.506E-01 |
| 500 | 30 | W | Xe | 0.92 | -4.156E+00 | 1.677E+01 | -2.427E+01 | 1.317E+01 | -1.533E+00 | 2.143E-01 | 1.772E+01 | -4.764E+01 | 4.863E+01 | -2.363E+01 | 5.393E+00 | -3.096E-01 |
| 500 | 45 | W | Xe | 0.96 | 2.952E+00 | -3.428E+00 | -5.053E+00 | 6.730E+00 | -1.087E+00 | 1.718E-01 | 2.654E+01 | -7.053E+01 | 6.973E+01 | -3.137E+01 | 6.149E+00 | -2.622E-01 |
| 500 | 60 | W | Xe | 0.68 | -1.436E+01 | 4.861E+01 | -6.492E+01 | 4.055E+01 | -1.048E+01 | 8.962E-01 | 1.955E+01 | -5.594E+01 | 6.125E+01 | -3.132E+01 | 7.198E+00 | -4.607E-01 |
| 750 | 0 | W | Xe | 1.13 | 9.689E+00 | -2.579E+01 | 2.666E+01 | -1.469E+01 | 4.629E+00 | -2.411E-01 | -1.666E+00 | 1.020E+01 | -1.632E+01 | 8.735E+00 | -9.194E-01 | 2.355E-01 |
| 750 | 5 | W | Xe | 1.14 | 9.197E+00 | -2.533E+01 | 2.757E+01 | -1.638E+01 | 5.572E+00 | -3.553E-01 | 1.222E+01 | -3.249E+01 | 3.365E+01 | -1.834E+01 | 5.504E+00 | -2.776E-01 |
| 750 | 15 | W | Xe | 1.22 | 7.732E+00 | -1.823E+01 | 1.609E+01 | -9.066E+00 | 4.073E+00 | -2.647E-01 | 1.424E+01 | -3.679E+01 | 3.693E+01 | -1.903E+01 | 5.207E+00 | -2.419E-01 |
| 750 | 30 | W | Xe | 1.41 | 7.304E+00 | -1.517E+01 | 8.958E+00 | -3.132E+00 | 2.534E+00 | -7.463E-02 | 2.853E+01 | -7.645E+01 | 7.828E+01 | -3.845E+01 | 9.038E+00 | -5.436E-01 |
| 750 | 45 | W | Xe | 1.49 | 1.778E-01 | 1.140E+01 | -2.980E+01 | 2.360E+01 | -5.391E+00 | 5.500E-01 | 3.255E+01 | -8.608E+01 | 8.579E+01 | -3.973E+01 | 8.335E+00 | -3.593E-01 |
| 750 | 60 | W | Xe | 1.22 | 1.443E+01 | -3.755E+01 | 3.066E+01 | -7.277E+00 | 6.912E-02 | 1.939E-01 | -7.309E+00 | 2.657E+01 | -3.279E+01 | 1.754E+01 | -4.095E+00 | 6.085E-01 |
| 1000 | 0 | W | Xe | 1.40 | 3.930E+00 | -7.607E+00 | 5.086E+00 | -2.861E+00 | 1.743E+00 | 7.174E-02 | 5.305E+00 | -1.267E+01 | 1.229E+01 | -8.022E+00 | 3.583E+00 | -1.222E-01 |
| 1000 | 5 | W | Xe | 1.38 | 1.158E+01 | -3.064E+01 | 3.151E+01 | -1.750E+01 | 5.812E+00 | -3.776E-01 | 1.078E+01 | -2.819E+01 | 2.934E+01 | -1.679E+01 | 5.515E+00 | -2.704E-01 |
| 1000 | 15 | W | Xe | 1.45 | 1.193E+01 | -2.910E+01 | 2.660E+01 | -1.381E+01 | 5.179E+00 | -3.390E-01 | 1.934E+01 | -5.079E+01 | 5.134E+01 | -2.597E+01 | 6.899E+00 | -3.822E-01 |
| 1000 | 30 | W | Xe | 1.62 | 1.020E+01 | -2.456E+01 | 2.049E+01 | -9.303E+00 | 3.956E+00 | -2.100E-01 | 2.640E+01 | -6.871E+01 | 6.862E+01 | -3.332E+01 | 7.939E+00 | -3.858E-01 |
| 1000 | 45 | W | Xe | 1.71 | 2.551E+00 | 1.764E+00 | -1.446E+01 | 1.222E+01 | -1.483E+00 | 7.055E-02 | 2.734E+01 | -7.204E+01 | 7.271E+01 | -3.498E+01 | 7.984E+00 | -3.510E-01 |
| 1000 | 60 | W | Xe | 1.52 | 3.833E+01 | -1.142E+02 | 1.246E+02 | -6.130E+01 | 1.445E+01 | -1.151E+00 | 5.747E+00 | -1.193E+01 | 9.686E+00 | -3.967E+00 | 7.739E-01 | 3.573E-01 |
| 1500 | 0 | W | Xe | 1.77 | 1.311E+01 | -3.591E+01 | 3.820E+01 | -2.116E+01 | 6.708E+00 | -4.399E-01 | -9.462E+00 | 3.268E+01 | -4.057E+01 | 2.086E+01 | -3.658E+00 | 6.671E-01 |
| 1500 | 5 | W | Xe | 1.79 | 1.114E+01 | -3.058E+01 | 3.360E+01 | -2.017E+01 | 7.035E+00 | -4.676E-01 | 1.929E+01 | -5.305E+01 | 5.655E+01 | -3.066E+01 | 8.873E+00 | -4.601E-01 |
| 1500 | 15 | W | Xe | 1.86 | 7.790E+00 | -1.737E+01 | 1.499E+01 | -9.053E+00 | 4.600E+00 | -3.052E-01 | 1.984E+01 | -5.043E+01 | 4.945E+01 | -2.494E+01 | 7.008E+00 | -3.198E-01 |
| 1500 | 30 | W | Xe | 2.06 | 3.456E+01 | -9.589E+01 | 9.998E+01 | -5.090E+01 | 1.416E+01 | -1.106E+00 | 2.314E+01 | -5.647E+01 | 5.314E+01 | -2.518E+01 | 6.316E+00 | -1.443E-01 |
| 1500 | 45 | W | Xe | 2.13 | 1.559E+00 | 7.245E+00 | -2.287E+01 | 1.751E+01 | -2.712E+00 | 1.510E-01 | 1.893E+01 | -4.962E+01 | 5.150E+01 | -2.659E+01 | 6.859E+00 | -2.061E-01 |
| 1500 | 60 | W | Xe | 2.04 | 6.286E+01 | -1.859E+02 | 2.015E+02 | -9.695E+01 | 2.069E+01 | -1.269E+00 | -2.773E+01 | 8.808E+01 | -1.023E+02 | 5.370E+01 | -1.251E+01 | 1.636E+00 |
| 500 | 0 | W | Ar | 0.51 | 5.610E+00 | -1.618E+01 | 1.806E+01 | -1.004E+01 | 2.895E+00 | -1.911E-01 | -5.513E-01 | 3.373E+00 | -5.300E+00 | 2.810E+00 | -3.143E-01 | 1.346E-01 |
| 500 | 5 | W | Ar | 0.52 | 4.108E+00 | -1.113E+01 | 1.192E+01 | -6.797E+00 | 2.200E+00 | -1.234E-01 | 8.253E+00 | -2.205E+01 | 2.230E+01 | -1.107E+01 | 2.900E+00 | -1.699E-01 |
| 500 | 15 | W | Ar | 0.54 | 4.629E+00 | -1.136E+01 | 1.041E+01 | -5.117E+00 | 1.718E+00 | -1.037E-01 | 5.847E+00 | -1.475E+01 | 1.407E+01 | -6.687E+00 | 1.694E+00 | -2.750E-03 |
| 500 | 30 | W | Ar | 0.60 | 1.007E+01 | -2.775E+01 | 2.883E+01 | -1.479E+01 | 4.100E+00 | -2.699E-01 | 1.329E+00 | -1.196E+00 | -8.694E-01 | 8.432E-01 | -1.422E-02 | 1.051E-01 |
| 500 | 45 | W | Ar | 0.65 | -4.319E+00 | 1.814E+01 | -2.712E+01 | 1.719E+01 | -4.149E+00 | 4.645E-01 | 1.686E+00 | -4.029E+00 | 4.484E+00 | -2.998E+00 | 1.001E+00 | 6.040E-02 |
| 500 | 60 | W | Ar | 0.57 | -7.395E+00 | 3.138E+01 | -4.864E+01 | 3.324E+01 | -9.245E+00 | 8.586E-01 | 1.416E+00 | -1.952E+00 | -1.005E-01 | 1.122E+00 | -5.374E-01 | 2.405E-01 |
| 750 | 0 | W | Ar | 0.70 | 2.926E+00 | -7.436E+00 | 7.541E+00 | -4.409E+00 | 1.670E+00 | -7.588E-02 | -6.079E-01 | 3.823E+00 | -5.911E+00 | 2.973E+00 | -2.163E-01 | 1.619E-01 |
| 750 | 5 | W | Ar | 0.67 | 5.712E+00 | -1.530E+01 | 1.604E+01 | -8.771E+00 | 2.698E+00 | -1.488E-01 | 6.296E+00 | -1.630E+01 | 1.627E+01 | -8.402E+00 | 2.442E+00 | -8.818E-02 |
| 750 | 15 | W | Ar | 0.72 | 8.749E+00 | -2.177E+01 | 2.034E+01 | -9.720E+00 | 2.829E+00 | -1.675E-01 | 8.480E+00 | -2.089E+01 | 1.957E+01 | -9.320E+00 | 2.493E+00 | -7.092E-02 |
| 750 | 30 | W | Ar | 0.80 | 2.372E+01 | -6.545E+01 | 6.794E+01 | -3.372E+01 | 8.475E+00 | -6.351E-01 | 3.468E+00 | -5.380E+00 | 2.090E+00 | -2.696E-01 | 2.828E-01 | 1.362E-01 |
| 750 | 45 | W | Ar | 0.85 | 7.915E-01 | 3.662E+00 | -1.139E+01 | 8.926E+00 | -1.886E+00 | 2.085E-01 | -3.009E+00 | 9.417E+00 | -9.185E+00 | 2.857E+00 | 9.905E-02 | 1.379E-01 |
| 750 | 60 | W | Ar | 0.83 | 9.257E-01 | 9.080E+00 | -2.684E+01 | 2.381E+01 | -7.396E+00 | 7.280E-01 | -8.126E+00 | 2.685E+01 | -3.206E+01 | 1.694E+01 | -3.866E+00 | 5.680E-01 |
| 1000 | 0 | W | Ar | 0.75 | 6.670E+00 | -1.834E+01 | 1.959E+01 | -1.069E+01 | 3.223E+00 | -2.081E-01 | 3.288E+00 | -1.300E+01 | 2.141E+01 | -1.787E+01 | 7.213E+00 | -7.969E-01 |
| 1000 | 15 | W | Ar | 0.85 | 1.160E+01 | -2.922E+01 | 2.796E+01 | -1.368E+01 | 3.911E+00 | -2.400E-01 | 1.182E+01 | -2.974E+01 | 2.836E+01 | -1.347E+01 | 3.490E+00 | -1.425E-01 |
| 1000 | 30 | W | Ar | 0.98 | 3.618E+01 | -1.006E+02 | 1.054E+02 | -5.261E+01 | 1.306E+01 | -1.047E+00 | 5.463E+00 | -9.185E+00 | 4.438E+00 | -9.106E-01 | 4.158E-01 | 2.052E-01 |
| 1000 | 45 | W | Ar | 1.01 | 1.041E+01 | -2.465E+01 | 2.022E+01 | -7.652E+00 | 2.211E+00 | -1.584E-01 | -1.538E+01 | 4.426E+01 | -4.469E+01 | 1.856E+01 | -2.648E+00 | 3.085E-01 |
| 1000 | 60 | W | Ar | 1.04 | 1.243E+01 | -2.532E+01 | 1.232E+01 | 3.176E+00 | -2.573E+00 | 3.640E-01 | -2.372E+01 | 7.279E+01 | -8.180E+01 | 4.107E+01 | -9.015E+00 | 1.098E+00 |
| 1500 | 0 | W | Ar | 0.92 | 7.257E+00 | -1.916E+01 | 1.995E+01 | -1.095E+01 | 3.406E+00 | -1.861E-01 | 3.077E+00 | -7.355E+00 | 7.454E+00 | -4.763E+00 | 1.891E+00 | 2.058E-02 |
| 1500 | 15 | W | Ar | 1.01 | 1.065E+01 | -2.593E+01 | 2.413E+01 | -1.189E+01 | 3.674E+00 | -2.252E-01 | 1.682E+01 | -4.395E+01 | 4.341E+01 | -2.071E+01 | 5.007E+00 | -1.918E-01 |
| 1500 | 30 | W | Ar | 1.20 | 4.081E+01 | -1.135E+02 | 1.195E+02 | -6.005E+01 | 1.498E+01 | -1.194E+00 | 2.200E+00 | 3.884E-01 | -5.822E+00 | 3.741E+00 | -2.654E-01 | 2.650E-01 |
| 1500 | 45 | W | Ar | 1.30 | 1.729E+01 | -4.601E+01 | 4.603E+01 | -2.279E+01 | 6.612E+00 | -6.843E-01 | -3.234E+01 | 9.222E+01 | -9.553E+01 | 4.268E+01 | -7.233E+00 | 6.757E-01 |
| 1500 | 60 | W | Ar | 1.25 | 3.781E+01 | -1.058E+02 | 1.089E+02 | -5.022E+01 | 1.047E+01 | -6.708E-01 | -3.378E+01 | 1.044E+02 | -1.193E+02 | 6.156E+01 | -1.413E+01 | 1.716E+00 |

| E (eV) | β ° | Target | Ion | Y (atoms/ion) | A6 | A5 | A4 | A3 | A2 | A1 | B6 | B5 | B4 | B3 | B2 | B1 |
|---|---|---|---|---|---|---|---|---|---|---|---|---|---|---|---|---|
| 500 | 0 | W | Kr | 0.72 | 1.056E+01 | -3.099E+01 | 3.524E+01 | -2.004E+01 | 5.819E+00 | -4.405E-01 | -6.362E+00 | 2.194E+01 | -2.714E+01 | 1.407E+01 | -2.767E+00 | 4.278E-01 |
| 500 | 15 | W | Kr | 0.79 | -3.159E-01 | 2.103E+00 | -2.451E+00 | -8.650E-01 | 1.851E+00 | -1.297E-01 | 5.687E+00 | -1.488E+01 | 1.593E+01 | -9.499E+00 | 3.100E+00 | -1.554E-01 |
| 500 | 30 | W | Kr | 0.87 | 6.144E+00 | -1.658E+01 | 1.757E+01 | -1.110E+01 | 4.566E+00 | -3.701E-01 | 8.001E+00 | -2.011E+01 | 1.982E+01 | -1.010E+01 | 2.712E+00 | -9.504E-02 |
| 500 | 45 | W | Kr | 0.88 | 5.058E-01 | 7.677E+00 | -2.138E+01 | 1.749E+01 | -4.526E+00 | 5.062E-01 | 1.161E+01 | -3.055E+01 | 3.097E+01 | -1.513E+01 | 3.456E+00 | -8.068E-02 |
| 500 | 60 | W | Kr | 0.75 | 1.658E+01 | -4.599E+01 | 4.447E+01 | -1.795E+01 | 3.259E+00 | -1.009E-01 | -1.239E-01 | 3.652E+00 | -6.640E+00 | 4.245E+00 | -1.210E+00 | 3.442E-01 |
| 750 | 0 | W | Kr | 1.05 | -2.741E+00 | 7.167E+00 | -5.538E+00 | -1.635E-01 | 1.599E+00 | -6.025E-02 | -6.248E+00 | 2.184E+01 | -2.680E+01 | 1.321E+01 | -2.085E+00 | 3.641E-01 |
| 750 | 15 | W | Kr | 1.10 | 1.123E+01 | -2.792E+01 | 2.630E+01 | -1.353E+01 | 4.576E+00 | -2.989E-01 | 1.365E+01 | -3.528E+01 | 3.527E+01 | -1.801E+01 | 4.952E+00 | -2.517E-01 |
| 750 | 30 | W | Kr | 1.22 | 1.951E+01 | -5.158E+01 | 5.070E+01 | -2.483E+01 | 7.118E+00 | -5.071E-01 | 1.447E+01 | -3.729E+01 | 3.774E+01 | -1.940E+01 | 5.139E+00 | -2.373E-01 |
| 750 | 45 | W | Kr | 1.27 | -2.222E+00 | 1.909E+01 | -3.767E+01 | 2.725E+01 | -6.627E+00 | 6.356E-01 | 9.748E+00 | -2.466E+01 | 2.481E+01 | -1.266E+01 | 3.205E+00 | 9.605E-03 |
| 750 | 60 | W | Kr | 1.14 | 2.988E+01 | -8.223E+01 | 8.024E+01 | -3.331E+01 | 6.186E+00 | -3.020E-01 | -2.205E+00 | 1.117E+01 | -1.598E+01 | 9.094E+00 | -2.139E+00 | 5.154E-01 |
| 1000 | 0 | W | Kr | 1.20 | 9.760E+00 | -2.607E+01 | 2.748E+01 | -1.567E+01 | 5.294E+00 | -4.397E-01 | -7.334E+00 | 2.602E+01 | -3.227E+01 | 1.617E+01 | -2.637E+00 | 4.180E-01 |
| 1000 | 15 | W | Kr | 1.29 | 1.275E+01 | -3.049E+01 | 2.744E+01 | -1.362E+01 | 4.690E+00 | -3.093E-01 | 1.559E+01 | -3.948E+01 | 3.866E+01 | -1.955E+01 | 5.514E+00 | -3.014E-01 |
| 1000 | 30 | W | Kr | 1.42 | 3.926E+01 | -1.090E+02 | 1.138E+02 | -5.711E+01 | 1.481E+01 | -1.164E+00 | 2.281E+01 | -5.850E+01 | 5.819E+01 | -2.890E+01 | 7.313E+00 | -3.576E-01 |
| 1000 | 45 | W | Kr | 1.46 | 3.063E+00 | 3.226E+00 | -1.830E+01 | 1.522E+01 | -2.825E+00 | 1.994E-01 | 1.226E+01 | -3.213E+01 | 3.410E+01 | -1.872E+01 | 5.289E+00 | -2.269E-01 |
| 1000 | 60 | W | Kr | 1.37 | 3.219E+01 | -8.483E+01 | 7.770E+01 | -2.864E+01 | 4.245E+00 | -8.981E-02 | -3.560E+00 | 1.505E+01 | -2.002E+01 | 1.102E+01 | -2.592E+00 | 6.691E-01 |
| 1500 | 0 | W | Kr | 1.47 | 1.306E+01 | -3.674E+01 | 4.050E+01 | -2.294E+01 | 7.058E+00 | -4.894E-01 | -1.272E+01 | 4.058E+01 | -4.652E+01 | 2.226E+01 | -3.709E+00 | 5.636E-01 |
| 1500 | 15 | W | Kr | 1.56 | 1.796E+01 | -4.437E+01 | 4.133E+01 | -2.010E+01 | 6.185E+00 | -4.103E-01 | 2.468E+01 | -6.454E+01 | 6.476E+01 | -3.230E+01 | 8.413E+00 | -4.414E-01 |
| 1500 | 30 | W | Kr | 1.72 | 4.913E+01 | -1.368E+02 | 1.438E+02 | -7.260E+01 | 1.870E+01 | -1.537E+00 | 4.242E+00 | -3.399E+00 | -2.321E+00 | 1.349E+00 | 5.955E-01 | 2.766E-01 |
| 1500 | 45 | W | Kr | 1.75 | 1.953E+00 | 7.211E+00 | -2.412E+01 | 1.966E+01 | -4.271E+00 | 2.859E-01 | -8.861E+00 | 2.567E+01 | -2.291E+01 | 5.625E+00 | 1.096E+00 | 1.307E-01 |
| 1500 | 60 | W | Kr | 1.57 | -9.341E+01 | 2.802E+02 | -3.150E+02 | 1.628E+02 | -3.745E+01 | 3.582E+00 | 9.783E+01 | -3.080E+02 | 3.632E+02 | -1.953E+02 | 4.665E+01 | -3.737E+00 |
| 500 | 0 | Mo | Kr | 0.63 | -5.025E+00 | 1.976E+01 | -2.688E+01 | 1.523E+01 | -3.444E+00 | 4.467E-01 | -8.858E+00 | 2.981E+01 | -3.671E+01 | 1.927E+01 | -3.929E+00 | 4.945E-01 |
| 500 | 15 | Mo | Kr | 0.75 | 6.500E+00 | -1.500E+01 | 1.252E+01 | -6.709E+00 | 2.974E+00 | -1.529E-01 | 6.182E+00 | -1.466E+01 | 1.332E+01 | -6.588E+00 | 1.915E+00 | -4.766E-02 |
| 500 | 30 | Mo | Kr | 1.01 | 2.923E-01 | 7.109E+00 | -1.739E+01 | 1.115E+01 | -1.268E+00 | 3.158E-01 | 1.926E+01 | -5.146E+01 | 5.254E+01 | -2.571E+01 | 5.933E+00 | -3.711E-01 |
| 500 | 45 | Mo | Kr | 1.26 | 1.308E+01 | -2.598E+01 | 1.351E+01 | -2.587E+00 | 2.416E+00 | -1.059E-01 | 3.300E+01 | -8.815E+01 | 8.754E+01 | -3.943E+01 | 7.682E+00 | -3.548E-01 |
| 500 | 60 | Mo | Kr | 1.00 | -7.699E+00 | 3.278E+01 | -5.122E+01 | 3.358E+01 | -7.822E+00 | 7.007E-01 | 3.300E+01 | -9.518E+01 | 1.043E+02 | -5.299E+01 | 1.206E+01 | -8.383E-01 |
| 750 | 0 | Mo | Kr | 0.97 | 1.503E+01 | -4.101E+01 | 4.320E+01 | -2.310E+01 | 6.530E+00 | -4.259E-01 | -7.959E+00 | 3.060E+01 | -4.075E+01 | 2.200E+01 | -4.189E+00 | 5.101E-01 |
| 750 | 15 | Mo | Kr | 1.11 | 2.799E+01 | -7.529E+01 | 7.603E+01 | -3.816E+01 | 1.037E+01 | -6.691E-01 | 1.074E+01 | -2.528E+01 | 2.301E+01 | -1.144E+01 | 3.395E+00 | -1.594E-01 |
| 750 | 30 | Mo | Kr | 1.42 | -2.644E+01 | 8.551E+01 | -1.027E+02 | 5.317E+01 | -1.027E+01 | 1.099E+00 | 2.247E+01 | -5.971E+01 | 6.154E+01 | -3.131E+01 | 7.920E+00 | -5.625E-01 |
| 750 | 45 | Mo | Kr | 1.67 | -1.425E-01 | 1.646E+01 | -3.562E+01 | 2.204E+01 | -2.369E+00 | 1.894E-01 | 3.303E+01 | -8.632E+01 | 8.539E+01 | -3.954E+01 | 8.358E+00 | -3.876E-01 |
| 750 | 60 | Mo | Kr | 1.51 | -5.875E+00 | 3.748E+01 | -7.017E+01 | 5.145E+01 | -1.355E+01 | 1.249E+00 | 3.478E+01 | -9.699E+01 | 1.035E+02 | -5.186E+01 | 1.192E+01 | -7.445E-01 |
| 1000 | 0 | Mo | Kr | 1.18 | 1.200E+01 | -3.244E+01 | 3.381E+01 | -1.821E+01 | 5.429E+00 | -3.239E-01 | -1.781E+01 | 5.880E+01 | -7.054E+01 | 3.623E+01 | -7.256E+00 | 8.500E-01 |
| 1000 | 15 | Mo | Kr | 1.29 | 1.638E+01 | -4.104E+01 | 3.897E+01 | -1.997E+01 | 6.450E+00 | -3.740E-01 | 1.465E+01 | -3.404E+01 | 3.015E+01 | -1.434E+01 | 4.230E+00 | -2.572E-01 |
| 1000 | 30 | Mo | Kr | 1.67 | 2.999E+01 | -7.585E+01 | 7.169E+01 | -3.484E+01 | 1.036E+01 | -6.919E-01 | 4.414E+01 | -1.158E+02 | 1.164E+02 | -5.663E+01 | 1.336E+01 | -8.594E-01 |
| 1000 | 45 | Mo | Kr | 1.87 | -1.521E+00 | 2.321E+01 | -4.605E+01 | 2.901E+01 | -4.231E+00 | 2.994E-01 | 3.662E+01 | -9.569E+01 | 9.495E+01 | -4.437E+01 | 9.656E+00 | -4.743E-01 |
| 1000 | 60 | Mo | Kr | 1.75 | -1.501E+01 | 6.626E+01 | -1.043E+02 | 7.060E+01 | -1.847E+01 | 1.679E+00 | 3.714E+01 | -1.047E+02 | 1.138E+02 | -5.872E+01 | 1.411E+01 | -9.108E-01 |
| 1500 | 0 | Mo | Kr | 1.19 | 8.132E+00 | -1.967E+01 | 1.741E+01 | -7.888E+00 | 2.443E+00 | -7.334E-02 | 6.249E+00 | -1.472E+01 | 1.231E+01 | -5.652E+00 | 2.125E+00 | 2.700E-02 |
| 1500 | 15 | Mo | Kr | 1.47 | 7.688E+00 | -1.762E+01 | 1.528E+01 | -8.557E+00 | 3.928E+00 | -1.879E-01 | 2.642E+01 | -6.632E+01 | 6.163E+01 | -2.707E+01 | 6.142E+00 | -3.043E-01 |
| 1500 | 30 | Mo | Kr | 2.01 | 1.849E+01 | -4.634E+01 | 4.538E+01 | -2.538E+01 | 9.325E+00 | -6.712E-01 | 4.998E+01 | -1.325E+02 | 1.354E+02 | -6.750E+01 | 1.651E+01 | -1.100E+00 |
| 1500 | 45 | Mo | Kr | 2.21 | -1.196E+01 | 5.294E+01 | -7.703E+01 | 4.394E+01 | -7.509E+00 | 5.412E-01 | 3.431E+01 | -8.895E+01 | 8.862E+01 | -4.250E+01 | 9.901E+00 | -4.714E-01 |
| 1500 | 60 | Mo | Kr | 2.15 | -1.062E+01 | 5.715E+01 | -9.950E+01 | 7.205E+01 | -2.000E+01 | 1.875E+00 | 2.535E+01 | -6.818E+01 | 7.159E+01 | -3.606E+01 | 8.397E+00 | -1.349E-01 |

| E (eV) | β ° | Target | Ion | Y (atoms/ion) | A6 | A5 | A4 | A3 | A2 | A1 | B6 | B5 | B4 | B3 | B2 | B1 |
|---|---|---|---|---|---|---|---|---|---|---|---|---|---|---|---|---|
| 500 | 0 | Mo | Ar | 0.56 | 0.000E+00 | 1.288E+00 | -2.632E+00 | 1.336E+00 | 2.257E-02 | 1.199E-01 | 0.000E+00 | 1.655E+00 | -3.545E+00 | 2.043E+00 | -1.114E-01 | 9.684E-02 |
| 500 | 15 | Mo | Ar | 0.68 | 0.000E+00 | -1.776E-01 | 1.572E+00 | -3.272E+00 | 2.099E+00 | -5.359E-02 | 0.000E+00 | 1.533E+00 | -2.841E+00 | 1.207E+00 | 2.333E-01 | 1.718E-02 |
| 500 | 30 | Mo | Ar | 0.81 | -8.962E+00 | 2.622E+01 | -2.809E+01 | 1.213E+01 | -1.409E+00 | 3.094E-01 | 0.000E+00 | 2.082E+00 | -4.042E+00 | 2.308E+00 | -2.548E-01 | 7.418E-02 |
| 500 | 45 | Mo | Ar | 0.93 | -1.109E+01 | 3.353E+01 | -3.631E+01 | 1.481E+01 | -7.887E-01 | 9.403E-02 | 0.000E+00 | 1.656E+00 | -2.537E+00 | 7.969E-01 | 2.482E-01 | 3.488E-02 |
| 500 | 60 | Mo | Ar | 0.77 | -1.071E+01 | 3.463E+01 | -4.257E+01 | 2.262E+01 | -4.028E+00 | 2.719E-01 | 0.000E+00 | 1.713E+00 | -3.134E+00 | 1.791E+00 | -3.175E-01 | 1.319E-01 |
| 750 | 0 | Mo | Ar | 0.75 | 0.000E+00 | 1.073E+00 | -1.856E+00 | 4.112E-01 | 4.664E-01 | 1.028E-01 | 0.000E+00 | 1.759E+00 | -3.631E+00 | 1.863E+00 | 9.967E-02 | 1.086E-01 |
| 750 | 15 | Mo | Ar | 0.87 | 0.000E+00 | -3.355E-01 | 2.122E+00 | -3.893E+00 | 2.399E+00 | -4.433E-02 | 0.000E+00 | 2.172E+00 | -3.727E+00 | 1.253E+00 | 5.280E-01 | -2.156E-03 |
| 750 | 30 | Mo | Ar | 1.01 | -6.692E+00 | 1.863E+01 | -1.838E+01 | 6.313E+00 | 2.926E-01 | 1.456E-01 | 0.000E+00 | 3.206E+00 | -6.244E+00 | 3.710E+00 | -5.488E-01 | 1.429E-01 |
| 750 | 45 | Mo | Ar | 1.07 | -1.323E+01 | 4.098E+01 | -4.651E+01 | 2.177E+01 | -2.944E+00 | 2.690E-01 | 0.000E+00 | 1.812E+00 | -2.501E+00 | 3.386E-01 | 6.329E-01 | 1.391E-02 |
| 750 | 60 | Mo | Ar | 0.92 | -2.156E+01 | 7.506E+01 | -1.005E+02 | 6.206E+01 | -1.630E+01 | 1.538E+00 | 0.000E+00 | 1.897E+00 | -3.098E+00 | 1.287E+00 | 3.009E-02 | 1.621E-01 |
| 1000 | 0 | Mo | Ar | 0.80 | 0.000E+00 | 7.994E-01 | -1.443E+00 | 2.263E-01 | 5.563E-01 | 7.594E-02 | 0.000E+00 | 8.683E-01 | -1.642E+00 | 3.260E-01 | 6.022E-01 | 6.043E-02 |
| 1000 | 15 | Mo | Ar | 0.94 | 0.000E+00 | -1.005E+00 | 3.768E+00 | -5.321E+00 | 2.970E+00 | -1.318E-01 | 0.000E+00 | 1.992E+00 | -3.392E+00 | 1.082E+00 | 5.421E-01 | 2.689E-02 |
| 1000 | 30 | Mo | Ar | 1.05 | -1.150E+01 | 3.262E+01 | -3.302E+01 | 1.277E+01 | -6.441E-01 | 9.774E-02 | 0.000E+00 | 2.382E+00 | -3.889E+00 | 1.313E+00 | 4.608E-01 | 3.044E-02 |
| 1000 | 45 | Mo | Ar | 1.14 | -8.713E+00 | 2.767E+01 | -3.192E+01 | 1.457E+01 | -1.320E+00 | 1.075E-01 | 0.000E+00 | 1.476E+00 | -1.741E+00 | -1.662E-01 | 7.334E-01 | 4.789E-02 |
| 1000 | 60 | Mo | Ar | 0.97 | -1.133E+01 | 4.197E+01 | -6.015E+01 | 3.959E+01 | -1.082E+01 | 1.080E+00 | 0.000E+00 | 1.793E+00 | -3.047E+00 | 1.322E+00 | 1.951E-02 | 2.168E-01 |
| 1500 | 0 | Mo | Ar | 0.92 | 0.000E+00 | -1.452E+00 | 3.796E+00 | -3.992E+00 | 1.888E+00 | -1.459E-03 | 0.000E+00 | 8.425E-02 | 3.934E-01 | -1.543E+00 | 1.349E+00 | -2.469E-02 |
| 1500 | 15 | Mo | Ar | 1.06 | 0.000E+00 | -1.399E+00 | 4.581E+00 | -5.782E+00 | 2.979E+00 | -5.366E-02 | 0.000E+00 | 1.804E+00 | -3.105E+00 | 9.043E-01 | 6.707E-01 | 1.131E-02 |
| 1500 | 30 | Mo | Ar | 1.13 | -4.576E+00 | 1.055E+01 | -5.840E+00 | -3.255E+00 | 3.864E+00 | -3.699E-01 | 0.000E+00 | 4.686E+00 | -9.479E+00 | 5.966E+00 | -1.017E+00 | 1.934E-01 |
| 1500 | 45 | Mo | Ar | 1.20 | -4.207E+00 | 1.326E+01 | -1.394E+01 | 3.730E+00 | 1.890E+00 | -3.072E-01 | 0.000E+00 | 7.591E-01 | -9.618E-03 | -1.802E+00 | 1.482E+00 | -3.026E-02 |
| 1500 | 60 | Mo | Ar | 1.07 | 1.219E+01 | -3.108E+01 | 2.416E+01 | -4.363E+00 | -8.211E-01 | 2.963E-01 | 0.000E+00 | 1.468E+00 | -2.682E+00 | 1.531E+00 | -3.012E-01 | 3.472E-01 |
| 500 | 0 | Mo | Xe | 0.44 | 1.950E+00 | -4.833E+00 | 4.486E+00 | -2.455E+00 | 8.638E-01 | 4.444E-02 | 4.709E-01 | -3.232E-01 | -6.052E-01 | -3.311E-03 | 4.538E-01 | 6.405E-02 |
| 500 | 15 | Mo | Xe | 0.58 | -2.636E-01 | 1.291E+00 | -7.020E-01 | -2.372E+00 | 2.198E+00 | -6.454E-02 | 4.348E+00 | -1.097E+01 | 1.065E+01 | -5.404E+00 | 1.539E+00 | -8.864E-02 |
| 500 | 30 | Mo | Xe | 0.93 | -2.172E+01 | 6.951E+01 | -8.244E+01 | 4.175E+01 | -7.904E+00 | 9.483E-01 | 1.708E+01 | -4.719E+01 | 4.943E+01 | -2.445E+01 | 5.669E+00 | -4.241E-01 |
| 500 | 45 | Mo | Xe | 1.18 | 8.810E-01 | 5.443E+00 | -1.575E+01 | 9.647E+00 | -9.676E-02 | 1.469E-01 | 3.225E+01 | -8.609E+01 | 8.501E+01 | -3.787E+01 | 7.324E+00 | -3.952E-01 |
| 500 | 60 | Mo | Xe | 0.87 | -4.114E+00 | 1.110E+01 | -1.122E+01 | 2.931E+00 | 1.945E+00 | -3.322E-01 | 4.011E+01 | -1.163E+02 | 1.280E+02 | -6.544E+01 | 1.515E+01 | -1.166E+00 |
| 750 | 0 | Mo | Xe | 0.78 | 4.194E+00 | -8.863E+00 | 6.375E+00 | -2.672E+00 | 1.023E+00 | 1.028E-01 | 7.239E+00 | -1.774E+01 | 1.603E+01 | -7.838E+00 | 2.604E+00 | -1.318E-01 |
| 750 | 15 | Mo | Xe | 1.16 | -2.288E+01 | 6.786E+01 | -7.472E+01 | 3.784E+01 | -1.008E+01 | 2.176E+00 | 5.272E+00 | -1.298E+01 | 1.261E+01 | -6.950E+00 | 2.355E+00 | -1.481E-01 |
| 750 | 30 | Mo | Xe | 1.51 | -3.703E+01 | 1.219E+02 | -1.483E+02 | 7.821E+01 | -1.625E+01 | 1.820E+00 | 3.398E+01 | -9.304E+01 | 9.715E+01 | -4.836E+01 | 1.147E+01 | -8.835E-01 |
| 750 | 45 | Mo | Xe | 1.91 | -4.661E+00 | 3.113E+01 | -5.405E+01 | 3.219E+01 | -4.675E+00 | 6.326E-01 | 5.354E+01 | -1.424E+02 | 1.411E+02 | -6.377E+01 | 1.286E+01 | -7.495E-01 |
| 750 | 60 | Mo | Xe | 1.52 | -2.708E+01 | 9.619E+01 | -1.312E+02 | 8.160E+01 | -2.102E+01 | 2.083E+00 | 5.403E+01 | -1.553E+02 | 1.703E+02 | -8.740E+01 | 2.049E+01 | -1.496E+00 |
| 1000 | 0 | Mo | Xe | 1.11 | -6.441E-01 | 7.248E+00 | -1.267E+01 | 6.933E+00 | -9.362E-01 | 3.491E-01 | 4.790E+00 | -7.530E+00 | 2.057E+00 | -1.656E-01 | 1.116E+00 | 1.118E-02 |
| 1000 | 15 | Mo | Xe | 1.29 | -5.631E+00 | 2.207E+01 | -2.805E+01 | 1.200E+01 | -2.199E-01 | 1.949E-01 | 1.401E+01 | -3.272E+01 | 2.868E+01 | -1.300E+01 | 3.590E+00 | -2.142E-01 |
| 1000 | 30 | Mo | Xe | 1.79 | -2.275E+01 | 7.709E+01 | -9.464E+01 | 4.825E+01 | -8.636E+00 | 1.216E+00 | 5.242E+01 | -1.450E+02 | 1.533E+02 | -7.723E+01 | 1.851E+01 | -1.448E+00 |
| 1000 | 45 | Mo | Xe | 2.20 | -1.427E+01 | 5.896E+01 | -8.362E+01 | 4.614E+01 | -7.220E+00 | 7.426E-01 | 5.390E+01 | -1.428E+02 | 1.419E+02 | -6.503E+01 | 1.353E+01 | -7.752E-01 |
| 1000 | 60 | Mo | Xe | 1.93 | -4.098E+01 | 1.393E+02 | -1.800E+02 | 1.050E+02 | -2.460E+01 | 2.045E+00 | 4.209E+01 | -1.193E+02 | 1.305E+02 | -6.762E+01 | 1.629E+01 | -1.155E+00 |
| 1500 | 0 | Mo | Xe | 1.54 | 2.096E+00 | 2.436E-01 | -5.135E+00 | 2.250E+00 | 8.472E-01 | 1.591E-01 | 3.959E+00 | -4.067E+00 | -1.854E+00 | 8.900E-01 | 1.509E+00 | 2.013E-02 |
| 1500 | 15 | Mo | Xe | 1.78 | -7.314E+00 | 2.854E+01 | -3.578E+01 | 1.534E+01 | -4.431E-01 | 2.599E-01 | 2.098E+01 | -4.945E+01 | 4.406E+01 | -2.018E+01 | 5.478E+00 | -3.114E-01 |
| 1500 | 30 | Mo | Xe | 2.26 | -1.584E+01 | 5.562E+01 | -6.759E+01 | 3.146E+01 | -3.504E+00 | 7.022E-01 | 5.991E+01 | -1.603E+02 | 1.642E+02 | -8.103E+01 | 1.953E+01 | -1.495E+00 |
| 1500 | 45 | Mo | Xe | 2.62 | -1.374E+01 | 5.837E+01 | -8.232E+01 | 4.384E+01 | -5.468E+00 | 3.340E-01 | 5.846E+01 | -1.540E+02 | 1.532E+02 | -7.135E+01 | 1.547E+01 | -8.660E-01 |
| 1500 | 60 | Mo | Xe | 2.54 | -5.716E+01 | 2.002E+02 | -2.672E+02 | 1.638E+02 | -4.263E+01 | 4.033E+00 | 3.848E+01 | -1.073E+02 | 1.166E+02 | -6.057E+01 | 1.471E+01 | -8.290E-01 |

| E (eV) | β ° | Target | Ion | Y (atoms/ion) | A6 | A5 | A4 | A3 | A2 | A1 | B6 | B5 | B4 | B3 | B2 | B1 |
|---|---|---|---|---|---|---|---|---|---|---|---|---|---|---|---|---|
| 150 | 0 | Ta | Xe | 0.05 | -4.795E-01 | 1.155E+00 | -7.751E-01 | -2.819E-02 | 1.097E-01 | 1.972E-02 | -1.248E+00 | 3.871E+00 | -4.396E+00 | 2.194E+00 | -4.926E-01 | 7.343E-02 |
| 200 | 0 | Ta | Xe | 0.14 | -1.035E+00 | 3.020E+00 | -2.804E+00 | 7.250E-01 | 1.805E-02 | 8.056E-02 | -1.008E+00 | 2.573E+00 | -1.666E+00 | -3.911E-01 | 4.797E-01 | 1.677E-02 |
| 300 | 0 | Ta | Xe | 0.36 | -6.179E-01 | 1.504E+00 | 1.232E-01 | -2.389E+00 | 1.445E+00 | -3.391E-02 | -4.145E+00 | 1.276E+01 | -1.327E+01 | 4.833E+00 | -2.668E-01 | 1.197E-01 |
| 300 | 15 | Ta | Xe | 0.47 | -1.244E+01 | 3.578E+01 | -3.491E+01 | 1.167E+01 | -1.164E-01 | 6.812E-02 | 9.935E-01 | -2.337E+00 | 3.156E+00 | -3.003E+00 | 1.328E+00 | -8.617E-02 |
| 300 | 30 | Ta | Xe | 0.63 | -3.217E+01 | 9.859E+01 | -1.101E+02 | 5.259E+01 | -9.717E+00 | 9.245E-01 | 1.045E+01 | -2.942E+01 | 3.193E+01 | -1.662E+01 | 3.996E+00 | -2.614E-01 |
| 300 | 45 | Ta | Xe | 0.66 | -1.061E+01 | 3.260E+01 | -3.537E+01 | 1.436E+01 | -1.007E+00 | 1.796E-01 | 1.832E+01 | -4.926E+01 | 4.944E+01 | -2.273E+01 | 4.626E+00 | -2.664E-01 |
| 300 | 60 | Ta | Xe | 0.48 | -6.418E+00 | 1.944E+01 | -2.110E+01 | 8.760E+00 | -5.550E-01 | 4.311E-02 | 1.800E+01 | -5.235E+01 | 5.785E+01 | -2.967E+01 | 6.803E+00 | -4.892E-01 |
| 400 | 0 | Ta | Xe | 0.57 | -3.452E+00 | 1.140E+01 | -1.211E+01 | 3.990E+00 | 1.083E-01 | 1.464E-01 | -7.496E+00 | 2.361E+01 | -2.565E+01 | 1.055E+01 | -1.119E+00 | 1.826E-01 |
| 500 | 0 | Ta | Xe | 0.69 | -3.298E+00 | 1.174E+01 | -1.321E+01 | 4.694E+00 | 4.791E-02 | 1.504E-01 | -4.149E+00 | 1.434E+01 | -1.593E+01 | 5.663E+00 | 7.041E-02 | 1.209E-01 |
| 500 | 15 | Ta | Xe | 0.64 | -1.069E+00 | 3.985E+00 | -4.055E+00 | -4.476E-01 | 1.796E+00 | -8.990E-02 | 8.166E+00 | -2.134E+01 | 2.152E+01 | -1.089E+01 | 2.761E+00 | -1.002E-01 |
| 500 | 30 | Ta | Xe | 0.79 | -1.700E+01 | 4.986E+01 | -5.276E+01 | 2.239E+01 | -2.689E+00 | 3.531E-01 | 1.750E+01 | -4.652E+01 | 4.626E+01 | -2.111E+01 | 4.115E+00 | -1.024E-01 |
| 500 | 45 | Ta | Xe | 0.86 | -1.030E+01 | 3.441E+01 | -4.131E+01 | 1.954E+01 | -2.216E+00 | 1.493E-01 | 2.608E+01 | -6.951E+01 | 6.907E+01 | -3.131E+01 | 6.204E+00 | -2.920E-01 |
| 500 | 60 | Ta | Xe | 0.67 | -5.025E+00 | 1.633E+01 | -1.881E+01 | 7.942E+00 | -2.576E-02 | -1.222E-01 | 2.024E+01 | -5.718E+01 | 6.201E+01 | -3.166E+01 | 7.361E+00 | -4.918E-01 |
| 750 | 0 | Ta | Xe | 0.92 | -7.306E+00 | 2.715E+01 | -3.481E+01 | 1.824E+01 | -3.514E+00 | 4.749E-01 | -1.819E+00 | 1.049E+01 | -1.565E+01 | 7.942E+00 | -1.006E+00 | 2.742E-01 |
| 750 | 15 | Ta | Xe | 1.04 | -7.239E+00 | 2.348E+01 | -2.500E+01 | 8.053E+00 | 1.078E+00 | -5.426E-02 | 1.134E+01 | -2.761E+01 | 2.655E+01 | -1.369E+01 | 3.923E+00 | -2.157E-01 |
| 750 | 30 | Ta | Xe | 1.25 | -2.749E+01 | 8.682E+01 | -1.005E+02 | 4.986E+01 | -9.096E+00 | 8.510E-01 | 3.140E+01 | -8.690E+01 | 9.321E+01 | -4.846E+01 | 1.192E+01 | -8.064E-01 |
| 750 | 45 | Ta | Xe | 1.32 | -3.034E+01 | 9.831E+01 | -1.158E+02 | 5.751E+01 | -9.718E+00 | 5.639E-01 | 4.381E+01 | -1.158E+02 | 1.144E+02 | -5.221E+01 | 1.082E+01 | -5.938E-01 |
| 750 | 60 | Ta | Xe | 1.10 | -2.520E-01 | 8.334E+00 | -1.637E+01 | 8.294E+00 | 1.196E+00 | -6.652E-01 | 3.444E+01 | -9.647E+01 | 1.031E+02 | -5.131E+01 | 1.132E+01 | -5.512E-01 |
| 1000 | 0 | Ta | Xe | 1.11 | -6.225E+00 | 2.342E+01 | -2.940E+01 | 1.425E+01 | -1.980E+00 | 2.731E-01 | -9.523E+00 | 3.547E+01 | -4.590E+01 | 2.477E+01 | -5.136E+00 | 6.595E-01 |
| 1000 | 15 | Ta | Xe | 1.26 | -6.751E+00 | 2.299E+01 | -2.521E+01 | 8.353E+00 | 1.112E+00 | -5.002E-02 | 1.389E+01 | -3.436E+01 | 3.391E+01 | -1.788E+01 | 5.140E+00 | -2.827E-01 |
| 1000 | 30 | Ta | Xe | 1.54 | -4.840E+01 | 1.496E+02 | -1.699E+02 | 8.401E+01 | -1.622E+01 | 1.405E+00 | 3.932E+01 | -1.057E+02 | 1.089E+02 | -5.377E+01 | 1.260E+01 | -8.009E-01 |
| 1000 | 45 | Ta | Xe | 1.66 | -2.836E+01 | 9.678E+01 | -1.201E+02 | 6.320E+01 | -1.151E+01 | 6.882E-01 | 3.748E+01 | -9.657E+01 | 9.346E+01 | -4.201E+01 | 8.617E+00 | -3.210E-01 |
| 1000 | 60 | Ta | Xe | 1.44 | -1.486E+01 | 4.934E+01 | -6.185E+01 | 3.475E+01 | -7.559E+00 | 7.846E-01 | 2.191E+01 | -6.214E+01 | 6.941E+01 | -3.753E+01 | 9.443E+00 | -5.004E-01 |
| 1500 | 0 | Ta | Xe | 1.46 | -9.641E+00 | 3.221E+01 | -3.819E+01 | 1.860E+01 | -2.893E+00 | 3.785E-01 | -4.240E+00 | 1.828E+01 | -2.506E+01 | 1.309E+01 | -2.020E+00 | 4.237E-01 |
| 1500 | 15 | Ta | Xe | 1.66 | -1.194E+01 | 3.642E+01 | -3.700E+01 | 1.210E+01 | 1.119E+00 | -5.459E-02 | 2.210E+01 | -5.512E+01 | 5.281E+01 | -2.540E+01 | 6.584E+00 | -3.679E-01 |
| 1500 | 30 | Ta | Xe | 2.02 | -3.585E+01 | 1.112E+02 | -1.248E+02 | 5.897E+01 | -9.466E+00 | 7.433E-01 | 4.596E+01 | -1.242E+02 | 1.304E+02 | -6.703E+01 | 1.682E+01 | -1.152E+00 |
| 1500 | 45 | Ta | Xe | 2.18 | -5.006E+01 | 1.554E+02 | -1.761E+02 | 8.500E+01 | -1.409E+01 | 7.141E-01 | 5.007E+01 | -1.339E+02 | 1.367E+02 | -6.604E+01 | 1.503E+01 | -8.439E-01 |
| 1500 | 60 | Ta | Xe | 2.09 | -1.624E+01 | 6.285E+01 | -8.987E+01 | 5.747E+01 | -1.473E+01 | 1.474E+00 | 4.051E+01 | -1.231E+02 | 1.487E+02 | -8.782E+01 | 2.463E+01 | -1.939E+00 |
| 500 | 0 | Ta | Ar | 0.43 | -2.486E+00 | 8.413E+00 | -9.773E+00 | 4.411E+00 | -5.711E-01 | 1.431E-01 | 5.502E+00 | -1.479E+01 | 1.531E+01 | -7.909E+00 | 2.132E+00 | -1.095E-01 |
| 500 | 15 | Ta | Ar | 0.51 | -4.244E+00 | 1.249E+01 | -1.204E+01 | 3.396E+00 | 6.009E-01 | -3.691E-02 | 4.629E+00 | -1.136E+01 | 1.085E+01 | -5.494E+00 | 1.587E+00 | -5.633E-02 |
| 500 | 30 | Ta | Ar | 0.62 | -9.069E+00 | 2.855E+01 | -3.227E+01 | 1.515E+01 | -2.506E+00 | 3.472E-01 | 6.840E+00 | -1.733E+01 | 1.701E+01 | -8.419E+00 | 2.193E+00 | -1.003E-01 |
| 500 | 45 | Ta | Ar | 0.68 | -8.581E+00 | 2.668E+01 | -2.862E+01 | 1.127E+01 | -5.775E-01 | 4.629E-02 | 7.966E+00 | -2.092E+01 | 2.131E+01 | -1.068E+01 | 2.606E+00 | -8.003E-02 |
| 500 | 60 | Ta | Ar | 0.59 | -2.146E+01 | 7.365E+01 | -9.475E+01 | 5.527E+01 | -1.380E+01 | 1.279E+00 | 3.209E+00 | -8.472E+00 | 9.452E+00 | -5.711E+00 | 1.714E+00 | -1.593E-02 |
| 750 | 0 | Ta | Ar | 0.62 | -4.904E+00 | 1.548E+01 | -1.708E+01 | 7.482E+00 | -9.272E-01 | 1.563E-01 | 2.488E+00 | -4.868E+00 | 3.532E+00 | -1.803E+00 | 8.088E-01 | 4.912E-02 |
| 750 | 15 | Ta | Ar | 0.71 | -5.198E+00 | 1.568E+01 | -1.527E+01 | 4.294E+00 | 8.042E-01 | -4.671E-02 | 5.475E+00 | -1.258E+01 | 1.133E+01 | -5.753E+00 | 1.870E+00 | -8.810E-02 |
| 750 | 30 | Ta | Ar | 0.85 | -1.312E+01 | 4.164E+01 | -4.700E+01 | 2.194E+01 | -3.516E+00 | 3.753E-01 | 7.313E+00 | -1.781E+01 | 1.760E+01 | -9.505E+00 | 2.804E+00 | -9.890E-02 |
| 750 | 45 | Ta | Ar | 0.86 | -1.465E+01 | 4.616E+01 | -5.133E+01 | 2.288E+01 | -2.925E+00 | 1.819E-01 | 1.250E+01 | -3.222E+01 | 3.191E+01 | -1.548E+01 | 3.741E+00 | -1.429E-01 |
| 750 | 60 | Ta | Ar | 0.82 | -2.592E+01 | 9.021E+01 | -1.173E+02 | 6.924E+01 | -1.765E+01 | 1.687E+00 | 7.780E+00 | -2.153E+01 | 2.401E+01 | -1.353E+01 | 3.606E+00 | -5.756E-02 |
| 1000 | 0 | Ta | Ar | 0.67 | -3.100E+00 | 1.004E+01 | -1.026E+01 | 3.135E+00 | 4.044E-01 | 2.930E-02 | 2.635E+00 | -4.652E+00 | 2.989E+00 | -1.725E+00 | 9.841E-01 | 1.304E-02 |
| 1000 | 15 | Ta | Ar | 0.81 | -1.163E+01 | 3.569E+01 | -3.806E+01 | 1.580E+01 | -1.590E+00 | 1.084E-01 | 4.933E+00 | -9.197E+00 | 5.814E+00 | -2.237E+00 | 9.592E-01 | 2.669E-02 |
| 1000 | 30 | Ta | Ar | 0.99 | -1.526E+01 | 4.828E+01 | -5.407E+01 | 2.502E+01 | -4.028E+00 | 4.532E-01 | 1.930E+01 | -5.299E+01 | 5.715E+01 | -3.066E+01 | 8.159E+00 | -5.735E-01 |
| 1000 | 45 | Ta | Ar | 0.99 | -1.420E+01 | 4.620E+01 | -5.293E+01 | 2.449E+01 | -3.366E+00 | 1.992E-01 | 1.464E+01 | -3.807E+01 | 3.826E+01 | -1.896E+01 | 4.680E+00 | -1.721E-01 |
| 1000 | 60 | Ta | Ar | 0.95 | -1.805E+01 | 6.338E+01 | -8.291E+01 | 4.886E+01 | -1.215E+01 | 1.191E+00 | 3.812E+00 | -8.530E+00 | 8.340E+00 | -5.219E+00 | 1.839E+00 | 7.534E-02 |
| 1500 | 0 | Ta | Ar | 0.82 | -6.722E+00 | 2.055E+01 | -2.135E+01 | 8.231E+00 | -5.156E-01 | 1.025E-01 | 2.164E-01 | 2.687E+00 | -5.057E+00 | 2.115E+00 | 2.066E-01 | 1.286E-01 |
| 1500 | 15 | Ta | Ar | 1.02 | -3.922E+00 | 1.347E+01 | -1.405E+01 | 3.927E+00 | 9.770E-01 | 2.100E-03 | -5.265E+00 | 1.970E+01 | -2.402E+01 | 1.140E+01 | -1.670E+00 | 2.424E-01 |
| 1500 | 30 | Ta | Ar | 1.25 | -6.954E+00 | 2.404E+01 | -2.701E+01 | 1.059E+01 | -2.134E-01 | 5.634E-02 | 1.176E+01 | -2.958E+01 | 3.037E+01 | -1.682E+01 | 4.949E+00 | -1.734E-01 |
| 1500 | 45 | Ta | Ar | 1.22 | -2.070E+01 | 6.809E+01 | -8.037E+01 | 4.024E+01 | -7.284E+00 | 5.177E-01 | 1.067E+01 | -2.847E+01 | 3.132E+01 | -1.825E+01 | 5.484E+00 | -2.494E-01 |
| 1500 | 60 | Ta | Ar | 1.23 | 1.540E+01 | -3.856E+01 | 3.374E+01 | -1.237E+01 | 2.230E+00 | 1.813E-02 | -6.315E+00 | 2.042E+01 | -2.192E+01 | 8.953E+00 | -1.202E+00 | 5.112E-01 |

| E (eV) | β ° | Target | Ion | Y (atoms/ion) | A6 | A5 | A4 | A3 | A2 | A1 | B6 | B5 | B4 | B3 | B2 | B1 |
|---|---|---|---|---|---|---|---|---|---|---|---|---|---|---|---|---|
| 500 | 0 | Ta | Kr | 0.58 | -2.199E+00 | 1.072E+01 | -1.651E+01 | 1.021E+01 | -2.435E+00 | 3.620E-01 | 5.969E+00 | -1.673E+01 | 1.839E+01 | -1.030E+01 | 2.892E+00 | -7.766E-02 |
| 500 | 15 | Ta | Kr | 0.67 | -6.870E+00 | 1.978E+01 | -1.919E+01 | 5.746E+00 | 7.392E-01 | -4.325E-02 | 4.224E+00 | -9.386E+00 | 8.013E+00 | -3.918E+00 | 1.204E+00 | 2.096E-02 |
| 500 | 30 | Ta | Kr | 0.75 | -2.017E+01 | 6.103E+01 | -6.786E+01 | 3.247E+01 | -5.921E+00 | 6.318E-01 | 1.638E+01 | -4.627E+01 | 4.997E+01 | -2.571E+01 | 6.224E+00 | -4.202E-01 |
| 500 | 45 | Ta | Kr | 0.84 | -1.181E+01 | 3.641E+01 | -3.945E+01 | 1.594E+01 | -8.571E-01 | 1.950E-02 | 1.732E+01 | -4.559E+01 | 4.487E+01 | -2.046E+01 | 4.277E+00 | -1.810E-01 |
| 500 | 60 | Ta | Kr | 0.67 | 1.252E+00 | 3.307E+00 | -1.474E+01 | 1.496E+01 | -5.350E+00 | 8.135E-01 | 1.787E+01 | -5.083E+01 | 5.521E+01 | -2.818E+01 | 6.528E+00 | -3.689E-01 |
| 750 | 0 | Ta | Kr | 0.88 | -1.243E+01 | 3.757E+01 | -4.016E+01 | 1.739E+01 | -2.452E+00 | 3.329E-01 | 5.922E+00 | -1.502E+01 | 1.519E+01 | -8.560E+00 | 2.811E+00 | -9.259E-02 |
| 750 | 15 | Ta | Kr | 1.02 | -1.085E+01 | 3.337E+01 | -3.514E+01 | 1.335E+01 | -4.882E-01 | 9.153E-02 | 1.027E+01 | -2.518E+01 | 2.428E+01 | -1.245E+01 | 3.520E+00 | -1.331E-01 |
| 750 | 30 | Ta | Kr | 1.15 | -2.399E+01 | 7.266E+01 | -7.943E+01 | 3.611E+01 | -5.412E+00 | 4.580E-01 | 1.850E+01 | -4.858E+01 | 4.962E+01 | -2.519E+01 | 6.375E+00 | -3.578E-01 |
| 750 | 45 | Ta | Kr | 1.19 | -3.055E+01 | 9.653E+01 | -1.111E+02 | 5.444E+01 | -9.468E+00 | 6.032E-01 | 2.512E+01 | -6.505E+01 | 6.338E+01 | -2.896E+01 | 6.175E+00 | -2.365E-01 |
| 750 | 60 | Ta | Kr | 1.14 | -9.523E+00 | 3.525E+01 | -4.797E+01 | 2.833E+01 | -6.188E+00 | 5.640E-01 | 2.632E+01 | -7.648E+01 | 8.630E+01 | -4.665E+01 | 1.161E+01 | -6.799E-01 |
| 1000 | 0 | Ta | Kr | 1.06 | -1.385E+01 | 4.247E+01 | -4.606E+01 | 2.029E+01 | -2.886E+00 | 3.554E-01 | 8.326E-01 | 1.392E+00 | -3.715E+00 | 9.972E-01 | 6.193E-01 | 1.958E-01 |
| 1000 | 15 | Ta | Kr | 1.20 | -1.088E+01 | 3.320E+01 | -3.345E+01 | 1.068E+01 | 9.584E-01 | -8.464E-02 | 1.519E+01 | -3.769E+01 | 3.617E+01 | -1.782E+01 | 4.801E+00 | -2.469E-01 |
| 1000 | 30 | Ta | Kr | 1.42 | -2.296E+01 | 7.129E+01 | -7.972E+01 | 3.728E+01 | -5.854E+00 | 5.217E-01 | 4.001E+01 | -1.090E+02 | 1.144E+02 | -5.815E+01 | 1.420E+01 | -9.194E-01 |
| 1000 | 45 | Ta | Kr | 1.42 | -2.659E+01 | 8.736E+01 | -1.033E+02 | 5.127E+01 | -8.618E+00 | 4.640E-01 | 2.216E+01 | -5.702E+01 | 5.636E+01 | -2.700E+01 | 6.253E+00 | -1.922E-01 |
| 1000 | 60 | Ta | Kr | 1.44 | -7.771E+00 | 3.172E+01 | -4.698E+01 | 3.041E+01 | -7.599E+00 | 8.019E-01 | 2.816E+01 | -7.587E+01 | 7.771E+01 | -3.751E+01 | 8.233E+00 | -1.604E-01 |
| 1500 | 0 | Ta | Kr | 1.33 | -1.079E+01 | 3.309E+01 | -3.464E+01 | 1.349E+01 | -9.095E-01 | 2.158E-01 | 8.961E+00 | -2.147E+01 | 2.114E+01 | -1.219E+01 | 4.120E+00 | -1.050E-01 |
| 1500 | 15 | Ta | Kr | 1.55 | -2.102E+01 | 6.111E+01 | -6.075E+01 | 2.189E+01 | -6.323E-01 | 2.320E-02 | 1.901E+01 | -4.660E+01 | 4.409E+01 | -2.139E+01 | 5.781E+00 | -3.114E-01 |
| 1500 | 30 | Ta | Kr | 1.84 | -3.013E+01 | 9.340E+01 | -1.039E+02 | 4.835E+01 | -7.597E+00 | 6.099E-01 | 3.239E+01 | -8.782E+01 | 9.406E+01 | -5.041E+01 | 1.334E+01 | -8.165E-01 |
| 1500 | 45 | Ta | Kr | 1.82 | -3.642E+01 | 1.179E+02 | -1.386E+02 | 6.989E+01 | -1.278E+01 | 7.996E-01 | 2.478E+01 | -6.490E+01 | 6.633E+01 | -3.357E+01 | 8.451E+00 | -3.398E-01 |
| 1500 | 60 | Ta | Kr | 1.79 | -4.370E+00 | 2.257E+01 | -3.807E+01 | 2.674E+01 | -6.886E+00 | 7.466E-01 | 1.043E+01 | -2.374E+01 | 2.200E+01 | -1.150E+01 | 3.214E+00 | 3.077E-01 |

## Appendix B:

## Table of Modified Zhang Fit Parameters to Experimental Data

## Eqn. 5.1

| Ion | Target | Energy (eV) | Phi (º) | Beta (º) | Y* (atoms/ion) | E* (eV) |
|---|---|---|---|---|---|---|
| Xe | Mo | 1500 | 0 | 0 | 1.59 | 185 |
| Xe | Mo | 1500 | 0 | 15 | 2.02 | 334 |
| Xe | Mo | 1500 | 0 | 30 | 2.68 | 363 |
| Xe | Mo | 1500 | 0 | 45 | 3.06 | 331 |
| Xe | Mo | 1500 | 0 | 60 | 3.09 | 152 |
| Xe | Mo | 1000 | 0 | 0 | 1.15 | 233 |
| Xe | Mo | 1000 | 0 | 15 | 1.46 | 328 |
| Xe | Mo | 1000 | 0 | 30 | 2.04 | 361 |
| Xe | Mo | 1000 | 0 | 45 | 2.44 | 357 |
| Xe | Mo | 1000 | 0 | 60 | 2.33 | 201 |
| Xe | Mo | 750 | 0 | 0 | 0.81 | 221 |
| Xe | Mo | 750 | 0 | 15 | 1.18 | 351 |
| Xe | Mo | 750 | 0 | 30 | 1.67 | 335 |
| Xe | Mo | 750 | 0 | 45 | 2.03 | 339 |
| Xe | Mo | 750 | 0 | 60 | 1.81 | 190 |
| Xe | Mo | 500 | 0 | 0 | 0.47 | 197 |
| Xe | Mo | 500 | 0 | 15 | 0.65 | 235 |
| Xe | Mo | 500 | 0 | 30 | 0.98 | 270 |
| Xe | Mo | 500 | 0 | 45 | 1.20 | 275 |
| Xe | Mo | 500 | 0 | 60 | 1.02 | 208 |
| Kr | W | 1500 | 0 | 0 | 1.51 | 48 |
| Kr | W | 1500 | 0 | 15 | 1.66 | 43 |
| Kr | W | 1500 | 0 | 30 | 1.98 | 11 |
| Kr | W | 1500 | 0 | 45 | 2.04 | 1 |
| Kr | W | 1500 | 0 | 60 | 1.98 | 129 |
| Kr | W | 1000 | 0 | 0 | 1.24 | 62 |
| Kr | W | 1000 | 0 | 15 | 1.39 | 96 |
| Kr | W | 1000 | 0 | 30 | 1.62 | 75 |
| Kr | W | 1000 | 0 | 45 | 1.68 | 62 |
| Kr | W | 1000 | 0 | 60 | 1.40 | 21 |
| Kr | W | 750 | 0 | 0 | 1.08 | 105 |
| Kr | W | 750 | 0 | 15 | 1.17 | 118 |
| Kr | W | 750 | 0 | 30 | 1.36 | 102 |
| Kr | W | 750 | 0 | 45 | 1.42 | 78 |
| Kr | W | 750 | 0 | 60 | 1.30 | 14 |
| Kr | W | 500 | 0 | 0 | 0.75 | 132 |
| Kr | W | 500 | 0 | 15 | 0.83 | 130 |
| Kr | W | 500 | 0 | 30 | 0.94 | 135 |
| Kr | W | 500 | 0 | 45 | 0.94 | 135 |
| Kr | W | 500 | 0 | 60 | 0.83 | 56 |
| Xe | W | 1500 | 0 | 0 | 1.83 | 97 |
| Xe | W | 1500 | 0 | 15 | 2.00 | 128 |
| Xe | W | 1500 | 0 | 30 | 2.38 | 107 |
| Xe | W | 1500 | 0 | 45 | 2.54 | 75 |
| Xe | W | 1500 | 0 | 60 | 2.45 | 0 |
| Xe | W | 1000 | 0 | 0 | 1.45 | 154 |
| Xe | W | 1000 | 0 | 15 | 1.58 | 178 |
| Xe | W | 1000 | 0 | 30 | 1.88 | 187 |
| Xe | W | 1000 | 0 | 45 | 2.02 | 146 |
| Xe | W | 1000 | 0 | 60 | 1.85 | 26 |

| Ion | Target | Energy (eV) | Phi (º) | Beta (º) | Y* (atoms/ion) | E* (eV) |
|---|---|---|---|---|---|---|
| Xe | W | 750 | 0 | 0 | 1.18 | 182 |
| Xe | W | 750 | 0 | 15 | 1.33 | 196 |
| Xe | W | 750 | 0 | 30 | 1.62 | 220 |
| Xe | W | 750 | 0 | 45 | 1.72 | 183 |
| Xe | W | 750 | 0 | 60 | 1.50 | 55 |
| Xe | W | 500 | 0 | 0 | 0.78 | 193 |
| Xe | W | 500 | 0 | 15 | 0.88 | 202 |
| Xe | W | 500 | 0 | 30 | 1.01 | 213 |
| Xe | W | 500 | 0 | 45 | 1.06 | 197 |
| Xe | W | 500 | 0 | 60 | 0.86 | 104 |
| Kr | Mo | 1500 | 0 | 0 | 1.23 | 123 |
| Kr | Mo | 1500 | 0 | 15 | 1.66 | 233 |
| Kr | Mo | 1500 | 0 | 30 | 2.37 | 197 |
| Kr | Mo | 1500 | 0 | 45 | 2.61 | 169 |
| Kr | Mo | 1500 | 0 | 60 | 2.59 | 49 |
| Kr | Mo | 1000 | 0 | 0 | 1.22 | 248 |
| Kr | Mo | 1000 | 0 | 15 | 1.43 | 252 |
| Kr | Mo | 1000 | 0 | 30 | 1.97 | 205 |
| Kr | Mo | 1000 | 0 | 45 | 2.15 | 222 |
| Kr | Mo | 1000 | 0 | 60 | 2.11 | 124 |
| Kr | Mo | 750 | 0 | 0 | 1.02 | 226 |
| Kr | Mo | 750 | 0 | 15 | 1.21 | 265 |
| Kr | Mo | 750 | 0 | 30 | 1.59 | 271 |
| Kr | Mo | 750 | 0 | 45 | 1.84 | 247 |
| Kr | Mo | 750 | 0 | 60 | 1.76 | 165 |
| Kr | Mo | 500 | 0 | 0 | 0.65 | 206 |
| Kr | Mo | 500 | 0 | 15 | 0.82 | 218 |
| Kr | Mo | 500 | 0 | 30 | 1.11 | 230 |
| Kr | Mo | 500 | 0 | 45 | 1.31 | 247 |
| Kr | Mo | 500 | 0 | 60 | 1.13 | 200 |
| Ar | W | 1500 | 0 | 0 | 0.94 | 0 |
| Ar | W | 1500 | 0 | 15 | 1.06 | 0 |
| Ar | W | 1500 | 0 | 30 | 1.31 | 0 |
| Ar | W | 1500 | 0 | 45 | 1.33 | 0 |
| Ar | W | 1500 | 0 | 60 | 1.30 | 0 |
| Ar | W | 1000 | 0 | 0 | 0.78 | 2.5 |
| Ar | W | 1000 | 0 | 15 | 0.90 | 15 |
| Ar | W | 1000 | 0 | 30 | 1.10 | 0.4 |
| Ar | W | 1000 | 0 | 45 | 1.14 | 1.05 |
| Ar | W | 1000 | 0 | 60 | 1.13 | 0 |
| Ar | W | 750 | 0 | 0 | 0.72 | 22 |
| Ar | W | 750 | 0 | 15 | 0.75 | 14.3 |
| Ar | W | 750 | 0 | 30 | 0.90 | 20 |
| Ar | W | 750 | 0 | 45 | 0.94 | 21 |
| Ar | W | 750 | 0 | 60 | 0.90 | 1.04 |
| Ar | W | 500 | 0 | 0 | 0.53 | 40 |
| Ar | W | 500 | 0 | 15 | 0.56 | 33 |
| Ar | W | 500 | 0 | 30 | 0.65 | 56 |
| Ar | W | 500 | 0 | 45 | 0.68 | 58 |
| Ar | W | 500 | 0 | 60 | 0.61 | 35 |

# Appendix C:

# Table of Data Collected in Azimuthal Experiments (500 eV $Xe^+$ on Mo)

| β (°) | α (°) | Φ (°) | y (atoms/ion/str) |
|---|---|---|---|
| 0 | 90 | 0 | 0.0037 |
| 0 | 80 | 0 | 0.0441 |
| 0 | 70 | 0 | 0.081 |
| 0 | 60 | 0 | 0.1203 |
| 0 | 50 | 0 | 0.1288 |
| 0 | 40 | 0 | 0.1102 |
| 0 | 30 | 0 | 0.0864 |
| 0 | 20 | 0 | 0.0695 |
| 0 | 10 | 0 | 0.0692 |
| 0 | 0 | 0 | 0.0703 |
| 0 | 20 | 180 | 0.0749 |
| 0 | 30 | 180 | 0.0923 |
| 0 | 40 | 180 | 0.1153 |
| 0 | 50 | 180 | 0.1238 |
| 0 | 60 | 180 | 0.102 |
| 0 | 70 | 180 | 0.0573 |
| 0 | 80 | 180 | 0.0138 |
| 0 | 90 | 180 | 0.0025 |
| 0 | 90 | 165 | 0.0019 |
| 0 | 80 | 165 | 0.0129 |
| 0 | 70 | 165 | 0.0635 |
| 0 | 60 | 165 | 0.1116 |
| 0 | 50 | 165 | 0.1351 |
| 0 | 40 | 165 | 0.1237 |
| 0 | 30 | 165 | 0.0978 |
| 0 | 20 | 165 | 0.0762 |
| 0 | 10 | 165 | 0.0714 |
| 0 | 10 | 15 | 0.0771 |
| 0 | 20 | 15 | 0.0827 |
| 0 | 30 | 15 | 0.0966 |
| 0 | 40 | 15 | 0.1191 |
| 0 | 50 | 15 | 0.1329 |
| 0 | 60 | 15 | 0.127 |
| 0 | 70 | 15 | 0.0851 |
| 0 | 80 | 15 | 0.0325 |
| 0 | 90 | 15 | 0.0036 |
| 0 | 90 | 30 | 0.0015 |
| 0 | 80 | 30 | 0.034 |
| 0 | 70 | 30 | 0.0891 |
| 0 | 60 | 30 | 0.1272 |
| 0 | 50 | 30 | 0.1395 |
| 0 | 40 | 30 | 0.1278 |
| 0 | 30 | 30 | 0.1039 |
| 0 | 20 | 30 | 0.0871 |
| 0 | 10 | 30 | 0.0789 |
| 0 | 10 | 150 | 0.0798 |
| 0 | 20 | 150 | 0.0887 |
| 0 | 30 | 150 | 0.108 |
| 0 | 40 | 150 | 0.1318 |

| β (°) | α (°) | Φ (°) | y (atoms/ion/str) |
|---|---|---|---|
| 0 | 50 | 150 | 0.1345 |
| 0 | 60 | 150 | 0.1097 |
| 0 | 70 | 150 | 0.063 |
| 0 | 80 | 150 | 0.0127 |
| 0 | 90 | 150 | 0.0027 |
| 0 | 90 | 135 | 0.0018 |
| 0 | 80 | 135 | 0.0183 |
| 0 | 70 | 135 | 0.0595 |
| 0 | 60 | 135 | 0.1075 |
| 0 | 50 | 135 | 0.1358 |
| 0 | 40 | 135 | 0.135 |
| 0 | 30 | 135 | 0.1132 |
| 0 | 20 | 135 | 0.0922 |
| 0 | 10 | 135 | 0.089 |
| 0 | 10 | 45 | 0.0856 |
| 0 | 20 | 45 | 0.106 |
| 0 | 30 | 45 | 0.1241 |
| 0 | 40 | 45 | 0.1415 |
| 0 | 50 | 45 | 0.1482 |
| 0 | 60 | 45 | 0.1316 |
| 0 | 70 | 45 | 0.0906 |
| 0 | 80 | 45 | 0.0359 |
| 0 | 90 | 45 | 0.0021 |
| 0 | 90 | 60 | 0.0003 |
| 0 | 80 | 60 | 0.0357 |
| 0 | 70 | 60 | 0.0888 |
| 0 | 60 | 60 | 0.1279 |
| 0 | 50 | 60 | 0.1523 |
| 0 | 40 | 60 | 0.1537 |
| 0 | 30 | 60 | 0.1377 |
| 0 | 20 | 60 | 0.1051 |
| 0 | 10 | 60 | 0.0866 |
| 0 | 10 | 120 | 0.0904 |
| 0 | 20 | 120 | 0.106 |
| 0 | 30 | 120 | 0.1304 |
| 0 | 40 | 120 | 0.1442 |
| 0 | 50 | 120 | 0.1384 |
| 0 | 60 | 120 | 0.1028 |
| 0 | 70 | 120 | 0.0566 |
| 0 | 80 | 120 | 0.0107 |
| 0 | 90 | 120 | 0.0016 |
| 0 | 90 | 105 | 0 |
| 0 | 80 | 105 | 0.0363 |
| 0 | 70 | 105 | 0.0715 |
| 0 | 60 | 105 | 0.0845 |
| 0 | 50 | 105 | 0.1284 |
| 0 | 40 | 105 | 0.1359 |
| 0 | 30 | 105 | 0.126 |
| 0 | 20 | 105 | 0.0985 |
| 0 | 10 | 105 | 0.0786 |

| β (°) | α (°) | Φ (°) | y (atoms/ion/str) |
|---|---|---|---|
| 0 | 10 | 75 | 0.0786 |
| 0 | 20 | 75 | 0.0930 |
| 0 | 30 | 75 | 0.1259 |
| 0 | 40 | 75 | 0.1344 |
| 0 | 50 | 75 | 0.1192 |
| 0 | 60 | 75 | 0.0870 |
| 0 | 70 | 75 | 0.0494 |
| 0 | 80 | 75 | 0.0100 |
| 0 | 90 | 75 | 0.0000 |
| 0 | 90 | 90 | 0.0015 |
| 0 | 80 | 90 | 0.0302 |
| 0 | 70 | 90 | 0.0756 |
| 0 | 60 | 90 | 0.1132 |
| 0 | 50 | 90 | 0.1367 |
| 0 | 40 | 90 | 0.1311 |
| 0 | 30 | 90 | 0.1108 |
| 0 | 20 | 90 | 0.0881 |
| 0 | 10 | 90 | 0.0790 |
| 0 | 10 | 90 | 0.0803 |
| 0 | 20 | 90 | 0.0919 |
| 0 | 30 | 90 | 0.1129 |
| 0 | 40 | 90 | 0.1311 |
| 0 | 50 | 90 | 0.1328 |
| 0 | 60 | 90 | 0.1100 |
| 0 | 70.0 | 90.0 | 0.0670 |
| 0 | 80.0 | 90.0 | 0.0193 |
| 0 | 90.0 | 90.0 | 0.0021 |
| 15 | 85.0 | 0.0 | 0.0037 |
| 15 | 75.0 | 0.0 | 0.0963 |
| 15 | 65.0 | 0.0 | 0.2237 |
| 15 | 55.0 | 0.0 | 0.3042 |
| 15 | 45.0 | 0.0 | 0.3098 |
| 15 | 35.0 | 0.0 | 0.2676 |
| 15 | 25.0 | 0.0 | 0.1947 |
| 15 | 15.0 | 0.0 | 0.1425 |
| 15 | 5.0 | 0.0 | 0.1124 |
| 15 | 0.0 | 0.0 | 0.0916 |
| 15 | 5.0 | 180.0 | 0.0660 |
| 15 | 5.0 | 0.0 | 0.0675 |
| 15 | 15.0 | 0.0 | 0.0767 |
| 15 | 55.0 | 180.0 | 0.0743 |
| 15 | 65.0 | 180.0 | 0.0519 |
| 15 | 75.0 | 180.0 | 0.0239 |
| 15 | 85.0 | 180.0 | 0.0026 |
| 15 | 84.5 | 165.9 | 0.0027 |
| 15 | 74.5 | 166.6 | 0.0257 |
| 15 | 64.6 | 167.3 | 0.0541 |
| 15 | 54.6 | 168.2 | 0.0775 |
| 15 | 44.6 | 169.4 | 0.0808 |
| 15 | 34.7 | 171.1 | 0.0715 |

| β (°) | α (°) | Φ (°) | y (atoms/ion/str) |
|---|---|---|---|
| 15 | 24.8 | 173.8 | 0.0695 |
| 15 | 5.9 | 154.2 | 0.0908 |
| 15 | 6.7 | 49.4 | 0.1131 |
| 15 | 15.9 | 28.1 | 0.1501 |
| 15 | 25.8 | 22.5 | 0.1933 |
| 15 | 35.7 | 19.9 | 0.2517 |
| 15 | 45.6 | 18.3 | 0.2914 |
| 15 | 55.6 | 17.1 | 0.2997 |
| 15 | 65.5 | 16.3 | 0.2266 |
| 15 | 75.5 | 15.5 | 0.1026 |
| 15 | 85.5 | 14.8 | 0.0036 |
| 15 | 87.0 | 29.5 | 0.0030 |
| 15 | 77.0 | 30.9 | 0.0862 |
| 15 | 67.1 | 32.3 | 0.1976 |
| 15 | 57.2 | 34.0 | 0.2676 |
| 15 | 47.4 | 36.0 | 0.2728 |
| 15 | 37.6 | 38.9 | 0.2504 |
| 15 | 27.9 | 43.4 | 0.2082 |
| 15 | 18.5 | 52.2 | 0.1646 |
| 15 | 10.2 | 75.9 | 0.1253 |
| 15 | 8.0 | 141.6 | 0.0937 |
| 15 | 24.2 | 167.8 | 0.0651 |
| 15 | 33.8 | 162.1 | 0.0693 |
| 15 | 43.6 | 158.7 | 0.0840 |
| 15 | 53.4 | 156.4 | 0.0856 |
| 15 | 63.3 | 154.6 | 0.0640 |
| 15 | 73.2 | 153.1 | 0.0312 |
| 15 | 83.1 | 151.8 | 0.0016 |
| 15 | 90.7 | 135.9 | 0.0010 |
| 15 | 80.9 | 137.7 | 0.0060 |
| 15 | 71.1 | 139.7 | 0.0412 |
| 15 | 61.3 | 141.8 | 0.0784 |
| 15 | 51.5 | 144.5 | 0.0990 |
| 15 | 41.8 | 148.0 | 0.0958 |
| 15 | 32.3 | 153.1 | 0.0801 |
| 15 | 23.2 | 161.8 | 0.0728 |
| 15 | 10.6 | 138.0 | 0.0932 |
| 15 | 14.0 | 92.3 | 0.1196 |
| 15 | 21.9 | 71.6 | 0.1715 |
| 15 | 31.0 | 62.1 | 0.2225 |
| 15 | 40.4 | 56.6 | 0.2450 |
| 15 | 50.1 | 53.0 | 0.2500 |
| 15 | 59.8 | 50.2 | 0.2245 |
| 15 | 69.6 | 48.0 | 0.1576 |
| 15 | 79.5 | 46.0 | 0.0569 |
| 15 | 89.3 | 44.1 | 0.0010 |
| 15 | 92.3 | 58.6 | 0.0051 |
| 15 | 82.6 | 60.9 | 0.0239 |
| 15 | 72.8 | 63.2 | 0.1096 |

| β (°) | α (°) | Φ (°) | y (atoms/ion/str) |
|---|---|---|---|
| 15 | 63.1 | 65.8 | 0.1710 |
| 15 | 53.5 | 68.9 | 0.2085 |
| 15 | 43.9 | 72.9 | 0.2370 |
| 15 | 34.6 | 78.6 | 0.2292 |
| 15 | 25.7 | 87.7 | 0.1883 |
| 15 | 17.8 | 104.8 | 0.1318 |
| 15 | 13.2 | 138.7 | 0.0930 |
| 15 | 21.8 | 156.1 | 0.0760 |
| 15 | 30.3 | 144.0 | 0.0892 |
| 15 | 39.5 | 137.1 | 0.1115 |
| 15 | 48.9 | 132.4 | 0.1228 |
| 15 | 58.6 | 129.0 | 0.1037 |
| 15 | 68.2 | 126.1 | 0.0646 |
| 15 | 78.0 | 123.7 | 0.0234 |
| 15 | 87.7 | 121.4 | 0.0031 |
| 15 | 84.2 | 107.0 | 0.0033 |
| 15 | 74.5 | 109.6 | 0.0434 |
| 15 | 64.9 | 112.5 | 0.0900 |
| 15 | 55.3 | 115.8 | 0.1301 |
| 15 | 45.8 | 120.0 | 0.1446 |
| 15 | 36.6 | 125.9 | 0.1334 |
| 15 | 27.8 | 134.9 | 0.1055 |
| 15 | 20.0 | 150.7 | 0.0888 |
| 15 | 15.7 | 141.6 | 0.0903 |
| 15 | 21.5 | 115.5 | 0.1203 |
| 15 | 29.5 | 101.6 | 0.1700 |
| 15 | 38.5 | 93.5 | 0.2057 |
| 15 | 47.8 | 88.1 | 0.2049 |
| 15 | 57.2 | 84.1 | 0.1732 |
| 15 | 66.8 | 80.8 | 0.1339 |
| 15 | 76.5 | 78.1 | 0.0722 |
| 15 | 86.2 | 75.5 | 0.0019 |
| 15 | 90.0 | 90.0 | 0.0016 |
| 15 | 80.3 | 92.6 | 0.0373 |
| 15 | 70.7 | 95.4 | 0.0959 |
| 15 | 61.1 | 98.5 | 0.1360 |
| 15 | 51.6 | 102.3 | 0.1701 |
| 15 | 42.3 | 107.1 | 0.1791 |
| 15 | 33.2 | 114.1 | 0.1535 |
| 15 | 24.8 | 125.4 | 0.1137 |
| 15 | 18.0 | 145.7 | 0.0867 |
| 15 | 18.0 | 145.7 | 0.0892 |
| 15 | 24.8 | 125.4 | 0.1156 |
| 15 | 33.2 | 114.1 | 0.1546 |
| 15 | 42.3 | 107.1 | 0.1743 |
| 15 | 51.6 | 102.3 | 0.1570 |
| 15 | 61.1 | 98.5 | 0.1214 |
| 15 | 70.7 | 95.4 | 0.0710 |
| 15 | 80.3 | 92.6 | 0.0100 |
| 15 | 90.0 | 90.0 | 0.0019 |

| β (°) | α (°) | Φ (°) | y (atoms/ion/str) |
|---|---|---|---|
| 30 | 0.0 | 0.0 | 0.1537 |
| 30 | 10.0 | 180.0 | 0.1012 |
| 30 | 20.0 | 180.0 | 0.0722 |
| 30 | 20.0 | 180.0 | 0.0487 |
| 30 | 50.0 | 180.0 | 0.0483 |
| 30 | 60.0 | 180.0 | 0.0480 |
| 30 | 70.0 | 180.0 | 0.0340 |
| 30 | 80.0 | 180.0 | 0.0126 |
| 30 | 90.0 | 180.0 | 0.0045 |
| 30 | 89.2 | 167.0 | 0.0035 |
| 30 | 79.2 | 168.4 | 0.0108 |
| 30 | 69.3 | 169.8 | 0.0335 |
| 30 | 59.4 | 171.4 | 0.0516 |
| 30 | 49.6 | 173.3 | 0.0543 |
| 30 | 39.7 | 176.0 | 0.0555 |
| 30 | 20.5 | 172.6 | 0.0758 |
| 30 | 11.8 | 154.3 | 0.1019 |
| 30 | 7.5 | 96.5 | 0.1593 |
| 30 | 13.1 | 47.1 | 0.2236 |
| 30 | 22.1 | 31.8 | 0.2845 |
| 30 | 31.6 | 25.3 | 0.3669 |
| 30 | 41.4 | 21.6 | 0.4560 |
| 30 | 51.2 | 19.1 | 0.5580 |
| 30 | 61.1 | 17.2 | 0.5389 |
| 30 | 71.0 | 15.6 | 0.3326 |
| 30 | 80.9 | 14.3 | 0.0873 |
| 30 | 90.8 | 13.0 | -0.0016 |
| 30 | 74.0 | 30.8 | 0.5324 |
| 30 | 64.3 | 33.7 | 0.6475 |
| 30 | 54.8 | 37.1 | 0.6044 |
| 30 | 45.3 | 41.4 | 0.5440 |
| 30 | 36.1 | 47.3 | 0.4929 |
| 30 | 27.3 | 56.5 | 0.3967 |
| 30 | 19.7 | 72.9 | 0.2826 |
| 30 | 14.9 | 103.1 | 0.1800 |
| 30 | 15.9 | 141.3 | 0.1035 |
| 30 | 21.9 | 166.5 | 0.0716 |
| 30 | 39.0 | 172.1 | 0.0523 |
| 30 | 48.3 | 166.8 | 0.0448 |
| 30 | 57.8 | 162.8 | 0.0302 |
| 30 | 67.4 | 159.6 | 0.0050 |
| 30 | 77.0 | 156.9 | 0.0023 |
| 30 | 82.7 | 141.9 | -0.0017 |
| 30 | 73.4 | 145.6 | 0.0032 |
| 30 | 64.1 | 149.7 | 0.0149 |
| 30 | 55.0 | 154.4 | 0.0398 |
| 30 | 46.1 | 160.4 | 0.0538 |
| 30 | 37.7 | 168.4 | 0.0560 |
| 30 | 23.9 | 162.4 | 0.0709 |
| 30 | 20.8 | 137.1 | 0.0992 |

| β (º) | α (º) | Φ (°) | y (atoms/ion/str) |
|---|---|---|---|
| 30 | 22.1 | 109.7 | 0.1810 |
| 30 | 27.0 | 88.7 | 0.2900 |
| 30 | 34.2 | 74.7 | 0.4129 |
| 30 | 42.3 | 65.4 | 0.4731 |
| 30 | 51.1 | 58.7 | 0.5007 |
| 30 | 60.1 | 53.4 | 0.5141 |
| 30 | 69.3 | 49.1 | 0.4832 |
| 30 | 78.6 | 45.3 | 0.3481 |
| 30 | 87.9 | 41.7 | 0.1475 |
| 30 | 97.3 | 38.1 | 0.0110 |
| 30 | 93.5 | 54.6 | 0.0148 |
| 30 | 84.5 | 59.0 | 0.1448 |
| 30 | 75.5 | 63.4 | 0.2776 |
| 30 | 66.6 | 68.3 | 0.3535 |
| 30 | 57.9 | 73.8 | 0.3736 |
| 30 | 49.5 | 80.5 | 0.3739 |
| 30 | 41.6 | 89.1 | 0.3521 |
| 30 | 34.5 | 100.7 | 0.2794 |
| 30 | 29.0 | 116.6 | 0.1813 |
| 30 | 25.9 | 137.4 | 0.1084 |
| 30 | 26.3 | 160.2 | 0.0706 |
| 30 | 36.0 | 165.2 | 0.0579 |
| 30 | 43.3 | 154.4 | 0.0651 |
| 30 | 51.3 | 146.3 | 0.0630 |
| 30 | 59.8 | 139.9 | 0.0390 |
| 30 | 68.6 | 134.6 | 0.0058 |
| 30 | 77.5 | 129.8 | 0.0022 |
| 30 | 86.5 | 125.4 | 0.0009 |
| 30 | 91.3 | 72.1 | 0.0077 |
| 30 | 82.6 | 76.9 | 0.0905 |
| 30 | 73.9 | 82.0 | 0.1828 |
| 30 | 65.3 | 87.5 | 0.2239 |
| 30 | 57.0 | 93.8 | 0.2477 |
| 30 | 49.0 | 101.4 | 0.2555 |
| 30 | 41.7 | 111.0 | 0.2186 |
| 30 | 35.4 | 123.6 | 0.1445 |
| 30 | 30.9 | 140.0 | 0.0989 |
| 30 | 28.9 | 159.7 | 0.0747 |
| 30 | 33.9 | 162.5 | 0.0735 |
| 30 | 39.7 | 148.8 | 0.0910 |
| 30 | 46.7 | 138.5 | 0.1015 |
| 30 | 54.5 | 130.3 | 0.0882 |
| 30 | 62.8 | 123.7 | 0.0562 |
| 30 | 71.3 | 118.0 | 0.0107 |
| 30 | 79.9 | 112.8 | 0.0031 |
| 30 | 88.7 | 107.9 | 0.0016 |
| 30 | 90.0 | 90.0 | -0.0650 |
| 30 | 81.4 | 95.0 | 0.0083 |
| 30 | 72.8 | 100.3 | 0.0386 |
| 30 | 64.3 | 106.1 | 0.0963 |

| β (º) | α (º) | Φ (°) | y (atoms/ion/str) |
|---|---|---|---|
| 30 | 56.2 | 112.8 | 0.1284 |
| 30 | 48.4 | 120.8 | 0.1440 |
| 30 | 41.4 | 130.9 | 0.1358 |
| 30 | 35.5 | 143.9 | 0.1112 |
| 30 | 31.5 | 160.6 | 0.0768 |
| 30 | 31.5 | 160.6 | 0.0692 |
| 30 | 35.5 | 143.9 | 0.0884 |
| 30 | 41.4 | 130.9 | 0.1383 |
| 30 | 48.4 | 120.8 | 0.1732 |
| 30 | 56.2 | 112.8 | 0.1677 |
| 30 | 64.3 | 106.1 | 0.1432 |
| 30 | 72.8 | 100.3 | 0.1087 |
| 30 | 81.4 | 95.0 | 0.0352 |
| 30 | 90.0 | 90.0 | 0.0029 |
| 45 | 85.0 | 0.0 | -0.0031 |
| 45 | 75.0 | 0.0 | 0.1321 |
| 45 | 65.0 | 0.0 | 0.3631 |
| 45 | 55.0 | 0.0 | 0.6195 |
| 45 | 45.0 | 0.0 | 0.6842 |
| 45 | 35.0 | 0.0 | 0.5752 |
| 45 | 25.0 | 0.0 | 0.4652 |
| 45 | 15.0 | 0.0 | 0.3708 |
| 45 | 5.0 | 0.0 | 0.2859 |
| 45 | 5.0 | 180.0 | 0.1867 |
| 45 | 15.0 | 180.0 | 0.1143 |
| 45 | 25.0 | 180.0 | 0.0704 |
| 45 | 35.0 | 180.0 | 0.0473 |
| 45 | 55.0 | 180.0 | 0.0359 |
| 45 | 65.0 | 180.0 | 0.0284 |
| 45 | 75.0 | 180.0 | 0.0163 |
| 45 | 85.0 | 180.0 | 0.0079 |
| 45 | 74.3 | 172.3 | 0.0224 |
| 45 | 64.5 | 174.4 | 0.0395 |
| 45 | 54.7 | 176.8 | 0.0456 |
| 45 | 35.4 | 175.6 | 0.0563 |
| 45 | 26.1 | 168.4 | 0.0938 |
| 45 | 17.5 | 154.5 | 0.1577 |
| 45 | 11.3 | 121.7 | 0.2619 |
| 45 | 12.1 | 70.9 | 0.3761 |
| 45 | 19.1 | 43.3 | 0.4882 |
| 45 | 27.9 | 31.3 | 0.5591 |
| 45 | 37.3 | 24.9 | 0.6644 |
| 45 | 46.9 | 20.8 | 0.7871 |
| 45 | 56.6 | 17.8 | 0.6609 |
| 45 | 66.4 | 15.4 | 0.3805 |
| 45 | 76.2 | 13.3 | 0.1190 |
| 45 | 86.1 | 11.5 | -0.0130 |
| 45 | 89.2 | 22.5 | -0.0110 |
| 45 | 79.8 | 26.1 | 0.0726 |
| 45 | 70.5 | 29.9 | 0.2808 |

| β (°) | α (°) | Φ (°) | y (atoms/ion/str) |
|---|---|---|---|
| 45 | 61.3 | 34.2 | 0.5324 |
| 45 | 52.2 | 39.2 | 0.6475 |
| 45 | 43.5 | 45.7 | 0.6044 |
| 45 | 35.2 | 54.6 | 0.5440 |
| 45 | 27.9 | 67.8 | 0.4929 |
| 45 | 22.5 | 87.8 | 0.3967 |
| 45 | 20.7 | 114.7 | 0.2826 |
| 45 | 23.3 | 140.8 | 0.1800 |
| 45 | 29.1 | 159.4 | 0.1035 |
| 45 | 36.6 | 171.6 | 0.0716 |
| 45 | 53.8 | 173.8 | 0.0523 |
| 45 | 62.9 | 168.9 | 0.0448 |
| 45 | 72.2 | 164.8 | 0.0302 |
| 45 | 81.5 | 161.0 | 0.0050 |
| 45 | 90.8 | 157.5 | 0.0023 |
| 45 | 94.6 | 142.1 | -0.0017 |
| 45 | 85.9 | 147.1 | 0.0032 |
| 45 | 77.3 | 152.2 | 0.0149 |
| 45 | 68.8 | 157.7 | 0.0398 |
| 45 | 60.4 | 163.9 | 0.0538 |
| 45 | 52.4 | 171.1 | 0.0560 |
| 45 | 38.4 | 168.6 | 0.0709 |
| 45 | 33.3 | 153.9 | 0.0992 |
| 45 | 30.4 | 135.7 | 0.1810 |
| 45 | 30.3 | 115.9 | 0.2900 |
| 45 | 33.1 | 97.5 | 0.4129 |
| 45 | 38.1 | 82.6 | 0.4731 |
| 45 | 44.6 | 71.1 | 0.5007 |
| 45 | 52.0 | 62.0 | 0.5141 |
| 45 | 60.0 | 54.7 | 0.4832 |
| 45 | 68.3 | 48.5 | 0.3481 |
| 45 | 76.8 | 43.0 | 0.1475 |
| 45 | 85.4 | 37.9 | 0.0110 |
| 45 | 84.8 | 54.8 | 0.0148 |
| 45 | 77.0 | 61.1 | 0.1448 |
| 45 | 69.3 | 67.8 | 0.2776 |
| 45 | 61.9 | 75.2 | 0.3535 |
| 45 | 55.0 | 83.7 | 0.3736 |
| 45 | 48.7 | 93.6 | 0.3739 |
| 45 | 43.5 | 105.5 | 0.3521 |
| 45 | 39.7 | 119.5 | 0.2794 |
| 45 | 37.9 | 135.2 | 0.1813 |
| 45 | 38.2 | 151.4 | 0.1084 |
| 45 | 40.7 | 166.7 | 0.0706 |
| 45 | 50.6 | 168.8 | 0.0579 |
| 45 | 57.1 | 159.3 | 0.0651 |
| 45 | 64.2 | 151.2 | 0.0630 |
| 45 | 71.7 | 144.1 | 0.0390 |
| 45 | 79.4 | 137.6 | 0.0058 |
| 45 | 87.3 | 131.3 | 0.0022 |

| β (°) | α (°) | Φ (°) | y (atoms/ion/str) |
|---|---|---|---|
| 45 | 95.2 | 125.2 | 0.0009 |
| 45 | 86.7 | 72.3 | 0.0077 |
| 45 | 79.5 | 79.3 | 0.0905 |
| 45 | 72.4 | 86.5 | 0.1828 |
| 45 | 65.6 | 94.4 | 0.2239 |
| 45 | 59.2 | 103.1 | 0.2477 |
| 45 | 53.5 | 113.0 | 0.2555 |
| 45 | 48.8 | 124.3 | 0.2186 |
| 45 | 45.3 | 137.2 | 0.1445 |
| 45 | 43.4 | 151.2 | 0.0989 |
| 45 | 43.3 | 165.8 | 0.0747 |
| 45 | 48.3 | 167.0 | 0.0735 |
| 45 | 53.0 | 155.6 | 0.0910 |
| 45 | 58.6 | 145.5 | 0.1015 |
| 45 | 64.9 | 136.7 | 0.0882 |
| 45 | 71.7 | 128.8 | 0.0562 |
| 45 | 78.8 | 121.5 | 0.0107 |
| 45 | 86.0 | 114.5 | 0.0031 |
| 45 | 93.3 | 107.7 | 0.0016 |
| 45 | 90.0 | 90.0 | -0.0650 |
| 45 | 82.9 | 97.1 | 0.0083 |
| 45 | 76.0 | 104.4 | 0.0386 |
| 45 | 69.3 | 112.2 | 0.0963 |
| 45 | 63.0 | 120.7 | 0.1284 |
| 45 | 57.2 | 130.1 | 0.1440 |
| 45 | 52.2 | 140.8 | 0.1358 |
| 45 | 48.4 | 152.8 | 0.1112 |
| 45 | 45.9 | 166.0 | 0.0768 |
| 45 | 45.9 | 166.0 | 0.0692 |
| 45 | 48.4 | 152.8 | 0.0884 |
| 45 | 52.2 | 140.8 | 0.1383 |
| 45 | 57.2 | 130.1 | 0.1732 |
| 45 | 63.0 | 120.7 | 0.1677 |
| 45 | 69.3 | 112.2 | 0.1432 |
| 45 | 76.0 | 104.4 | 0.1087 |
| 45 | 82.9 | 97.1 | 0.0352 |
| 45 | 90.0 | 90.0 | 0.0029 |